Full-Wave Modeling of Radar Scattering From Maize and Inversion Methods for Biophysical Parameter Estimation

by

A. Kaleo Roberts

A dissertation submitted in partial fulfillment
of the requirements for the degree of
Doctor of Philosophy
(Electrical and Computer Engineering)
in the University of Michigan
2025

Doctoral Committee:

Professor Kamal Sarabandi, Chair
Associate Research Scientist Leland Pierce
Professor Chris Ruf
Professor Leung Tsang

A. Kaleo Roberts
kaleor@umich.edu
ORCID iD: 0000-0002-4858-4864

© A. Kaleo Roberts 2025

DEDICATION

To my parents Thomas and Maile Roberts.

ACKNOWLEDGEMENTS

Looking back on my doctoral journey, I am reminded that although some aspects of it were a bit lonely, there were still many people that helped me in one form or another. Here I would like to express my gratitude for many of those who helped.

First and foremost, I would like to warmly thank my doctoral advisor Professor Kamal Sarabandi. He almost always made himself available to me when I went looking for his guidance or help. There was much that I learned from him in taking his classes or discussing different strategies for moving research goals forward. He has also provided me with many recommendation letters over the years. I am also very grateful for his patience with my efforts. This journey would never have occurred if he had not accepted me as a student, and for that I am most grateful.

I would also like to thank the members of my dissertation committee: Dr. Leland Pierce, Professor Chris Ruf, and Professor Leung Tsang. I had the good fortune to take one of Prof. Tsang's classes and gain some insight into fast numerical methods from it. It was also a pleasure to gain a wider knowledge of efforts in the remote sensing field from a class presentation made by Prof. Ruf in a remote sensing class. Dr. Pierce has also been a helpful advisor in striving to manage a student remote sensing organization, and also a pleasant, sympathetic colleague to discuss ideas with. I also appreciate the advice they've given me and the time and effort they have dedicated in order to serve on the committee.

I would also like to give a warm thanks to Professor Jasmeet Judge at the University of Florida for the opportunity to collaborate on research with her. Her insights and the contributions of her group are an important part of the research in this work. I also wish to thank her associates Professor Alejandro Monsivais-Huertero, Professor Robert Moore, and Dr. Kaiser Niknam. It was a pleasure to meet with them on a weekly basis for a season.

I would also like to thank a few researchers that have been helpful in making this work possible. I would like to thank Dr. Heather McNairn, Dr. Ramata Magagi, and Amanda Halstead for providing access to the pin profilometer and leaf area index photos from SMAPVEX12. I also want to thank Dr. Andreas Colliander and Dr. Xiaolan Xu for their help in working with the UAVSAR data.

A big thank you also goes to the research staff at the RADLAB: Dr. Adib Nashishibi and Dr. Behzad Yektakhah. Dr. Nashishibi was almost always pleasant and eager to help me when

he could. Dr. Yektakhah introduced me to the logistics of using the University of Michigan's Great Lakes high-performance computing servers, which has certainly been an essential tool in completing the work of this dissertation.

I would be remiss if I failed to express my thanks for the great help of the staff in the Electrical and Computer Engineering Department (EECS) at the University of Michigan. This includes the graduate student coordinator Kristen Thornton, who provided me with indispensable help and advice throughout the program and had my back on more than one occasion. It also includes Michelle Chapman for helping to organize research grant application packages and Kathrine Godwin and Erika Booms for helping to organize travel and registration at conferences. It was also great to hear about Kathrine's own doctoral work in France, and Erika's baked goods are some of the best. Additionally, the staff at EECS DCO, including Don Winsor and George Kroslak, were also very helpful with meeting the computer needs of this work, which included getting internet to my lab computer, acquiring a new computer, finding additional hard drives for data storage, and determining a way to back up research data.

There were a few semesters where I had the opportunity to serve as a graduate student instructor in the EECS department. I would like to thank the professors that I worked with, namely Dr. Fatemeh Arbabjolfaei, Dr. Sangsin Na, and Professor Wayne Stark. I would also like to thank a few of the professors that I had the opportunity to take a class from. I am grateful to Professor Anthony Grbic for his metamaterials class and reference letters. I am also grateful to Professor Fawwaz Ulaby for taking time in his remote sensing class to individually meet with all the students, including myself.

Luckily, there are fellow graduate students that have helped or been with me through this program to varying degrees. I am certainly grateful for their advice and friendship. I am grateful to Tanner Douglas for helping me to move my utilization of the Great Lakes HPC to an advanced level and Menglou Rao for giving me some good on-boarding advice. It was also a pleasure to have Abdelhamid Nasr as a graduate student instructor when I took the microwave measurements class. I am grateful for the good humor of James Gruber as a lab partner and Matthew Belz as a project partner when taking the first microwave circuits class. I would also like to thank Haokui Xu and Firoz Borah for providing touchstones to the remote sensing world that I was relatively unfamiliar with. I also thank Weihui Gu for showing me the ropes on how to export raw field data from HFSS. Also worth mentioning are some former and current students including Navid Barani, David Geroski, Max Bright, Brian Raeker, Hamad Alotaibi, Abdullah Alothman, Chun-Wen Lin, Wenhao Peng, Ruoxing Gao, Malik Almunif, Duncan Madden, Zachary Fritts, Zhenming Huang, John Le, Andrew Park, Amirata Tabatabavakili, Hersh Desai, Ehsan Hafezi, Jongwoo Jeong, Siyu Su, Dinan Bai, Gopal Sundaram, Aysu Akbari, Coady Lewis, Andrew DeVries, and Angie Bu. It has also been a blessing to know and work with Aditya Muppala as a project partner in the mi-

crowave measurements class, especially during our collaboration on the dielectric measurement system.

It was also a great pleasure to meet new friends that helped me to keep my sanity while conducting research. This includes the folks at the U-M Amateur Radio Club (W8UM), with whom I was able to associate and serve with over much of my program. This includes past members like Michael Fluegemann, Kim Zwolshen, Maggie Li, Mick Gordinier, Peter Crary, Professor Amir Mortazawi, and last but certainly not least the eminent station manager John Palmisano. Participating in foxhunts, some collegiate contests, and field days were new, enjoyable experiences for me.

I would also like to thank my advisors and mentors from my alma mater, Brigham Young University, who helped to make this endeavor a possibility for me: my master's advisor Dr. Karl Warnick, my master's committee members Dr. David Long and Dr. Michael Rice, and also Dr. Greg Nordin. Thank you for your advice and reference letters over the years.

This doctoral experience would have been very different without funding support from a few organizations. I would like to express my gratitude to the Rackham Merit Fellows program, especially Dr. Cherie Dotson; the American Indian Science and Engineering Society (AISES) in partnership with Intel for the Growing the Legacy Scholarship; and the J. Robert Beyster Computational Innovation Graduate Fellows Program.

I would also like to thank those that have supported or encouraged me in this endeavor throughout the years: Lars Bowman, my grandfather Eldon Roberts, and grandmother Dora Kamalu. Much thanks are also due to Steve Taylor for providing reference letters. I am also grateful to Ashley Calder for listening and providing feedback on my research presentations.

Finally, I would like to thank my parents and siblings for their support, concern, patience, and love throughout this process. It certainly helped to be able to talk with them or engage in online activities to stay in touch with each other and take some of the stress off. The help, support, and love of my parents Thomas and Maile Roberts was invaluable to me, and they helped me navigate some of the vagaries that a doctoral program can bring. Perhaps most PhD students will agree that there are peaks and valleys to the graduate school experience. I am very grateful for my parents in helping to get me through the valleys and to celebrate the peaks.

TABLE OF CONTENTS

DEDICATION ii

ACKNOWLEDGEMENTS iii

LIST OF FIGURES ix

LIST OF TABLES xiii

LIST OF ACRONYMS xiv

ABSTRACT xvi

CHAPTER

1 Introduction 1

1.1 Research Objectives 4
1.2 Background 5
1.2.1 Forward Model for Predicting Radar Backscatter 5
1.2.2 Inverse Models for Physical Parameters From Radar Backscatter 11
1.2.3 Electrical Characterization of Soil and Plant Material 13
1.3 Methodology 15
1.4 Dissertation Outline 16

2 In-line Dielectric Measurement Apparatus for Liquids 18

2.1 Introduction 18
2.2 Background 19
2.3 Design and Manufacturing 23
2.4 Simulation Results 25
2.4.1 Parametric Analysis 25
2.4.2 Sensitivity Analysis 29
2.5 Methodology 30
2.5.1 Experimental Setup 30
2.5.2 Sample Preparation 33
2.5.3 Data Processing 33
2.5.4 Extraction of f_0 and Q 34
2.5.5 Construction of Inverse Model 35
2.6 Error Analysis 37

2.7 Experimental Results . . . 41
2.7.1 Spot Measurements . . . 42
2.7.2 Real Time Measurements . . . 43
2.8 Conclusion . . . 46

3 EM Simulation Development and Characteristics . . . 48

3.1 Simulation Methodology . . . 49
3.1.1 Potential Simulation Configurations . . . 50
3.2 Adapting Corn Plants for The Simulation Methodology . . . 56
3.2.1 Corn Plant Description . . . 56
3.2.2 Electromagnetic Representation of Corn Components . . . 57
3.2.3 Geometric Representation of Corn Components . . . 61
3.2.4 University of Florida Dataset . . . 64
3.3 Soil Model . . . 69
3.3.1 Soil Dielectric Constant . . . 69
3.3.2 Soil Structure . . . 70
3.4 Plane Wave Equivalence Validation . . . 78
3.5 Canopy Row Structure . . . 79
3.5.1 Row and inter-plant spacing characteristics . . . 80
3.5.2 Effect of Plant Spacing on Backscatter . . . 82
3.5.3 Backscatter Behavior Versus Angle for a Small Patch of Plants . . . 85

4 Full-Wave Numerical Scattering Model for Corn . . . 88

4.1 Introduction . . . 88
4.2 Scattering Model Description . . . 92
4.2.1 Plant 3D CAD Model . . . 93
4.2.2 Electromagnetic Analysis . . . 94
4.3 Study Site . . . 100
4.4 Model Validation . . . 103
4.4.1 Comparison of Models Against SAR Measurement . . . 105
4.4.2 Computation Performance . . . 107
4.4.3 Backscatter Sensitivity to Soil Moisture and Vegetation Water Content . . . 107
4.5 Discussion . . . 109
4.6 Conclusion . . . 110

5 Inverse Model for Radar Sensing of Corn . . . 112

5.1 Introduction . . . 112
5.2 Forward Model . . . 115
5.2.1 Full-Wave Model . . . 116
5.2.2 Multivariate Macromodel . . . 118
5.3 Inversion Algorithm . . . 121
5.3.1 Iterative, Nonlinear, Regularized Inversion . . . 122
5.3.2 Regressive, Residual Neural Network . . . 123
5.3.3 Growth Stage Smoothing . . . 126
5.3.4 Simulated Algorithm Performance . . . 127

5.4 Description of Validation Data . . . 128
5.4.1 Soil and Vegetation Data . . . 129
5.4.2 SAR Data . . . 130
5.5 Results . . . 130
5.5.1 Forward Model Predictions . . . 130
5.5.2 Inversion Results . . . 132
5.6 Discussion . . . 136
5.7 Conclusion . . . 138
6 Conclusion . . . 140
6.1 Research Summary and Contributions . . . 140
6.2 Insights . . . 141
6.3 Future Work . . . 143
6.3.1 Standardized Test Datasets . . . 143
6.3.2 Modeling Tilted Ground Planes . . . 143
6.3.3 Additional Directions for Future Investigation . . . 144

APPENDICES . . . 145

BIBLIOGRAPHY . . . 146

LIST OF FIGURES

FIGURE

1.1 NISAR satellite concept art. . . . 3
1.2 Outline of research topics in this dissertation. . . . 4
1.3 Model of scattering processes under a single-scattering assumption: (1) direct, (2,3) direct-reflected, (4) indirect, and (5) rough surface. . . . 9
1.4 Different mapping classifications for functions. . . . 12

2.1 Supercoupling device made of machined pockets and micro-3D printed sample holder. 21
2.2 Cross section (front view) and side view of Device 1 and 2. . . . 24
2.3 Channel length sweep comparison between the supercoupling mode and the Fabry-Pérot mode. The black lines indicate the chosen design values. . . . 26
2.4 Channel height sweep comparison between Device 1 and 2. The black lines indicate the chosen design values. . . . 27
2.5 Sample holder chamber radius and height sweep comparison between Device 1 and 2. The black lines indicate the chosen design values. . . . 28
2.6 Close up of the sample holder/chamber (yellow in inset image) and the top and bottom halves of Device 2. . . . 30
2.7 Fully assembled devices with heat shrink tube connections to the sample holders. . . . 31
2.8 Schematic of the measurement setup. The device was connected to WR90 waveguides on both sides. The waveguides were attached to waveguide-to-coax adapters, which were used to connect the setup to the VNA via coaxial cables. Sample liquids were introduced into the device from the bottom to prevent the formation of air cavities inside the sample holder. . . . 32
2.9 Processing flow for results. . . . 33
2.10 Typical S_{21} measurement for water. The center frequency f_0 and points 3 dB below the peak are shown with red cross hairs in the left panel. The right panel shows the data in blue compared with a fitted parabola in red for interpolating the location of f_0. Blue circles are sample points. . . . 34
2.11 A comparison between the measured and simulated S_{21} after performing the forward model optimization using a constrained Nelder-Mead algorithm. Simulations are shown in solid lines and measurements are shown in dots. . . . 35
2.12 The inversion surface of ϵ_r for Device 2 generated by interpolating the sweep points (blue dots) that are obtained from HFSS transmission simulations. A bi-harmonic spline interpolation is used to generate the surface from the sample points. . . . 37
2.13 Average calibrated through response. One standard deviation is shown by the shaded areas. . . . 38

2.14 Experimental setup design and implementation for the real-time measurements. 44
2.15 Experimental results showing in-line measurements of the permittivity of two solutions whose compositions changed over time. 45

3.1 Diagrams of High Frequency Structure Solver (HFSS) simulation layouts for different scenarios. 51
3.2 A 3D view of an HFSS simulation using a Gaussian beam illumination. 52
3.3 Diagrams of HFSS simulation layouts with periodic boundaries. 53
3.4 Bragg angles in the first octant for 76×17 cm (red dots) and 152×136 cm (yellow dots) rectangular lattices. 55
3.5 High-level anatomy of a corn plant, with a labeled diagram (left) left and an example plant (right). 56
3.6 Change in vegetation dielectric constant versus gravimetric moisture and frequency. . 59
3.7 HFSS simulation illustration of backscatter from a thin leaf. 60
3.8 Backscatter from a thin leaf as simulated with HFSS and a physical-optics (PO) approximation for vertical (left) and horizontal (right) polarizations. 61
3.9 Diagrams of leaf measurements and CAD design. 62
3.10 Ear outline. 64
3.11 Corn stalk metrics versus the Day After Planting (DAP) based on data from the University of Florida. 66
3.12 Metrics for corn plant leaves versus the DAP based on data from the University of Florida. 67
3.13 Metrics for corn plant leaves and ears versus the DAP based on data from the University of Florida. 68
3.14 Soil texture diagram from [27]. 69
3.15 Permittivity for soil versus water content as formulated by Mironov et al. in [86]. . . . 70
3.16 A 1D profiles of soil surfaces: (top) a Gaussian rough surface with an exponential correlation function, (middle) a furrow structure defined as a combination of sinusoids, and (bottom) their summation. 71
3.17 Plots of the exponential, Gaussian, and power correlation functions, their associated power spectrums, and 1D profile examples: exponential (top), Gaussian (middle), power (bottom). 73
3.18 Comparison of the power spectrum of a sampled, exponential surface with its ideal spectrum, with $\Delta x = 5$ cm (left) and $\Delta x = 2$ cm (right). 74
3.19 Sample points along the x-axis of a 1D surface profile. 75
3.20 A 2D version of a periodic rough surface. 77
3.21 A 3D view of a rough, periodic surface (left) and a diagram of a plane wave incident on an array of regularly-spaced points (right). 78
3.22 3D views of different simulation configurations to test replacing the Floquet port with a plane wave. 80
3.23 Calibrated σ^0_{vv} SAR image in dB taken by NASA's UAVSAR of circular agricultural fields near Rosamond dry lake, CA, using a slant-range projection, with illumination coming from the bottom of the image. 81
3.24 Sampled and potential spacing distributions. 82

3.25 Point locations (left) and a heatmap (right) of the backscattered power from those points versus the incidence angle. 82
3.26 Illustration of point locations under different randomization schemes. 83
3.27 Heatmaps of average, normalized backscattered power versus incidence angle for each of the location randomization schemes. 84
3.28 HFSS corn patch simulation model (left) and heat maps of the average backscatter (right) for σ^0_{vv}, σ^0_{hh}, and σ^0_{hv} in dB, going from top to bottom. 86

4.1 Samples of corn plant geometries based on field measurements for four growth stages. 93
4.2 3D view of the electromagnetic simulation. Periodic boundaries (PRB) are applied to the left, right, front, and back sides of the simulation domain. A PML boundary is used on the top, while an impedance boundary (ZB) is used on the bottom of the soil layer. The soil layer is a dielectric material that is shown in brown near the bottom. . . 95
4.3 Level curves relating number of realizations, error interval, and confidence level (probability). The black marker indicates what was used in this study. 100
4.4 Satellite image of the SMAPVEX12 experiment region in Manitoba, Canada [33]. The total area imaged by UAVSAR is shown in red on the left panel. The right panel is a closeup of corn field 53, which is used for validation in this study. 101
4.5 SAR images of σ^0_{vv} of field 53, which is highlighted in blue. Row-like features for early-season corn (169) are likely tractor tracks. 102
4.6 Averaged ancillary data from field 53 over time. From top to bottom: stem height, plant biomass weight, gravimetric moisture content of plant components, and soil volumetric moisture content. 103
4.7 A single simulation realization from DoY 169 and 199, going from left to right. Each simulation is one of 50 total random realizations. The red disks are 10 cm thick, 20 cm wide, and spaced 50 cm apart and are only included for scale. 104
4.8 Simulated σ^0 (red, filled markers) compared with σ^0 data from UAVSAR for field 53 (blue squares) and SST predictions (green, unfilled markers). Whiskers around the red markers indicate the 90% confidence interval as defined by (4.8), while circles show the mean value. Whiskers on the blue markers indicate the 1st and 3rd quartiles of the SAR data, while the circles indicate the median. 106
4.9 Average backscatter from sweeping SM and VWC for the early and mature growth stages. Again, the shaded areas show the 90% confidence interval, where at least 15 realizations were computed for each sweep point. 108

5.1 Corn allometric relationships recorded by the University of Florida versus DAP: (a) stalk height, (b) stalk width, (c) number of leaves, and (d) ear radius. 117
5.2 A surface plot showing the allometric relationships for leaf length (left) and a labeled diagram of the computational domain for calculating the backscatter from a corn field (right). 118
5.3 Representative plant models used for each growth stage in the macromodel with labels for the DAP of each 3D model. 119
5.4 Surface plots of the spline macromodel fit to the full-wave simulation data (red dots) for σ^0_{vv} (top) and σ^0_{hh} (bottom) as a function of the DAP and SMC for a fixed $\theta_i = 40$ and $h_{rms} = 1.5$ cm. 121

5.5 Diagram of inversion algorithm. 122
5.6 Diagram of ResNet structure for soil moisture and growth stage estimation. 124
5.7 Retrieval performance for SMC from simulated data without (left) and with (right) knowledge of the roughness. 126
5.8 Retrieval performance for DAP from simulated data without (left) and with (right) knowledge of the roughness. 127
5.9 Map of corn fields considered in this study (left) and typical soil moisture sampling locations (right). 128
5.10 Comparison of σ^0_{pq} from UAVSAR data and the macromodel. 131
5.11 Correlations for the predicted and measured backscattering coefficients. The DOY color scale is identical among all plots. 132
5.12 Inversion results for SMC. 133
5.13 Scatter plots of measured SMC and estimated SMC values without (left) and with (right) soil roughness information. 134
5.14 Inversion results for plant height. 135
5.15 Scatterplots for smoothed plant height, with nominal results on the left, and results that include roughness information on the right. 136
5.16 Scatterplots of the average measured co-pol phase difference versus measured SMC (left) and plant height (right). 139

LIST OF TABLES

TABLE

2.1 Sensitivity of ϵ_r and $\tan\delta$ from Device 2 with respect to several key parameters and different sample liquids, assuming $\tan\delta = 0.4$ for each liquid. 29
2.2 Measured water-alcohol mixtures by alcohol volumetric percentage. 32
2.3 Device 1 (left) and Device 2 (right) spot measurements. Distilled water, ethanol, and methanol are indicated by W, E, and M respectively. The center frequency f_0 is given in GHz. 42

3.1 Comparing the backscattering coefficient of three simulation configurations to assess if the plane wave excitation can replace the Floquet port excitation. 79
3.2 Simulation parameters for the corn patch simulations associated with Fig. 3.28. 85

4.1 Model input parameters. 105
4.2 Simulation input parameters for the DoY 169 variations indicated by the markers. . . . 105
4.3 Computation statistics of a single realization. 107

5.1 Varied parameters in the simulation database. 119
5.2 Average soil parameters and incidence angle for each field. 129
5.3 Summary of inversion performance 137

LIST OF ACRONYMS

AGB Above Ground Biomass

ANN artificial neural network

CAD Computer-Aided Design

CNC Computer Numerical Control

DANL Displayed Average Noise Level

DAP Day After Planting

DBA Distorted Born Approximation

DOY Day of Year

ENZ Epsilon-Near-Zero

FDTD Finite-Difference Time-domain

FEM Finite Element Method

GNSS Global Navigation Satellite System

GPU Graphics Processing Unit

HFSS High Frequency Structure Solver

HPC High Performance Computing

IEM Integral Equation Method

KA Kirchoff Approximation

LIDAR Light Detection and Ranging

ML Machine Learning

MoM Method of Moments

PALS Passive Active L band System

PML Perfectly Matched Layer

PO Physical Optics

RCS Radar Cross Section

RMS Root Mean Square

RMSE Root Mean Square Error

RT Radiative Transfer

ReLU Rectified Linear Unit

SAR Synthetic Aperture Radar

SIW Substrate-Integrated Waveguide

SMAP Soil Moisture Active Passive

SMC Soil Moisture Content

SPM Small Perturbation Method

SST Single Scattering Theory

UAVSAR Uninhabited Aerial Vehicle Synthetic Aperture Radar

VNA Vector Network Analyzer

VWC Vegetation Water Content

WCM Water Cloud Model

ABSTRACT

Soil moisture and biomass are two important quantities that can affect the climate, weather, and agriculture. There is interest in measuring them from space because of the global, frequent, and repeated observations that could be achieved. Synthetic aperture radar (SAR) is an attractive imaging sensor for this because microwaves can readily penetrate foliage, and SAR can take high resolution images in all weather conditions. Translating radar backscatter to biomass or soil moisture is challenging, though, because it is also influenced by other variables. This work explores novel methods for interpreting radar backscatter in terms of soil moisture and biomass for corn fields. Key findings include the feasibility of using full-wave models and better inversion accuracy for biomass than soil moisture when polarimetric SAR systems are used at L-band (1.25 GHz).

The first part of this dissertation proposes a device for real-time measurement of the complex dielectric constant of liquids at X-band. The device consists of a narrow waveguide channel operating at the cut-off frequency. A micro-3D printed sample holder is placed inside the channel and connected to feeding tubes that are designed to prevent energy leakage from the channel. Two variations of the device are fabricated: one that provides higher accuracy, and another that provides higher sensitivity. The dielectric constant is estimated by using forward and inverse models based on full-wave simulations of the devices. Experiments with static and time-varying liquids are performed. The static measurements are done with mixtures of ethanol-water and methanol-water. The time-varying measurements are done with ethanol-water-sugar and ethanol-water mixtures. The measured results are consistent between the two devices and are in good agreement with the published literature.

The second part of this dissertation begins to focus on how microwaves scatter from corn fields. Historically, corn is a difficult crop to model at microwave frequencies. Novel models based on full-wave electromagnetic solvers can be accurate by accounting for multiple scattering among plant constituents, other adjacent plants, and the underlying soil surface. Such a model is computationally expensive, but the increased availability of computing resources may make it more feasible. This part presents a simulation methodology for calculating radar backscatter from corn fields at L-band based on finite element method (FEM) simulations. The physical representation of the corn plants comes from data-based 3-D plant models. The results of simulations are validated with synthetic aperture radar (SAR) data obtained during the SM active passive validation

experiment of 2012 (SMAPVEX12) experimental campaign. Validation is performed for two days within the experimental campaign. Good agreement is observed between the simulated and measured backscatter.

The final part of this dissertation considers how biophysical parameters of corn fields might be estimated with radar data. Here, the full-wave scattering model from the second part of this work is used in tandem with an inversion algorithm that combines machine learning and regularized inversion. The scattering model is first used to create a spline-based macromodel. The macromodel is then inverted with the hybrid inversion algorithm. The performance of the method is evaluated against simulated data from the SMAPVEX12 campaign for sensing soil moisture and plant height. It was found that the inversion algorithm did not effectively retrieve soil moisture, but it did retrieve plant height during vegetative growth with a correlation coefficient of 0.95 and RMSE of 39 cm.

CHAPTER 1

Introduction

Radar is a vitally important type of sensing instrument that can detect, locate, and determine the characteristics of distant objects using radio waves. It finds widespread use in applications like air traffic control, marine and automotive navigation, surveillance, and radar remote sensing. The latter application seeks to gain information about the earth's surface from radar observations. There has been sustained interest in using radar to measure physical characteristics of the earth's surface such as soil water content, above-ground vegetation, canopy average height, and surface wind speed over the oceans. This is because radars can produce high-resolution images of the earth's surface in almost all weather and lighting conditions.

Soil moisture and biomass are two physical quantities that have an important impact on earth's climate. Soil moisture or Soil Moisture Content (SMC) is important because of its role in the water cycle, which affects weather and plants. Its impact can manifest in exacerbating heat waves when more sunlight is converted into heat rather than creating water vapor [14], higher chances of dust storms from lack of moisture, increased flooding risks when the soil is already saturated with water, and potentially greater chances of precipitation from instabilities that are injected into the atmosphere from evaporation [14]. Both soil moisture and biomass are especially relevant in agriculture. There is only a relatively small portion of land used for agriculture at 7.5% of the world's habitable land ($\sim$8 Mkm^2). However, monitoring soil moisture and biomass in these areas could have a significant impact on peoples' lives because that land produces 83% of the world's calorie and 62% of its protein supply [111]. And in most cases, agricultural activities are the primary user of freshwater, where 70%, on average, of the freshwater supply is directed

to agriculture globally [110]. High resolution maps of soil moisture could help farmers use water more efficiently [20]. Sensing biomass could also be helpful with improving yield forecasts, which could give grain markets more time to coordinate shortages and surpluses [79].

Direct methods exist for measuring SMC or biomass. Hand-held or wired sensors can measure soil moisture, and biomass can be measured by destructive sampling from an area. However, these spot-measurements are labor intensive and can only be approximately generalized to a larger area of land. Thus, researchers have looked to use spaceborne remote sensing instruments to create maps of SMC and biomass.

Microwave radars and radiometers are two primary instruments that have been used for soil moisture and biomass sensing. There is also a third, more recent type of sensing instrument that opportunistically uses signals from a Global Navigation Satellite System (GNSS) to implement a bistatic radar system, where a passive satellite will receive both the direct line-of-sight signal from a GNSS satellite and its reflection off of the Earth's surface to sense parameters like soil moisture [25]. All of these sensors can penetrate vegetation and reach the soil at the proper frequencies, unlike optical or infrared sensors that are blocked by it. This allows them to sense the soil moisture and the biomass. Radiometers typically provide more robust soil moisture estimates since the emission is less sensitive to the soil and plant structure, but their low spatial resolution (often more than 30 km) limits their application, especially for smart agriculture. GNSS reflectometry (GNSS-R) has better resolution than radiometers at about a $\sim$3 km resolution. This is still a relatively recent technology, though, and correctly modeling the reflection from the Earth's surface is still an area of investigation [159]. Finally, radars can provide measurements at a very high spatial resolution on the order of 10's of meters. Thus, there is interest in using radars to estimate soil moisture and biomass because of the potential gains in resolution and the all-weather, day or night sensing capability of radars. The reflectivity or backscattered energy that a radar measures is generally stronger or brighter when there is more water in the soil. However, the backscatter is also a function of several other variables: frequency, polarization, the incidence angle, soil roughness, plant structure, and material composition. This means that it is difficult to correctly interpret radar

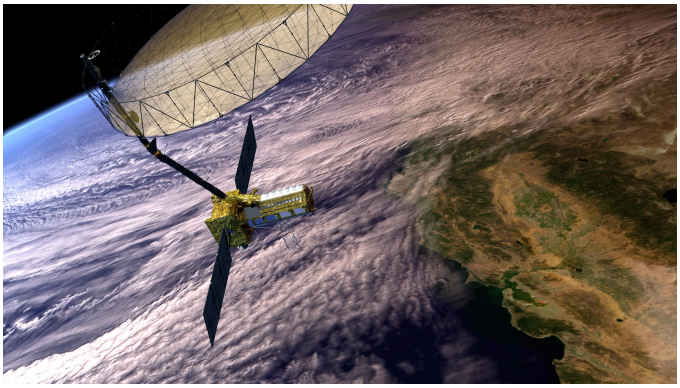


Figure 1.1: NISAR satellite concept art.

measurements and relate the backscatter to a specific amount of soil moisture or biomass.

Researchers have sought to find a reliable algorithm that can make accurate inferences about physical variables like SMC from radar data. They have done this by developing scattering models that define the relationship between all physical variables (biomass, frequency, etc.) and the backscatter. This type of model is called a *forward* scattering model. The forward model attempts to encapsulate everything that is known about radio wave scattering in vegetation. The forward model can then be used to develop an *inverse* model that can make predictions about physical variables based on radar measurements.

An accurate inverse model would be a valuable tool to have in the coming years to help track climate changes and enable efficient agricultural practices for a growing global population. Organizations may have seen these needs because there has been an increase in the amount of radar data that is and will be available. There are already several radar-equipped satellites in orbit like RADARSAT-2 from the Canadian Space Agency (CSA), the SENTINEL-1A satellite from the European Space Agency (ESA), ALOS-2 from the Japanese Aerospace Exploration Agency (JAXA), and SAOCOM from the Argentinian Space Agency. There are also several commercial companies that have begun to field constellations of radar-equipped satellites including CapellaSpace, Iceye, and Umbra Space. An important addition to this list is the NISAR satellite, a joint venture between the Indian Space Research Organization (ISRO) and NASA that is shown in Fig. 1.1. Collectively, these satellites and others can provide frequent passes over the same areas with multiple frequen-

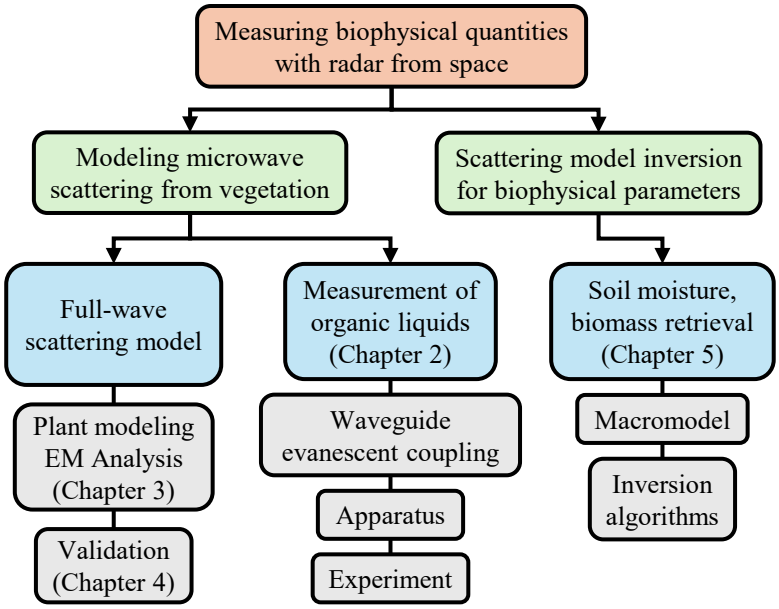


Figure 1.2: Outline of research topics in this dissertation.

cies and look angles. A good inverse model will be invaluable for interpreting the information these satellites have and will collect.

1.1 Research Objectives

In this dissertation, I primarily investigate novel forward and inverse scattering models for measuring soil moisture and above-ground biomass with radar, with a special focus on maize or corn plants. These models are particularly intended for air- or space-borne radars. I also investigate a method for characterizing the dielectric constant of liquids, as well as a technique for partially separating the radar reflection from plants and that from the underlying soil surface. These topics and their corresponding chapters are outlined by Fig. 1.2. The objectives of this study are also summarized as follows.

1. Develop a high-fidelity forward scattering model for radar measurement of corn fields throughout a growing season and as a function of radar attributes like the incidence angle, look angle, polarization, and frequency.

2. Develop an inverse model from the forward model that can accurately estimate SMC and biomass from radar measurements.

3. Develop a method to characterize the dielectric constant of liquid from plants.

1.2 Background

The objectives of this dissertation will contribute to what is an already large area of research. Thus, to give context to this work's contributions, the next four sections discuss some relevant background topics. The first two discuss forward and inverse scattering models to indicate some of the challenges associated with sensing SMC and biomass with radar. The last section provides background on measuring the electrical properties of soil and plant materials.

1.2.1 Forward Model for Predicting Radar Backscatter

Several models for characterizing radar signals from vegetation have been proposed over the past several decades. They generally fall into one of the following categories: empirical or semi-empirical models, analytic models, and numerical models. The empirical approaches generally work by taking detailed measurements of any parameters of interest simultaneously with radar measurements. The measured data can then be used as a lookup table or fitted to linear or non-linear equations. The early modeling work with corn was semi-empirical [144]. The analytic methods attempt to derive the relationship between backscatter and physical parameters from first principles. The numerical approaches rely on discretizing Maxwell's equations to explicitly solve for the scattered fields from an arbitrary structure.

Much of the previous research has favored semi-empirical and analytic approaches. Semi-empirical approaches often work well for the specific area and plant type that is studied, but beyond that they may not generalize well. They are still useful and are still developed [54, 78, 12, 164], and some notable examples are models developed by Oh [99] and Dubois *et al.* [32, 31]. Analytic models do much better at generalizing to different scenarios. They can be less accurate because the

scattering process is quite complex, and analytic models must make some simplifying assumptions to arrive at a workable solution. Numerical models, for the most part, keep all the complexity of a specific scattering scenario, and can thus take a more holistic consideration of a particular scattering scenario. This comes at an increased computational cost, however. The analytic approaches are important to be familiar with, and some background on them is given in the following section, which is then followed by some background on numerical models.

1.2.1.1 Theoretical Models

Traditionally, there are three scattering problems to consider when constructing an analytical scattering model for agricultural vegetation. The first is scattering from a rough soil surface; the second is scattering from a collection of plants; and the third problem is when the collection of plants is in close proximity to a rough soil surface.

Scattering from rough surfaces has been studied for quite some time. The first model for rough surface scattering was the Small Perturbation Method (SPM) [109], which could accurately model scattering from only slightly rough surfaces, which are surfaces where the Root Mean Square (RMS) height and correlation length are both much smaller than the incident wavelength. SPM formulations typically only provide only first-order co-polarized and second-order cross-polarized scattering coefficients, but efforts have been made derive second-order approximations for all of the scattering coefficients [120]. The next approximate model was the Kirchoff Approximation (KA) [13], and it could handle rough surfaces at the other side of the roughness spectrum where the soil's roughness mostly consisted of gentle slopes that are much larger than the wavelength. The equations of KA can be evaluated with *geometric optics* [139] or *physical optics*, depending on if the scattering is dominated by specular reflections or if there is some additional diffraction.

Both SPM and KA had limited applicability for microwave radar observations. This led to the development of the Integral Equation Method (IEM), which can handle the intermediate case when the roughness characteristics of the surface are comparable to the wavelength [43]. It was later improved to calculate bistatic scattering as an *improved* IEM, or I^2EM [44], and then again to

account for multiple scattering at high incidence angles as an *advanced* IEM, or AIEM [157] [158]. I^2EM and AIEM represent the state of the art for analytic scattering models of rough surfaces, and both show excellent agreement with measurements for their regions of validity.

The second problem to address in scattering from vegetation is to model scattering from a collection of particles, or volume scattering, and this has been approached in a couple of different ways. In one approach, the collection is represented by a continuous medium with small, continuous fluctuations in its dielectric constant throughout it, which could be termed a kind of blue-cheese representation. A second approach uses discrete particles like spheres, cylinders, disks, or needles placed in free space to represent different plant components in the volume or canopy. Because of that, it is often important to make detailed measurements of the plant being studied to correctly parameterize each particle's shape [22, 89, 131]. Both approaches can have an *incoherent* or *coherent* formulation model based on whether just power flow is analyzed, or if Maxwell's equations are used to keep track of the phase, respectively.

Most incoherent solutions are based on Radiative Transfer (RT). This solution only looks at how the wave's intensity or power density is scattered and absorbed by clusters of particles. This can be applied to a blue-cheese type medium [143] or a group of discrete particles [142]. An important incoherent approach is the Water Cloud Model (WCM) [6], which replaces a vegetation canopy with an equivalent medium that consists of a layer of water particles distributed throughout it. It is still currently used in practice in various forms because of its simplicity and reasonable accuracy. Several other approaches, which are modifications of WCM or RT, have been investigated that employed different layers for the canopy and trunk [147, 83], used an anisotropic medium to better match vertical plant structures (e.g. stalks) [145], or used a 2D ABCD analysis to treat periodic structures (i.e. corn rows) [124]. Incoherent solutions can only predict the average scattered power from a particular distribution of particles or dielectric fluctuations.

Coherent formulations use Maxwell's equations to derive scattering from heterogeneous mediums or particles. This formulation tracks the amplitude and phase of all fields in the medium. There is some variation in how coherent formulations are used such as taking periodic structure

into account for corn or agricultural crops [89, 135, 137], accounting for tall scattering elements (grass, stalks) with dipoles [135], extending the analysis to include second-order interactions for short, branching vegetation [26], accounting for multiple plant species and structures [19], or using fractal methods for generating geometric plant models [73].

Coherent approaches usually make use of three approximations: the Distorted Born Approximation (DBA), Foldy's approximation, and a single-scattering approximation. The DBA specifies that a particle in a collection of scatterers is illuminated by the mean wave. The mean wave models the extra propagation and attenuation that a plane wave would experience moving through a sparse collection of electrically small scatterers [70]. The propagation and attenuation constants for DBA are typically specified using Foldy's approximation, which is that the free space propagation constant is modified by the forward scattering characteristics of particles in the medium. Finally, the single-scattering approximation only considers field interactions where energy is scattered off a particle just once. This approximation leads to Single Scattering Theory (SST) models, and it can also be applied with incoherent approaches, in which case the coherent and incoherent solutions are effectively equivalent. It has been shown that the single-scattering approximation tends to overestimate forward scattering from clusters of electrically large particles [65].

The third type of problem is when there are scattering particles or objects in close proximity to the soil surface. This has been studied by considering the similar problem of scattering from a sphere (or cylinder) in close proximity to a ground plane. The research on this problem highlights an important difficulty in obtaining an analytic solution. Researchers often tackled the sphere-ground problem by representing the fields in the system with a spherical harmonic basis. Doing this leads to sphere-surface interaction terms whose evaluation requires the numerical integration of complex exponential functions. This feature makes the exact solution somewhat inaccessible [80]. Thus, approximate solutions were derived that are only valid when the distance between the sphere and surface was more than a wavelength [151].

There is always some portion of a plant that is in close proximity to the soil surface (and perhaps partially buried in it). This has meant that only approximations are available for predicting

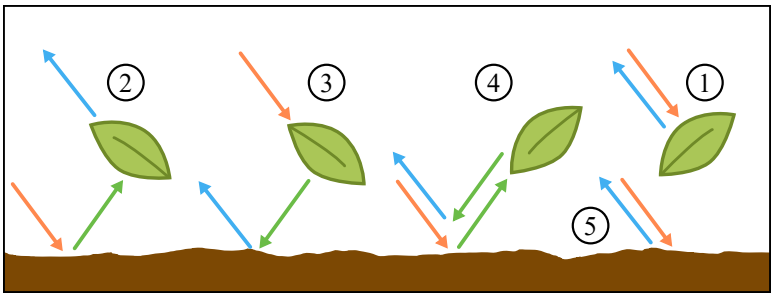


Figure 1.3: Model of scattering processes under a single-scattering assumption: (1) direct, (2,3) direct-reflected, (4) indirect, and (5) rough surface.

the interactions between the plant structure and the soil surface. The most common approach is to use the single scattering assumption along with the far-field scattering characteristics of the soil surface and plant particles. In this approach, there are five scattering mechanisms that contribute to the total observed backscatter, and they are diagrammed in Fig. 1.3. The first mechanism (1) is direct scattering from a single plant component, where the incident mean wave is shown with an orange arrow, and the wave scattered toward the radar is shown in blue. The second and third mechanisms are the direct-reflected paths, which describe similar scattering trajectories, just in the opposite order. In the second mechanism, for example, the mean wave illuminates the soil first and then reflects towards the leaf, with the intermediate reflection being shown by the green arrow. The leaf then scatters that reflection back toward the radar. The third mechanism goes in the opposite order. The fourth mechanism occurs when the mean wave reflects off the ground toward the leaf, and then the reflection from the leaf bounces off the ground again toward the radar. The final mechanism is the direct backscatter from the rough soil surface. The reflections from the soil surface are taken into account by using the Fresnel reflection coefficient for each of the interactions, and an attenuation factor can also be included which takes the soil's roughness into account. The reflections from the particles are defined by their far-field bistatic or backscatter scattering amplitudes. This model of the scattering process is also referred to as the four-component approximation when neglecting scattering from the soil surface.

1.2.1.2 Computational or Hybrid Models

As mentioned, analytic models rely on a few approximations (e.g. DBA, single scattering) to arrive at a workable solution for predicting the backscatter from a collection of plants. Those approximations generally simplify the multiple scattering interactions that take place between the soil and plants. The interactions can be explicitly accounted for using an electromagnetic numerical solver such as the finite-difference time-domain method (FDTD), the method of moments (MoM), or the finite element method (FEM). These solvers discretize Maxwell's equations to solve electromagnetic problems for nearly arbitrary structures and materials. Because of that, a numerical solver can work with a more accurate plant shape without resorting to the cylinder and disk representation that analytic methods may employ. Plant scattering models based on numerical solvers can thus produce higher fidelity results than their classical counterparts. The main drawback of using numerical solvers is that significantly more computational power and time are needed to produce results.

It may be for that reason that work with computational models has been limited. However, there has been recent effort devoted to their development. A MoM solver was used by Huang *et al.* [56] to predict the backscatter from rough surfaces as a function of several variables. They termed their solver the numerical Maxwell model in three dimensions (NMM3D). Their work indicated that even sophisticated models like I2EM may still not be entirely accurate. For scattering from vegetation, the work by Park *et al.* analyzed transmission through a set of long cylinders with periodic boundary conditions, which could serve as a rough model for a stand of corn plants [106]. One final example is the work by Gu *et al.* [49]. They used a numerical-analytic hybrid method which combined results from a MoM solver together with vector cylindrical wave expansions and the Foldy-Lax multiple scattering equation to predict transmission through a wheat field. The same approach has been applied to corn, but there is some difficulty there because the hybrid approach cannot yet handle overlap between plants, which is a common feature in corn fields [45]. Additionally, these approaches do not yet include effects from a soil surface.

Whether the model uses analytic or numerical methods, there is an important consideration to

point out. Models can have high fidelity descriptions of a plant's geometry in order to achieve more accurate results, but that requires a long list of needed input parameters. Some models, on the other hand, only need a few different parameters to make a prediction about the scattering. Both extremes have their drawbacks. For few-parameter models, their drawback may be lower accuracy. For many-parameter models, there is a problem where many different scenarios of input parameters may give backscatter predictions that are very close to each other, or even the same. This can be a problem when using a forward model to infer information about any of the input parameters when backscatter data is available. This issue brings us to the next background topic: inverse models.

1.2.2 Inverse Models for Physical Parameters From Radar Backscatter

Inverse problems try to estimate some quantity based on indirect observations of that quantity. One example would be to estimate the initial temperature profile on a metal bar using the observed temperature profile after some time has passed. This seems reasonable, however inverse problems are notorious for being difficult to work with because they are often *ill-posed* problems, which is a term coined in the 20th century by Hadamard [50]. A *well-posed* problem has the following characteristics: (1) there is a solution (existence), (2) there is only one solution (uniqueness), and (3) the solution varies continuously with data or initial conditions (stability). An ill-posed problem will not satisfy one or more of these requirements. With a system of linear equations, for example, a lack of stability can manifest as an ill conditioned matrix.

Despite the challenge of inverse problems, the second part of this work attempts to develop an inverse model for estimating physical parameters of a corn field from the radar backscatter. In this case, many-parameter scattering models for vegetation present a challenge because a radar only provides a few independent measurements, perhaps three, from one observation. This means that only three parameters at most can be estimated unless additional observations or other data sources are used. Thus, the character of a forward scattering model may be well described as a surjective function as illustrated by Fig. 1.4, where each element of the function's output is mapped

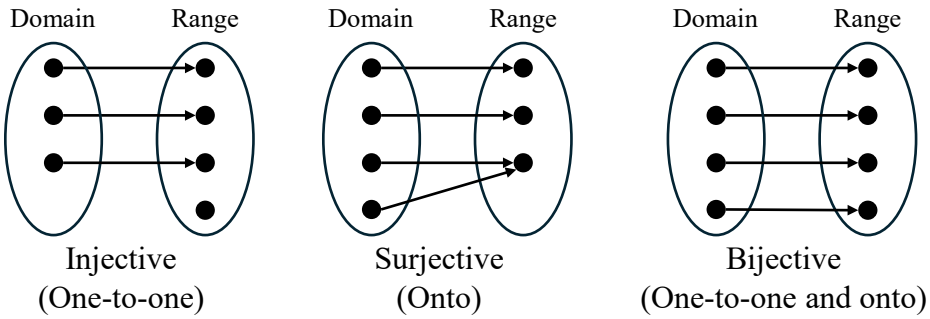


Figure 1.4: Different mapping classifications for functions.

to by *at least* one element from the function's domain. This scenario is equivalent to having an underdetermined set of equations. It inherently makes the forward model non-invertible from a rigorous standpoint and violates the uniqueness condition of a well-posed problem. Additionally, radar measurements are always corrupted by some amount of noise.

Nonetheless, even with an underdetermined problem, reasonable solutions can still be obtained. The typical approach that others take to deal with an ill-posed problem is a broad class of techniques that are referred to as *regularization*. Regularization can add more information to an underdetermined problem by adding prior information, penalties on the final solution, or additional constraints. This has allowed others to obtain estimates for physical parameters from radar data. There are perhaps four kinds of approaches for making an inverse model. The first approach is semi-empirical. These methods often use an already existing semi-empirical model, and then simply invert it for the parameter of interest [15, 74]. Like empirical models, these models have several coefficients that need to be calibrated to a specific scenario for the best performance. The models by Dubois *et al.* [32], Oh [99], and the WCM are good examples of forward models that support this approach.

The second type of approach that is specific to soil moisture sensing is based on change detection. Even without vegetation present, it's difficult to correctly parameterize soil conditions when attempting to estimate the SMC. A way around this is to assume that the soil's roughness or vegetation cover does not change significantly with time. Then, any changes in the backscatter over a short time period can largely be attributed to changes in soil moisture. Thus, these meth-

ods often compare a new measurement with a reference measurement that comes from bare, dry soil conditions [152, 104, 103]. The third approach relies on machine learning methods to specify the relationship between radar measurements and SMC or biomass. Most of the machine learning techniques like regression, random forests, vector support machines, artificial neural networks (ANNs), and convolutional ANNs have been explored [74, 9, 105, 67, 93, 130, 114, 113]. The data that the algorithm is trained on could be measured in situ data or data produced by analytic or numerical models. Finally, there are some approaches that take an ad hoc approach to making estimates. They rely on heuristic reasons for how the algorithm is developed. One example is the work by He *et al.* [53], which used a polarimetric decomposition to isolate different scattering mechanisms, and then used one of two empirical formulas to get the SMC, depending on which scattering mechanism is dominant.

The success of an inverse model depends on the data or forward model it is based on. If it is based on an analytic or numerical forward model, then it is equally important for that forward model to produce accurate backscatter predictions. Correctly characterizing objects is an important aspect of making good forward models, and part of that characterization is measuring the electrical properties of soil and plants. The next section reviews some important techniques that are used to measure the electrical properties of soil and plant material.

1.2.3 Electrical Characterization of Soil and Plant Material

There are several methods available at microwave frequencies for measuring the dielectric constant or permittivity of a material. They can be divided into resonant and non-resonant methods. Resonant methods do very well at measuring the dielectric constant or permittivity at one frequency. With the right modifications, they can also accurately measure materials with high dielectric loss. It is typically quite difficult, though, to use one system to measure the dielectric constant at multiple frequencies. This is because the physical apparatus of the measurement system needs to be tuned to work at another frequency, and this is often difficult or impossible. If a broadband characterization of a material's permittivity is desired, then a non-resonant method is more appropriate.

The apparatus in these methods does not need to be physically changed to work at a different frequency. However, these techniques do not work well with lossy materials. Thus, there is a tradeoff between dielectric accuracy and spectral range when selecting between one of these methods.

A well-known resonant technique is the resonant cavity. This is often a hollow, metal cylinder that is machined to specific dimensions so that it resonates at the desired frequency. It is filled with the material to be tested or the material under test (MUT) to determine its permittivity. This procedure cannot measure lossy materials well, but there are two techniques that allow it to do so. The first is to only partially fill the cavity with the MUT. The second is to place a small cylinder of the MUT material inside the cavity. These are known as the partially-filled cavity and cavity perturbation techniques. A second resonant technique is one that is based on a resonant microstrip circuit [121]. It benefits from the fact that the MUT does not need to be ground into a powder or machined to a specific shape. Only a flat surface on a bulk of the MUT is required. However, the approach is less accurate for lossy materials because the fields generated by the resonant circuit are allowed to expand.

Non-resonant methods for measuring a material's permittivity often rely on how a traveling electromagnetic wave interacts with the material. A common example of this method is the coaxial probe method. In this method, one end of a coaxial cable is cut open to expose the center conductor, dielectric and shielding. That end of the cable can then be pressed against the MUT, and a detector will measure the amount of reflection from the end of the cable to determine the permittivity. This is a very versatile method in terms of the situations where it might be used: against a solid bulk of material or in a liquid. And because the technique is non-resonant, it can measure the permittivity across a wide range of frequencies that is only limited by the detector and coaxial cable. A second set of non-resonant techniques is based on the use of waveguides. In one method, a thin slice of material with the same shape as the waveguide's cross-section is inserted into a waveguide, and a detector then measures the reflectivity from the slice to determine the permittivity [126]. The drawback with it, though, is that the material needs to be shaped to the precise dimensions of the waveguide.

A variety of these methods have been used to measure the permittivity of soil and plants. A seminal work relating the permittivity of plants to their water content are two papers by Ulaby, El-Rayes *et al.* [37, 145]. They conducted many experiments to formulate a theoretical model relating plant water content and the permittivity of plant tissue. They used the open-ended coaxial probe method to obtain experimental data on the permittivity of plant tissue. The probe method has also been used by Sharma *et al.* [131] to estimate the permittivity of nodes and internodes along a corn plant's stem. The waveguide method was used by Sarabandi *et al.* to determine the permittivity of plant leaves [126]. For measuring the permittivity of soil, widely used measurements were made by Hallikainen *et al.* [51]. They used two transmission-based methods, where the first involved comparing transmission through a waveguide to a reference waveguide, and the second used a free-space transmission method where radio waves were transmitted through the MUT. Another dataset of soil moisture measurements was also made by Curtis *et al.* [29]. They used a specially-made coaxial transmission line where the space between the center conductor and the shielding could be filled with soil material so that it would act as the dielectric fill for the transmission line. The permittivity would then be measured based on transmission through the line.

It is important to obtain accurate dielectric measurements that a forward or inverse model can be based on for measuring physical parameters with radar.

1.3 Methodology

The main topic of this work is to investigate different methods for sensing physical quantities with radar observations, with a special focus on sensing SMC and biomass or Vegetation Water Content (VWC) in corn fields. This is primarily addressed by developing a numerical radar scattering simulation that accurately mimics the scattering processes which take place in real-life scenarios. That scattering simulation provides a forward model that can predict the relationship between SMC and VWC and the radar backscatter coefficient. That relationship is then approximated with a macromodel that allows its behavior to be predicted over a wide range of scenarios. This solves the

problem of modeling the scattering from a corn field based on what its physical conditions are. The next step is to develop an inverse model or algorithm to do the reverse: sensing those conditions from backscatter measurements, constrained by the relationships derived from the forward model. The inverse model that is used is based on iterative, non-linear, regularized inversion and a residual artificial neural network, which is trained on the data produced by the forward model. This allows it to work out the complex relationship between the backscatter coefficient and the SMC and VWC. The inverse model then allows predictions to be made about those parameters given measured backscatter coefficients from corn. The performance of the inversion algorithm is assessed with measured, experimental data.

An important piece of this methodology lies in the need to electrically characterize plant components. A novel sensing technique for the dielectric constant of liquids is investigated that also makes use of inverse models, and it could be used for measuring the permittivity of fluid from plants. The last section of this chapter gives an outline of the topics in this work.

1.4 Dissertation Outline

An outline of the topics in this dissertation is illustrated in Fig. 1.2. Chapter 2 investigates a dielectric measurement technique that has special application for measuring the permittivity of liquids. It also requires the use of a numerical forward model and a regressive inverse model. In this case, the forward model is relatively simple and uses the coupling through a narrow waveguide channel operating in the cutoff region to provide estimates of the dielectric constant. The forward model is based on a full-wave numerical solver, and the computational cost is low. Additionally, the forward-inverse function is well-behaved so that a straightforward correspondence can be established between the microwave measurement and the estimated dielectric value. The design of the waveguide coupling structure, experimental procedure, data processing methods, and measurements of dielectrics using the apparatus are described.

Chapter 3 develops a full-wave scattering model for corn plants. It describes how the simulation

is set up and how each component of a corn plant is modeled. This includes the use of periodic boundary conditions in the computational domain and representing leaves with impedance surfaces. This chapter also justifies the modeling approach with analytic or simulated results.

The methodology in Chapter 3 is then validated for corn fields in Chapter 4. This is done by using data-based 3D models of corn plants to accurately represent the geometry in the methodology of chapter two. Chapter 4 also discusses the trade-off between computation time and radiometric accuracy because of how computationally intensive the full-wave model is. The 3D models are then used in the simulation methodology with in-situ data of biophysical parameters to make predictions of the radar backscattering coefficient that are then compared with data from real observations to validate the approach. The simulation results are also compared with lab measurements that use artificial plant structures.

Chapter 5 builds on the forward model described in the third and used in the fourth chapter, which is essentially a function that relates physical parameters to measurable radar quantities like the backscattering coefficient. This chapter describes an algorithm that estimates physical variables from radar measurements. The algorithm combines iterative, nonlinear regularized inversion, a classical inversion method, with a machine learning tool, specifically a residual artificial neural network or ResNet. The inversion algorithm requires the forward model to be evaluated for many different scattering scenarios. However, the forward model is computationally expensive to evaluate, and thus a limited database of representative scenarios is first created with the forward model. This database is then interpolated to create a spline-based forward macromodel that can be readily used by the inversion algorithm. The inverse model is then used to retrieve physical parameters from real radar measurements, and its performance is evaluated against experimental data.

Finally, Chapter 6 provides a summary of the work presented in this dissertation. Some avenues for future research are also discussed.

CHAPTER 2

In-line Dielectric Measurement Apparatus for Liquids

2.1 Introduction

The need for non-invasive, non-destructive, real-time measurement of liquid properties is widespread in industrial, agricultural, and scientific applications [97, 47, 117, 115]. Several specific applications include: measuring the purity of aqueous solutions for scientific experiments; the manufacture of medicines; quality control during the malting and fermentation of beer, whiskey and other alcohols; measuring sugar levels in beverages in the food and drug industries; and finally in measuring bio-markers in blood, urine and biological tissues [85, 102, 3]. The standard measurement techniques used in these applications are biochemical assays, spectroscopy, and radio frequency (RF) measurements. Biochemical assays can provide an accurate chemical composition of a liquid, but are generally very expensive and require a large sample to be collected. Spectroscopy can be accurate, real-time, and non-invasive, but it requires expensive and bulky equipment. On the other hand, RF measurement techniques are low-cost and compact, which makes them highly suitable for certain applications. They are generally based on resonance or propagation phenomena, each having their own advantages [71, 154, 128]. Resonance based techniques have strong field interactions and higher sensitivity, whereas propagation based techniques are broadband. Typically, liquid measurements using the resonance method require a small sample size due to their high loss tangent. The small sample produces a *perturbation* in the resonator's resonant frequency

and quality factor from which the liquid's complex dielectric constant can be extracted. Since only a small shift is observed, the sensitivity of this approach is low. Furthermore, for measuring multiple liquids and time-varying liquids, the samples must be replaced for each measurement, which introduces repeatability errors and is also time-consuming. Therefore, it is desirable to have a measurement technique that is: (1) accurate and sensitive; (2) capable of measuring a wide range of liquids from water to alcohols; (2) able to track dielectric constant changes in real-time; (3) low cost; and (4) easy to fabricate. This paper proposes such a device based on the concept of epsilon-near-zero (ENZ) supercoupling [133, 35].

2.2 Background

The concept of ENZ supercoupling was first introduced by Silverinha and Engheta in [133], where they showed a dramatic field enhancement inside a narrow, rectangular waveguide channel at its cut-off frequency. The most salient features of supercoupling are: (1) the resonant frequency is independent of the channel length and converges to the cut-off frequency as the height of the channel tends to zero; (2) the quality factor increases as the channel length increases or as the channel height decreases; and (3) the waveguide can be bent into different shapes while preserving the supercoupling behavior provided that the channel height is small [34].

There are several ways to interpret these unique features. The most common interpretation is the one provided by Silverinha and Engheta in the original article, where the channel being in cut-off has an effective dielectric constant (ϵ) of zero at the cut-off frequency. They showed that reducing the height of the channel towards zero causes *energy squeezing*, which results in perfect transmission through the channel. Another interpretation is to think of the channel as a Fabry-Pérot resonator with the supercoupling mode serving as the zeroth order resonance. In this case, as the channel height decreases, the reflectivity at the two ends of the channel increases, the finesse factor becomes larger, and the confined fields become stronger. Changing the length of the channel does not affect the resonant frequency since the mode is the zeroth order resonance, which exists

because there is no phase shift through the channel at cut-off. A third interpretation comes from basic waveguide/circuit theory. Assuming the channel length is small, it appears as a rectangular aperture, which may also be represented by an equivalent LC resonator [81]. As the channel length increases, the capacitance increases while the inductance decreases, thereby keeping the resonant frequency constant and increasing the quality factor. Thus, from a circuit perspective, the electric fields inside the channel grow larger for a given voltage excitation, and the quality factor increases. The lumped circuit approximation is valid even for long channels because at cut-off there is no phase shift between its ends. The first interpretation is the most general, as it can be extended to other geometries readily, whereas the second and third interpretations offer intuition and simplified modelling capability without the need for full wave simulations.

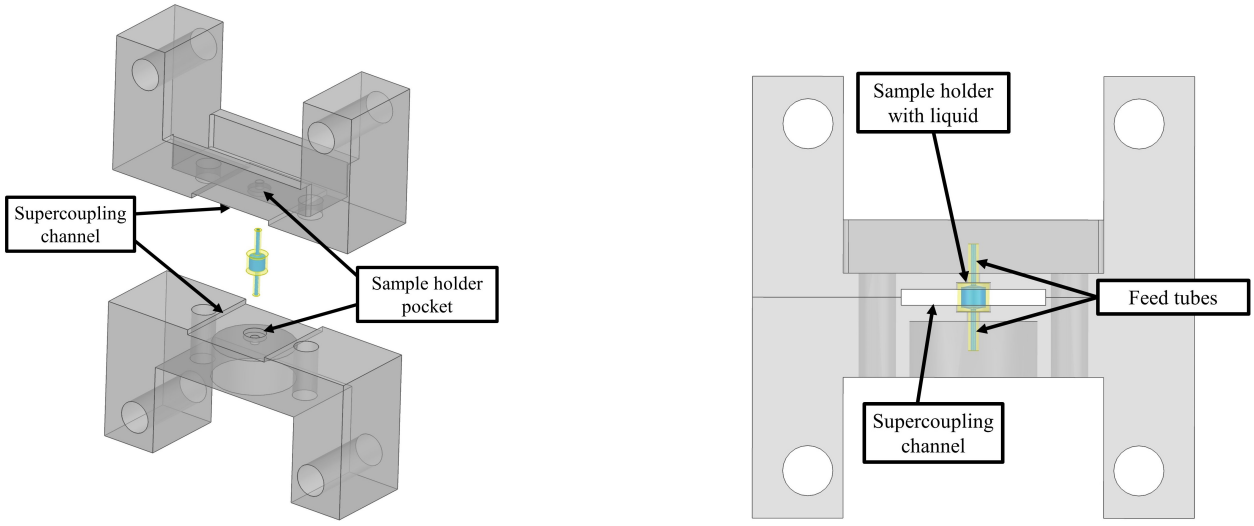
The strong fields inside the channel enhance wave-matter interactions and point to dielectric constant (ϵ) measurements as a potential application [5]. If the channel is taken to be a rectangular waveguide operating in the TE_{10} mode and filled with a material of permittivity ϵ_r, then it can be shown that the ENZ channel presents an effective dielectric constant given by

$$\epsilon_{\text{eff}} = \epsilon_0 \left(\epsilon_r - \frac{c_0^2}{4a^2 f^2} \right), \tag{2.1}$$

where c_0 is the speed of light in a vacuum, ϵ_0 is the vacuum permittivity, f is the operating frequency, and a is the channel width [116]. Since an ENZ channel has zero permittivity at the cutoff frequency, the dielectric constant of the waveguide's filling material is directly given by the cutoff frequency f_c, or

$$\epsilon_r = \frac{c_0^2}{4a^2 f_c^2}. \tag{2.2}$$

Thus, supercoupling and its many variations have been widely used for dielectric constant measurements [132, 24]. Lobato-Morales et al. demonstrated a substrate integrated waveguide (SIW) channel with two cavities and measured the dielectric constant of various solids at C-band [75]. Jha et al. demonstrated the same with binary liquid mixtures at S-band [58]. In both cases, a perturbation was introduced into the channel through a hole that was small enough to prevent energy



(a) Exploded view

(b) Front view

Figure 2.1: Supercoupling device made of machined pockets and micro-3D printed sample holder.

leaking from it. The small hole size limited the strength of the perturbation since the amount of liquid that could be introduced into the channel was small. This is also perhaps the reason for choosing the lower microwave frequency range in their work. As will be explained later in Section 2.3, the sample holder design proposed in this work overcomes this limitation to allow strong field interactions without allowing energy leakage through the feeding pipes.

Other waveguide based resonator measurements of the dielectric constant of liquids have been reported in the literature. In [2, 10], meta-material based resonators are placed inside a waveguide to measure the complex reflection coefficient of liquid samples. However, the sample holder used is large and therefore unsuitable for measuring lossy liquids such as water. The method proposed in this paper is able to measure the dielectric constant of liquids over a wide range of permittivities and loss tangents due to a novel sample holder design described in Section 2.3. Other works like [108, 90, 28, 21, 46, 1] present similar methods, but do not experimentally demonstrate the real-time capability for a wide range of liquids, which is shown in this paper.

In [11], Bao et al. characterized the complex dielectric constant of ethanol-water and methanol-water binary mixtures. Their results indicate that the maximum shift in the real part of the dielectric constant (as the volume fraction of water changes) occurs at around 4-5 GHz, whereas

for the imaginary part the maximum shift occurs at around 11 GHz. Therefore, to maximize the shift in the complex dielectric constant from alcohol to water, in this work the X-band (8 GHz to 12 GHz) is chosen as the operating frequency range. This has an additional benefit of making the device compact and in turn requiring a smaller sample size. However, the smaller wavelength at these frequencies makes the manufacturing and modelling quite challenging. To address these challenges, several techniques are introduced in the design, manufacturing, modelling and inversion steps to achieve a very accurate and sensitive device. The main contributions of this paper are the following:

1. A novel sample holder design is proposed. The design allows for larger liquid samples to be introduced into the device without allowing energy to escape from the resonator. It is also designed to prevent the formation of air cavities which improves repeatability and produces consistent measurements.

2. A forward model is developed and optimized to account for variations in the design due to manufacturing tolerances. A sensitivity analysis is performed to motivate the need for an optimized forward model in order to achieve very accurate measurements. This is a key step to make such a design work at high frequencies since the device is much more sensitive to manufacturing errors.

3. The device is manufactured using high precision CNC milling and micro-3D printing. Since the channel acts like a resonator, the machining accuracy must be very precise to prevent evanescent mode leakage and loss. Several design choices are made to ensure the channel and the sample holder can be successfully fabricated and assembled.

4. An extensive quantitative error analysis is performed to identify and minimize the various possible sources of error in the measurements. This error model is used in the inversion stage to quantify the error in each measurement.

5. Two designs of the device are fabricated to validate the measurement results and demonstrate the trade-off between accuracy and sensitivity.

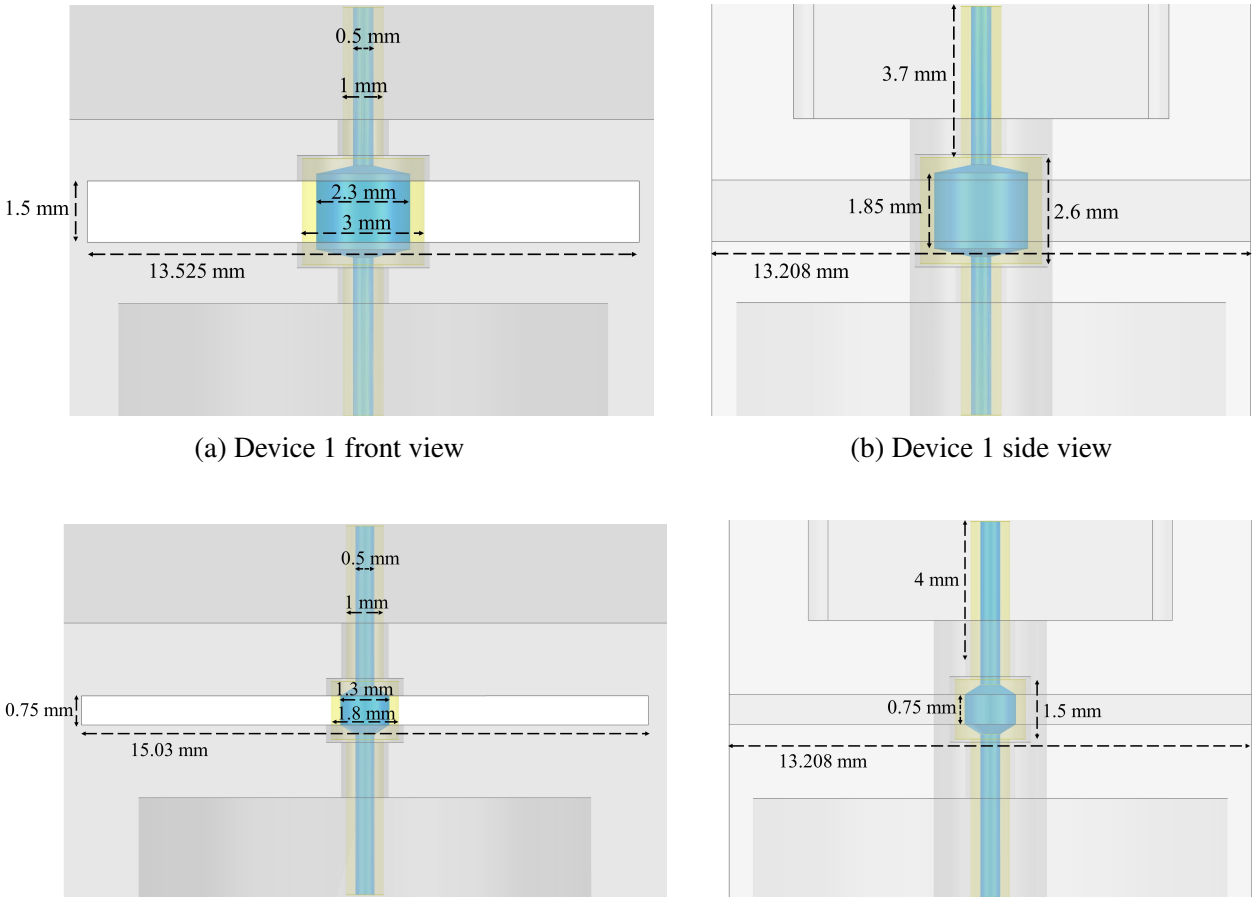
6. Finally, the device is tested in two different real-time measurement scenarios and is shown to agree well with the expected results. It is able to track variations in the complex dielectric constant over time.

2.3 Design and Manufacturing

The design proposed in this paper is shown in Figs. 2.1 and 2.2. It has a large pocket (machined inside the channel) that houses a sample holder chamber connected to two feeding tubes. The novelty of this design over previous works is that the sample holder chamber can be made much larger than the feeding tubes, which cannot be done using SIW channels. This creates a stronger perturbation, allowing for very sensitive measurements at higher frequencies. Additionally, the proposed design does not suffer from dielectric losses since the substrate is air.

The two narrow feeding tubes act as partially filled circular waveguides and must be carefully designed to not allow energy leakage through them. Since water has the highest dielectric constant ($\approx$ 62 at 10 GHz) among the liquids tested in this work, the dimensions of the feeding tubes were chosen to be small enough to ensure that the circular waveguide is operated below its cut-off frequency. The cut off frequency is around 30 GHz for a circular waveguide that is partially filled with water. This leaves a safe margin that accounts for manufacturing tolerances and the possibility of measuring liquids with even higher dielectric constants. The cut-off frequency can be obtained analytically [52] or by using an Eigen-mode solver.

This approach of using waveguide supercoupling with a large pocket machined into the channel was first presented in [92]. However, in the design presented there, the pocket size was small and the sample holder was put together using tubes. In this paper, the sample holder is made using a high resolution micro-3D printing fabrication technique, which admits much larger chamber sizes. The chamber design also prevents air bubbles from being trapped inside it, which is necessary for consistent real-time measurements of a changing liquid mixture. This paper also improves upon the preliminary work presented in [92] by: (1) developing an optimized forward model that accounts



(a) Device 1 front view

(b) Device 1 side view

(c) Device 2 front view

(d) Device 2 side view

Figure 2.2: Cross section (front view) and side view of Device 1 and 2.

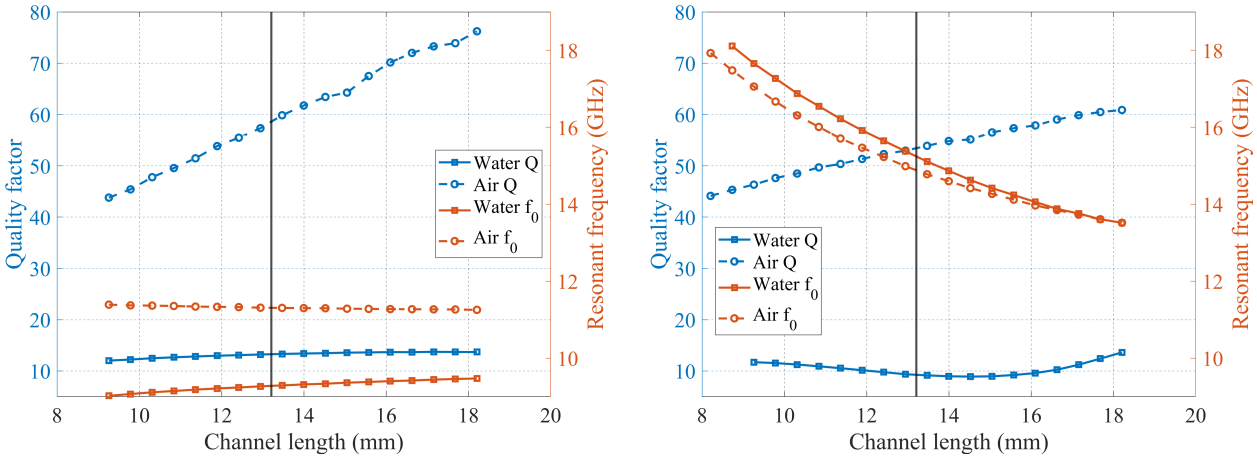
for manufacturing tolerances of the channel and the sample holder; (2) performing an extensive error analysis of the various sources of error to improve the accuracy of the measurements; and (3) designing and manufacturing two variations of the device to corroborate the results between them and optimize them for either sensitivity or accuracy.

The dimensions of the channel and the sample holder are shown in Fig. 2.2. Device 1 is chosen to have a larger channel and sample holder volume to allow stronger interactions between the liquid and the incident field. This produces a larger shift in the supercoupling frequency at the cost of more loss and a lower quality factor. Device 2 is chosen to have a smaller channel height and a smaller sample holder. The smaller height increases the quality factor and the weaker perturbation reduces the loss. Therefore, Device 1 is expected to have a higher resolution since small changes in ϵ produce larger shifts in the supercoupling frequency. Device 2 is expected to have higher accuracy due to the higher quality factor and lower loss. The tapered top and bottom surfaces of the sample holder chamber are designed to allow liquids to flow through without forming air pockets inside it, which improves the repeatability of measurements. Due to the small size of the sample holders, they were printed using a commercial Projection Micro Stereo-lithography technology from Boston Micro Fabrication. The print resolution is 10 μm in both XY and height. The dielectric constant of the sample holder polymer is 3.45 at X-band. The channel and pocket are machined in aluminum with screw holes and access trenches as shown in Fig. 2.1.

2.4 Simulation Results

2.4.1 Parametric Analysis

A parametric analysis is presented to motivate the choice of dimensions used for the two devices (see Fig 2.2). The simulations are run for air ($\epsilon_r = 1$ and $\tan\delta = 0$) and water (ϵ_r = 62 and $\tan\delta = 0.52$) [85] since they represent the two extremes of the liquids being measured. As mentioned earlier, the channel acts as a Fabry-Pérot resonator with the zeroth order mode corresponding to the supercoupling mode and the first order mode corresponding to the Fabry-Pérot resonance.



(a) Device 1 supercoupling mode

(b) Device 1 Fabry-Pérot mode

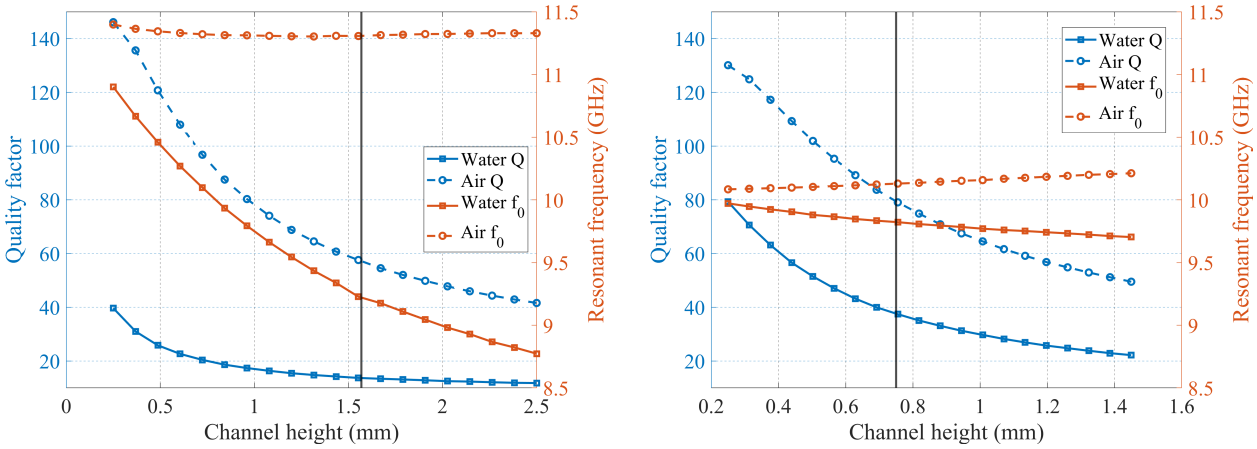
(c) Device 2 supercoupling mode

(d) Device 2 Fabry-Pérot mode

Figure 2.3: Channel length sweep comparison between the supercoupling mode and the Fabry-Pérot mode. The black lines indicate the chosen design values.

Figure 2.3 shows a comparison between the two modes for air and water as a function of channel length. Here, channel length is the dimension along which mode propagation occurs inside the waveguide. As expected, the supercoupling mode's resonant frequency does not change much when the channel length is increased. However, what is of interest is the variation in resonant frequency as the dielectric constant is changed.

Taking the two extremes of air and water, the difference between their resonant frequencies should be large for better sensitivity. The Fabry-Pérot mode for both devices has a very small shift

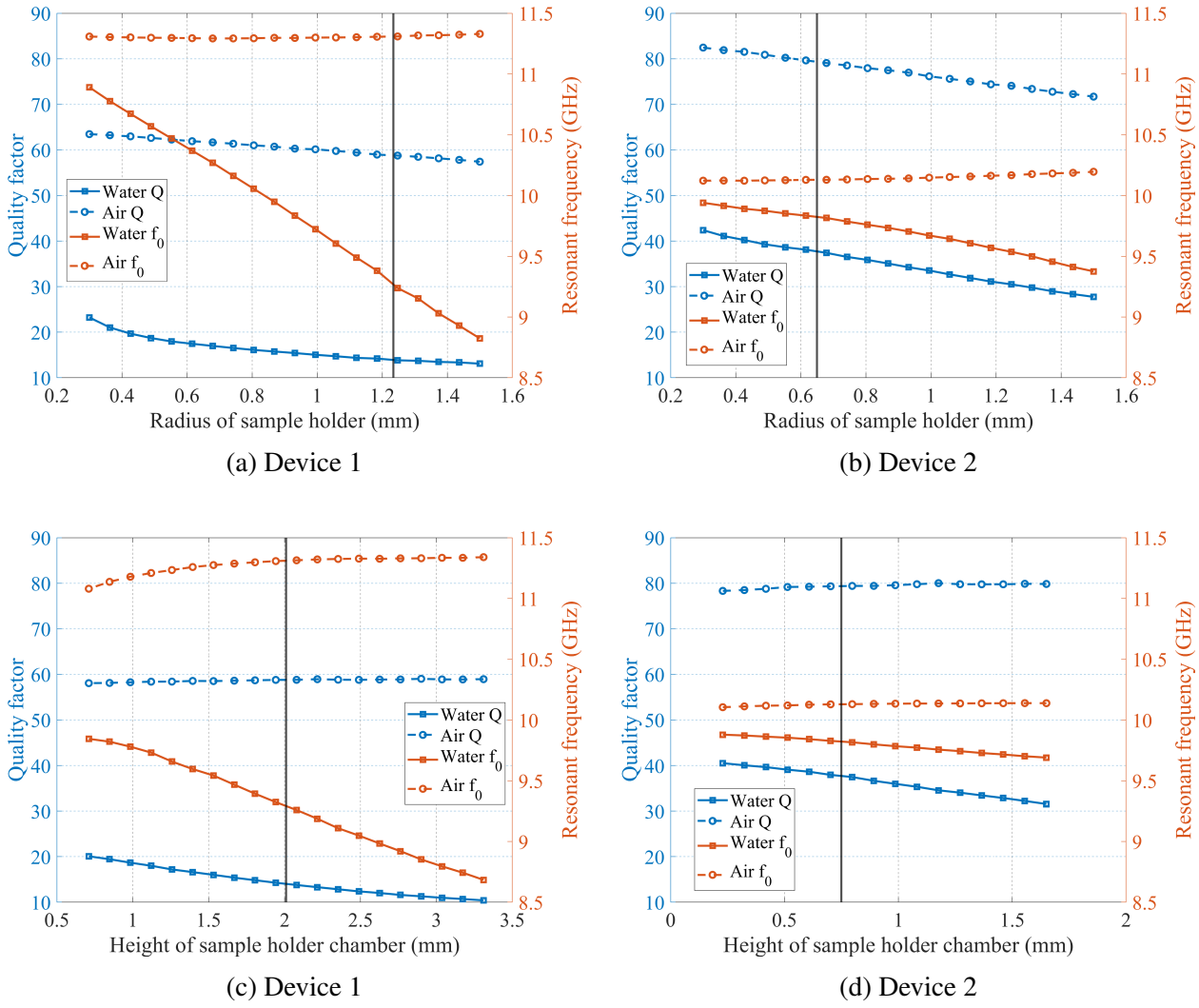


(a) Device 1 (b) Device 2

Figure 2.4: Channel height sweep comparison between Device 1 and 2. The black lines indicate the chosen design values.

in frequency from air to water. On the other hand, the large difference in the case of the supercoupling mode is attributed to the field enhancement inside the channel. This validates the choice of using the supercoupling mode over the Fabry-Pérot mode for dielectric constant measurements. Note that Device 1 has a higher sensitivity due to the larger shift in f_0 from air to water. On the other hand, Device 2 has a higher quality factor and hence a higher accuracy. This trade-off between accuracy and sensitivity (or resolution) is highlighted later in Section 2.7. The black vertical lines in Figs. 2.3, 2.4 and 2.5 correspond to the parameter values chosen for each device.

Starting from the dimensions shown in Fig. 2.2, the height of the channel is swept and the resulting resonant frequency and quality factor are shown in Fig. 2.4. The quality factor drops with increasing height since the finesse factor of the resonator decreases. For Device 1, the resonance frequency (with an air medium) remains stable since the cut-off frequency of the channel does not change with its height. However, the resonance frequency of water decreases as the channel height increases because a larger volume of the sample holder comes into the channel and produces a larger perturbation. This effect is weaker in Device 2 since the sample holder radius is smaller. Again, for Device 1, the change in resonance frequency Δf_0 is larger, while the quality factor is lower. The nominal values of the two devices are chosen in the middle of the sweep range based



(a) Device 1

(b) Device 2

(c) Device 1

(d) Device 2

Figure 2.5: Sample holder chamber radius and height sweep comparison between Device 1 and 2. The black lines indicate the chosen design values.

on the manufacturing constraints of the sample holder.

Next, the dimensions of the sample holder itself are varied and the results are shown in Fig. 2.5. As expected, the quality factor deceases with radius and height since the sample holder and water have a non-zero loss tangent. Interestingly, there is a slight increase in the resonant frequency as the volume of the sample holder increases when the medium is air, while the opposite effect is observed when the medium is water. The change in frequency is larger for Device 1 since the channel height is larger. The nominal values of the sample holder dimensions are chosen to be larger for Device 1 in order to further increase Δf_0. Several other parametric sweeps were conducted to optimize the

Table 2.1: Sensitivity of ϵ_r and $\tan\delta$ from Device 2 with respect to several key parameters and different sample liquids, assuming $\tan\delta = 0.4$ for each liquid.

Liquid ϵ_r	10		25		40		55		62	
Parameters	$\Delta\epsilon_r$	$\Delta\tan\delta$	$\Delta\epsilon_r$	$\Delta\tan\delta$	$\Delta\epsilon_r$	$\Delta\tan\delta$	$\Delta\epsilon_r$	$\Delta\tan\delta$	$\Delta\epsilon_r$	$\Delta\tan\delta$
Liquid radius	1.7	0.03	5.2	0.001	7.9	0.02	10	0.03	11.2	0.03
Liquid height	0.7	0.03	2.9	0.008	4.7	0.003	6.6	0.01	6	0.004
Pocket depth	0.01	0	0.11	0	0.6	0.007	0.1	0.004	1.2	0.002
Channel width	4.1	>4	>40	>4	>40	>4	>40	>4	>40	>4
Channel height	1.2	0.22	4.5	0.17	7.4	0.13	1.11	0.11	11.8	0.11
Chamber ϵ_r	0	0	0	0	0	0	0	0	0	0
Metal σ	0.1	0.01	0.02	0.003	0.04	0.003	0.43	0.005	0.2	0.002

two designs while keeping in mind the manufacturing constraints in machining and 3D printing.

2.4.2 Sensitivity Analysis

A sensitivity analysis is presented here to show which design parameters strongly affect the values of ϵ_r and $\tan\delta$ that the devices may measure. This is provided by Table 2.1 for device 2. The sensitivity is analyzed with respect to seven parameters: the sample holder chamber's radius and height, the depth of the machined pocket, the supercoupling channel width and height, the dielectric constant of the sample holder, and the conductivity of the metal used to construct the device. First, each of these parameters is simulated at $\pm 5\%$ from the nominal value. The resulting f_0 and Q from the simulations are then used to extract a corresponding ϵ_r and $\tan\delta$ based on an inverse model detailed later in Section 2.5. Table 2.1 is then populated with the difference in the simulated dielectric properties ($\Delta\epsilon_r$ and $\Delta\tan\delta$) that occurred from the $\pm 5\%$ perturbation. This is done for several representative values of ϵ_r: 10, 25, 40, 55, and 62. A loss tangent of 0.4 is used for each ϵ_r value. The table shows that the chamber radius, the chamber height, and the channel height significantly influence the dielectric constant. It is also extremely sensitive to the channel width. A $\pm 5\%$ change in that parameter is enough to move f_0 out of its typical range. Since these key dimensions are subject to tolerances during manufacturing, this motivates the need for a rigorous

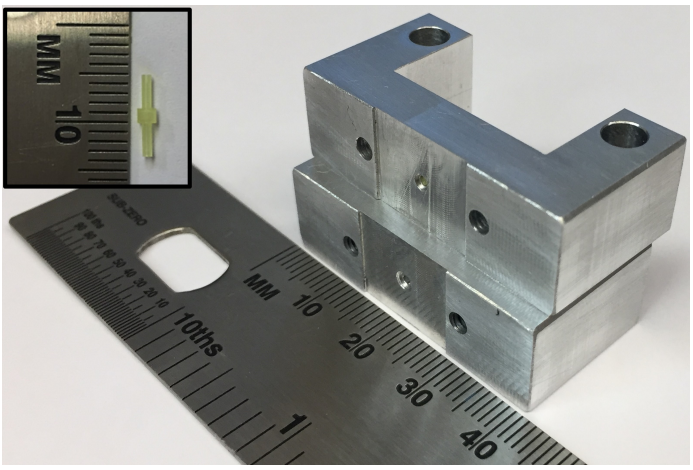


Figure 2.6: Close up of the sample holder/chamber (yellow in inset image) and the top and bottom halves of Device 2.

forward model that captures these variations in order to account for them during the inversion stage. The details of the forward and inverse model are presented later on in the next section.

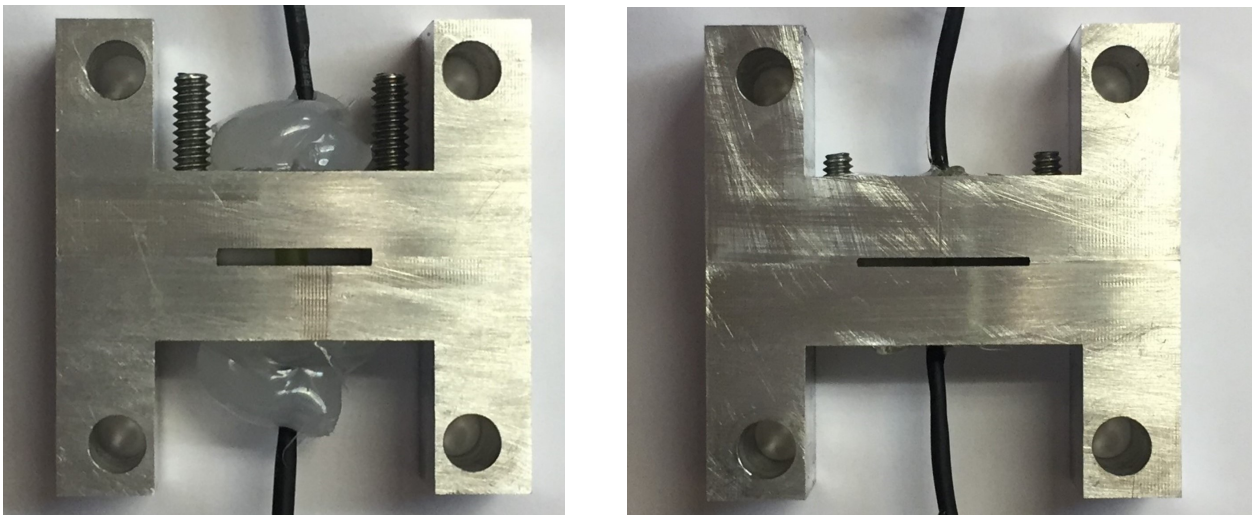
2.5 Methodology

The supercoupling devices described in Section 2.3 were used in several experiments to measure the dielectric constant of mixtures of alcohol and water. This section describes how the devices were set up for these experiments.

2.5.1 Experimental Setup

2.5.1.1 Device Assembly

The devices were manufactured in three parts: the sample holder, a top half, and a bottom half, which are shown in Fig. 2.6 for the case of Device 2. The devices were assembled by placing the sample holder in the machined pocket and screwing the two halves together tightly to prevent evanescent energy leakage from any air gaps between them. Plastic heat shrink tubes were attached to the ends of the sample holder with silicone to create a water-proof connection so that liquid samples could be circulated through the device without any leaks. The two fully assembled devices



(a) Device 1 (b) Device 2

Figure 2.7: Fully assembled devices with heat shrink tube connections to the sample holders.

can be seen in Fig. 2.7. Liquid solutions were passed through the sample holder by expelling liquid with a syringe into the tube from the bottom until the liquid level reached the top of the upper tube. Injecting liquid from the bottom helped to push all bubbles and air pockets out of the sample holder.

2.5.1.2 Network Analyzer and Waveguide Calibrations

A two-port Keysight E5080B-2K0 vector network analyzer (VNA) was used in all experiments. The VNA was set up to measure s-parameters from 8 to 12 GHz with 1,201 sweep points and a resolution bandwidth of 200 Hz. Prior to each measurement session, the VNA was calibrated using a 2-port Short-Open-Load-Through (SOLT) calibration to bring the VNA's calibration reference plane to the end of two cables attached to each of the VNA's ports. The cables were then attached to the waveguide adapters, which were attached to WR90 waveguides that were screwed onto one of the devices. A schematic representation of the connections between the VNA, waveguides, and a device are shown in Fig. 2.8.

A second calibration was performed to bring the reference plane to the ends of the supercoupling channel. This calibration used a standard 10-term error model, which assumes that the waveguide ports are perfectly isolated [134]. The method normally requires attaching and measuring the

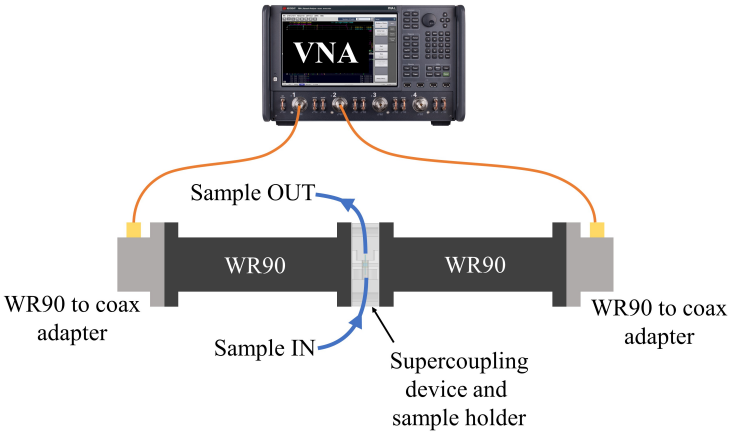


Figure 2.8: Schematic of the measurement setup. The device was connected to WR90 waveguides on both sides. The waveguides were attached to waveguide-to-coax adapters, which were used to connect the setup to the VNA via coaxial cables. Sample liquids were introduced into the device from the bottom to prevent the formation of air cavities inside the sample holder.

response of a few loads at each port, namely a short (**S**), an open (**O**), and a matched load (**M**), followed by a through (**T**) connection between the ports. An open waveguide load does not exist in practice, but an offset short (**OS**) can be used in its place. The length of the offset is typically $\lambda/4$ in order to provide a load that behaves like an open circuit and also provides independent impedance values compared to **S**. The **OS** that was available for this study had an offset of 7.6 mm, which is about one-fifth of the TE10 guided wavelength at 10 GHz ($\sim$39.76 mm). It is also a quarter-wavelength long at about 11.8 GHz. Additionally, the reflection coefficient of the matched load was estimated to be about -40 dB. The responses from each load were saved so that this second calibration could be applied in post-processing. This calibration was essential for removing reflections from the waveguide adapters, which distorted the measured s-parameters of the devices.

Table 2.2: Measured water-alcohol mixtures by alcohol volumetric percentage.

Percentage	5	10	15	25	50	75	100
Ethanol	✓	✓	✓	✓	✓	✓	✓
Methanol	×	×	×	✓	✓	✓	✓

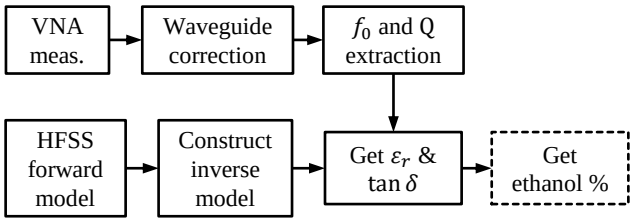


Figure 2.9: Processing flow for results.

2.5.2 Sample Preparation

Eleven mixtures were tested. Seven solutions of ethanol and distilled water were tested at 5, 10, 15, 25, 50, 75, and 100% ethanol concentration by volume. Four methanol and distilled water solutions were also tested at 25, 50, 75, and 100% methanol concentrations by volume. The tested mixtures are summarized in Table 2.2.

The ethanol and methanol solutions were prepared by measuring 100% alcohol into test tubes with 0.5 ml gradation lines to the required amount. For the 5, 10, and 15% concentrations, distilled water was also measured into larger, separate test tubes with gradation lines of 1 ml. The measured portions of distilled water and alcohol were then mixed together in a single test tube to obtain a solution at the desired concentration. The mixed solution occupied less volume than the combined volumes of water and alcohol due to molecular packing. The alcohol mixtures had the following errors: $5 \pm 0.6\%$, $10 \pm 0.3\%$, $15 \pm 0.4\%$, $25 \pm 0.9\%$, $50 \pm 0.8\%$, $75 \pm 0.9\%$. The derivation for these errors is given in Section 2.6.

2.5.3 Data Processing

The processing flow for estimating ϵ_r and $\tan\delta$ from the measured S_{21} response is illustrated in Fig. 2.9, where a measurement made by the VNA is first corrected using the waveguide calibration. Then, the center frequency f_0 and quality factor Q are extracted from the measurement. The f_0 and Q are used to read out corresponding values of ϵ_r and $\tan\delta$ from an inverse model created using full-wave simulations from ANSYS HFSS. The following sections gives details on the f_0 and Q extraction and the construction of the inverse model.

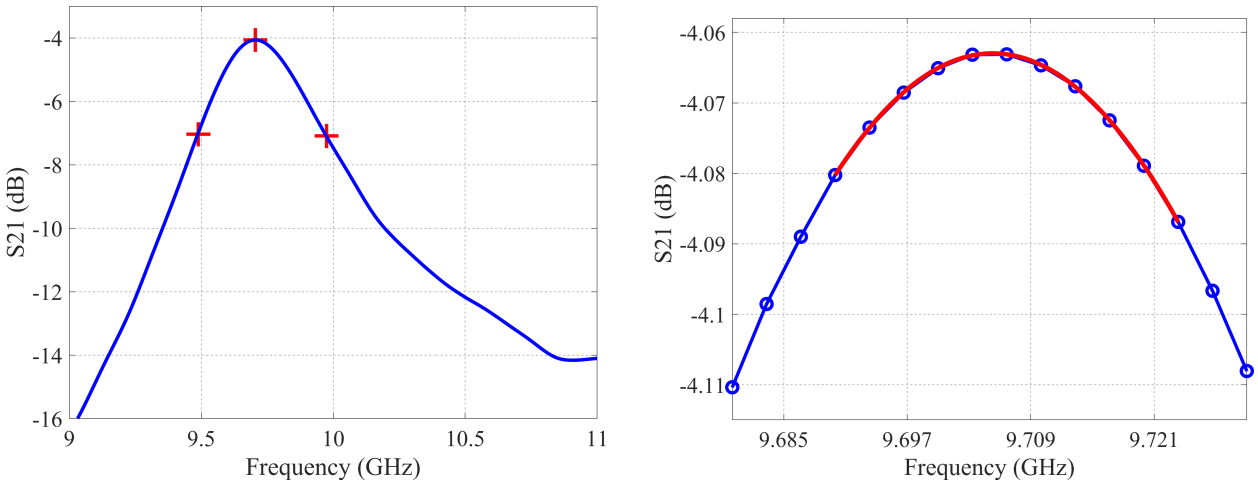
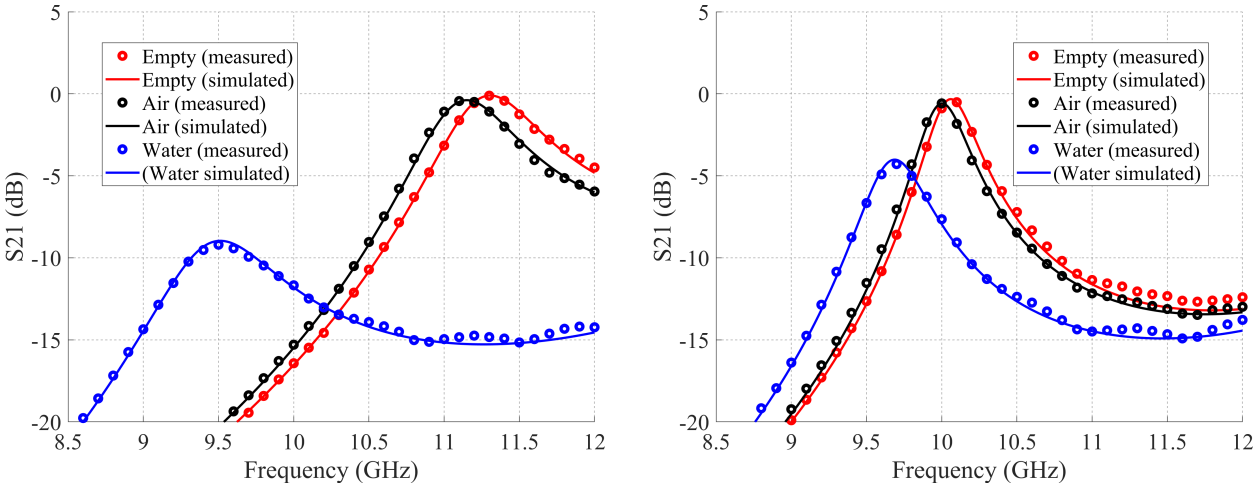


Figure 2.10: Typical S_{21} measurement for water. The center frequency f_0 and points 3 dB below the peak are shown with red cross hairs in the left panel. The right panel shows the data in blue compared with a fitted parabola in red for interpolating the location of f_0. Blue circles are sample points.

2.5.4 Extraction of f_0 and Q

The center frequency f_0 is defined as the frequency location of a peak in the S_{21} response, while the quality factor Q is f_0 divided by the double-sided 3 dB bandwidth. Figure 2.10 illustrates a typical S_{21} measurement with waveguide calibration applied. The 3 dB points and center frequency are also marked. The response is measured at discrete frequency points, and therefore the actual peak of S_{21} may lie between two points. This is also true for the 3 dB points. To avoid errors from relying on discrete samples, the center frequency is determined using the following steps: (1) the maximum sample point is located; (2) several points around this maximum are used to perform a least squares fit of a parabola to the data; and (3) the parabola coefficients are used to determine the location of the peak. The 3 dB bandwidth is measured by interpolating the crossing point between S_{21} and 3 dB below the peak's magnitude.



(a) Device 1

(b) Device 2

Figure 2.11: A comparison between the measured and simulated S_{21} after performing the forward model optimization using a constrained Nelder-Mead algorithm. Simulations are shown in solid lines and measurements are shown in dots.

2.5.5 Construction of Inverse Model

2.5.5.1 Forward Model

The manufactured devices are not perfect replicas of the devices used in simulation. There are imperfections due to machining/printing tolerances, slight part misalignment, and some uncertainty in the chamber's dielectric constant. To correct for these errors, a forward model is developed by perturbing the sample holder, channel dimensions, and metal conductivity until the simulation results match those obtained from an experimental measurement of three known dielectric materials. The bounds of the perturbations are set based on the tolerances given by the manufacturers. The three cases of known dielectric constant that are used to calibrate the forward model are: (1) a measurement of the device with no chamber inside; (2) a measurement with the chamber inside while filled with air; and (3) a measurement when the chamber inside is filled with distilled water. Simulations of the three cases are used to define a cost function that is minimized using a six parameter constrained Nelder-Mead simplex in MATLAB [69]. The six parameters over which the optimization is performed are: (1) the radius of the sample holder chamber; (2) the height of

the sample holder chamber; (3) the depth of the pocket machined into the channel that houses the sample holder; (4) the width of the channel; (5) the height of the channel and (6) the conductivity of the metal. The cost function is defined as a sum of relative errors for the resonant frequency (f_0), quality factor (Q), and insertion loss ($S_{21}(f_0)$) (see Eq. 2.3). A comparison between the measured response and the optimized simulation response for these three materials is shown in Fig. 2.11 for both devices.

$$F_{cost} = \frac{|Q^{meas} - Q^{sim}|}{Q^{sim}} + \frac{|f_0^{meas} - f_0^{sim}|}{f_0^{sim}} + \frac{|S_{21}(f_0^{meas}) - S_{21}(f_0^{sim})|}{S_{21}(f_0^{sim})} \tag{2.3}$$

Note here that $S_{21}(f_0^{meas})$ is the insertion loss at the resonant frequency. This is a single scalar number which is independent of the quality factor since it depends only on the resonator loss and does not depend on the stored energy in the resonator. Therefore, Q, f_0 and $S_{21}(f_0)$ are three independent quantities which are used in this cost function.

2.5.5.2 Inverse Model

Once the forward model is optimized, full-wave simulations in HFSS are used to sweep a range of values for the sample liquid's ϵ_r and $\tan\delta$. This gives a function that takes ϵ_r and $\tan\delta$ and produces f_0 and Q. As expected, due to supercoupling, the dielectric constant ϵ_r is a strong function of f_0, while $\tan\delta$ is mainly a function of Q. The forward (f_f) and inverse (f_i) models are specified below.

$$f_f : \mathbb{R}^2 \to \mathbb{R}^2$$

$$f_f(\epsilon_r, \tan\delta) = f_0, Q \tag{2.4}$$

$$f_i := f_f^{-1} = (f_i^{\epsilon}, f_i^{\delta}) \tag{2.5}$$

$$\epsilon_r = f_i^{\epsilon}(f_0, Q) \tag{2.6}$$

$$\tan\delta = f_i^{\delta}(f_0, Q). \tag{2.7}$$

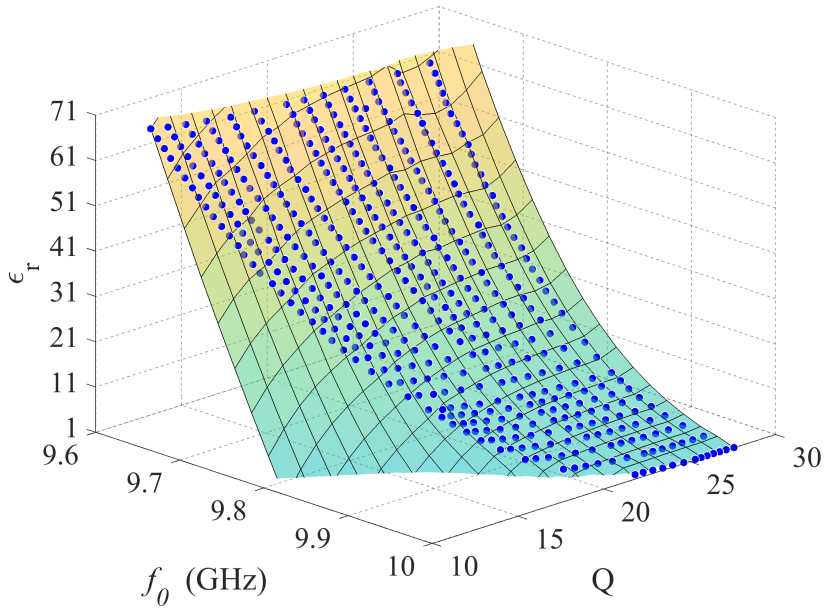


Figure 2.12: The inversion surface of ϵ_r for Device 2 generated by interpolating the sweep points (blue dots) that are obtained from HFSS transmission simulations. A bi-harmonic spline interpolation is used to generate the surface from the sample points.

To generate the inverse function, the forward model's sweep points are interpolated with a bi-harmonic spline interpolation. This generates a $\mathcal{C}^2$-diffeomorphism (f_f) that can be inverted at each point. Each component of the inverse function (i.e. f_i^ϵ and f_i^δ) can be visualized as a surface. Figure 2.12 shows the surface for the f_i^ϵ component.

2.6 Error Analysis

There are six sources of error in the proposed methodology. First, there is some error in the known concentrations of the alcohol and water mixtures because of measurement precision limitations. A second error comes from non-ideal loads used for the waveguide calibration. Third, there are repeatability errors with the waveguide calibration and liquid measurements. A fourth source of error comes from how well the inverse model function (2.5) matches the forward model (2.4). A fifth source of error comes from the accuracy of the forward model. And finally, a sixth source of error stems from electronic noise in the VNA. Methods for providing quantitative estimates of these errors are given in the following sections except the errors due to non-ideal calibration loads

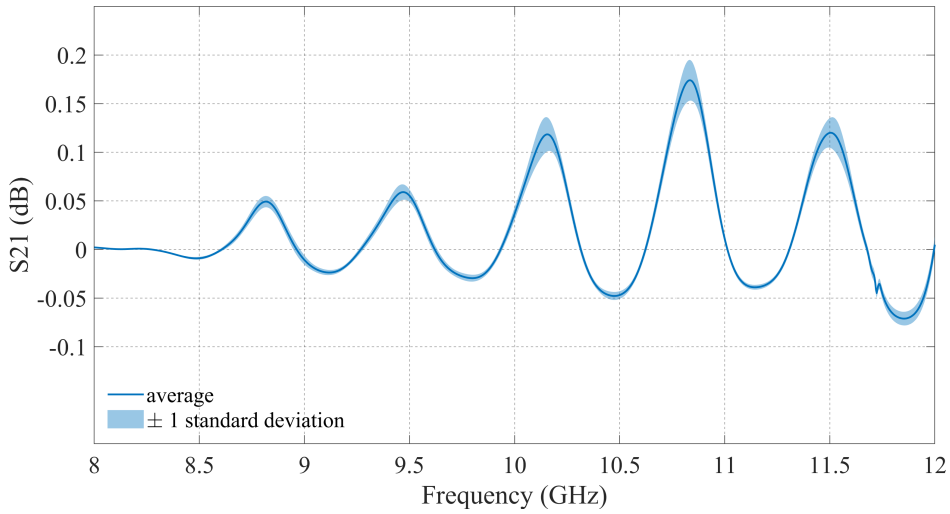


Figure 2.13: Average calibrated through response. One standard deviation is shown by the shaded areas.

and an imperfect forward model, which involve considerations beyond the scope of this work.

2.6.0.1 Volume Measurement Error

As mentioned in Section 2.5, the alcohol solutions were prepared using two sizes of test tubes, a larger size with 1 ml gradation lines, and a smaller size with 0.5 ml lines. It was estimated that the volumetric error in using the large test tube was ± 0.5 ml, and the error from the small one was within ± 0.1 ml. In preparing the 5% solution, 2.5 ± 0.1 ml of ethanol was mixed with $(45 \pm 0.5) + (2.5 \pm 0.1)$ ml of distilled water, which indicates 45 ml from the large tube and 2.5 from the small tube. In the worst case scenario, 2.6 ml of alcohol might be mixed with 46.9 ml (44.5 + 2.4) of water to give a 5.54% mixture. Thus, this mixture yielded a solution of $5 \pm 0.6\%$ at the worst. For the 10% solution, 5 ± 0.1 ml of ethanol was mixed with 45 ± 0.5 ml of water, giving a $10 \pm 0.3\%$ solution. For 15%, 7.5 ± 0.1 ml of ethanol was mixed with $(40 \pm 0.5) + (2.5 \pm 0.1)$ ml of water, giving a $15 \pm 0.4\%$ mixture. For 25%, 3 ± 0.1 ml of ethanol was mixed with 9 ± 0.1 ml water, giving $25 \pm 0.9\%$. For 50%, 7 ± 0.1 ml of ethanol was mixed with 7 ± 0.1 ml of water, giving $50 \pm 0.8\%$. For 75%, 9 ± 0.1 ml of ethanol was mixed with 3 ± 0.1 ml of water, giving $75 \pm 0.9\%$. The procedure for mixing the 25%, 50%, and 75% ethanol mixtures was also applied

to the methanol mixtures. Once the samples were prepared, the same sample was measured in both devices to maintain consistency in the experiment. The errors in the mixture percentages only affects the absolute estimate of the percentage from the measured dielectric constant and is not a shortcoming of the measurement system.

2.6.0.2 Waveguide Calibration Errors

There are two sources of error associated with the waveguide calibration: imperfect calibration loads and repeatability variations between calibrations. The latter error, for example, may be due to minute changes in cable flexion and interconnects. Errors from non-ideal loads will be omitted from this analysis, although the matched load (**M**) may have introduced the most error in this work. Variations between calibrations were assessed by observing the corrected S_{21} response while the waveguides were directly connected together (i.e. the through response). Eight waveguide calibrations were performed in the course of this study. Data from these calibrations was used to calculate an average corrected through response along with a standard deviation. Both are shown in Fig. 2.13. The following approach was used to quantify the calibration variation's effect on the extracted f_0 and Q and the subsequent ϵ_r and $\tan\delta$ of a liquid. First, an "ideal" S_{21} response for each material was created by using the material's estimated dielectric values ($\hat{\epsilon}_r$, $\tan\hat{\delta}$) to select one HFSS simulation from the forward model sweep with the closest (ϵ_r, $\tan\delta$) pair. Then, the S_{21} response from that simulation is perturbed by adding the average calibration through response to it, or

$$\tilde{S}_{21} = S_{21} + (S_{21}^T - 1), \tag{2.8}$$

where S_{21} is the device's ideal response, S_{21}^T is the average calibration through response, and $\tilde{S}_{21}$ is the perturbed response. All quantities in (2.8) are in linear units. From there, measurements of $\tilde{f}_0$ and $\tilde{Q}$ are extracted from $\tilde{S}_{21}$. Because of the calibration's perturbation, the perturbed measurements ($\tilde{f}_0$, $\tilde{Q}$) differ from the nominal values (f_0, Q) that would have been obtained from the ideal S_{21}. Those differences, (Δf, ΔQ), are then taken as the maximum error. For example, if the ideal f_0 is measured at 9.7 GHz, but the perturbed f_0 is 9.71 GHz, then the error on the f_0 measurement

would be ± 10 MHz. The errors (Δf, ΔQ) can be translated into errors in ($\Delta \epsilon_r$, $\Delta \tan\delta$) by using the inverse function described in Section 2.5. This is done by evaluating the inverse function at eight points corresponding to every combination of $f_0 \pm \Delta f$ and $Q \pm \Delta Q$. The greatest difference in ϵ_r and $\tan\delta$ is then computed from those sample points, and half of that difference is taken as the maximum error. For example, if the maximum and minimum ϵ_r values were 37 and 32, with a nominal value of 34.5, and the corresponding sample points were ($f_0 + \Delta f$, $Q + \Delta Q$) and ($f_0 - \Delta f$, $Q - \Delta Q$) respectively, then the maximum error for this material's ϵ_r would then be ± 2.5. It is in this way that the maximum error due to an imperfect calibration is estimated for each material. The error from calibration is by far the most dominant error component.

2.6.0.3 Inverse Model Error

The forward model consists of the device's geometry defined in HFSS and the electromagnetic solver that HFSS uses to calculate s-parameters. The accuracy of the forward model is affected by simulation parameters such as the density of the finite element (FE) mesh. These parameters were specified to give a high-fidelity, accurate simulation of a device's response.

There is a fitting error in the inverse function f_i that is used to produce estimates of ϵ_r and $\tan\delta$. This error comes from the fact that the inversion surface (see Fig. 2.12) is an approximate fit to the sample points produced by the forward model. Thus, if one of the forward model's sample points was the input/output pair ($\epsilon_r = 30$, $\tan\delta = 0.4$) and ($f_0 = 9.5$ GHz, $Q = 20$), then plugging the output pair into the inverse model, will not exactly produce (30, 0.4), but instead something like (30.4, 0.41). This difference between the forward and inverse models is quantified by computing the root mean square error (RMSE) between all sweep points of (ϵ_r, $\tan\delta$) from the forward model and the corresponding estimates of ($\hat{\epsilon}_r$, $\tan\hat{\delta}$) from the inverse model.

2.6.0.4 VNA Noise and Total Error

The displayed average noise level (DANL) of the VNA is specified at -145 dBm/Hz between 8 and 12 GHz. An intermediate frequency (IF) bandwidth of 200 Hz was used in the measurements of

this work, which results in a DANL of -122 dB. Since the DANL is very low compared to the S_{21} response of every liquid, which was always above -20 dB, the effect of noise from the VNA on the measurement of f_0 and Q is omitted.

The total error due to calibration, fitting, and noise is calculated by taking the Euclidean distance of each error for each liquid, or

$$\epsilon_{err} = \sqrt{\epsilon_{cal}^2 + \epsilon_{fit}^2}. \tag{2.9}$$

The estimated dielectric constants of each liquid are then stated to be within $\pm\epsilon_{err}$. The same is done for $\tan\delta$. These errors for the different liquids are shown in Table 2.3. From Fig. 2.13, it is clear that the calibration error is a function of frequency and hence is not consistent over the different liquids. Finally, it is important to note that these are the upper and lower bounds on the error and hence are very conservative estimates.

2.7 Experimental Results

The dielectric constant of the liquid mixtures listed in Table 2.2 were measured over the course of two measurement sessions. Two other experiments were also carried out to demonstrate the ability of the device to track real-time changes in ϵ_r, as well as the ability to track changes in the concentration of the ethanol and water mixtures. Here, "real-time" is defined by the sweep time of the VNA, which was around 2 seconds during these measurements. Any changes in dielectric constant on time scales shorter than this sweep time are not captured by the VNA. In the applications targeted by this study, the time scales are much larger than 2 seconds and hence this method can be approximated to be *quasi* real-time. The system can be made truly real-time by replacing the VNA with a chirp based vector transmission measurement where the chirp duration can be on the order of microseconds [4]. In this case, dielectric characterization can be performed on timescales on the order of microseconds.

Table 2.3: Device 1 (left) and Device 2 (right) spot measurements. Distilled water, ethanol, and methanol are indicated by W, E, and M respectively. The center frequency f_0 is given in GHz.

Liquid	ϵ_r	$\pm\Delta\epsilon_r$	$\tan\delta$	$\pm\Delta\tan\delta$	f_0	Q
W	62.09	0.19	0.51	0.24	9.50	10.37
5% E	52.55	0.69	0.59	0.28	9.58	9.44
10% E	49.33	1.35	0.67	0.29	9.60	8.68
15% E	40.97	1.2	0.76	0.13	9.68	7.87
25% E	29.54	0.25	0.91	0.19	9.82	6.57
50% E	16.22	1.25	1.12	0.15	10.01	NA
75% E	8.13	0.03	0.96	0.09	10.51	NA
100% E	4.92	0.09	0.44	0.04	10.75	10.07
25% M	36.10	0.95	0.85	0.25	9.73	7.17
50% M	22.30	0.84	1.08	0.19	9.94	NA
75% M	13.70	0.14	1.1	0.15	10.2	NA
100% M	8.12	0.06	0.90	0.16	10.51	NA

Liquid	ϵ_r	$\pm\Delta\epsilon_r$	$\tan\delta$	$\pm\Delta\tan\delta$	f_0	Q
W	61.57	0.27	0.52	0.01	9.69	20.48
5% E	54.26	.010	0.60	0.02	9.71	19.96
10% E	49.75	0.12	0.67	0.02	9.72	19.57
15% E	40.77	0.21	0.77	0.03	9.74	19.30
25% E	29.53	0.05	0.92	0.05	9.77	19.11
50% E	16.17	0.05	1.05	0.07	9.82	19.75
75% E	8.72	0.02	0.93	0.02	9.88	21.11
100% E	5.10	0.01	0.46	0.00	9.93	24.58
25% M	35.91	0.17	0.84	0.05	9.75	19.13
50% M	21.90	0.13	1.01	0.08	9.80	19.35
75% M	13.94	0.06	1.02	0.05	9.84	20.10
100% M	8.78	0.05	0.86	0.02	9.88	21.45

2.7.1 Spot Measurements

The estimated ϵ_r and $\tan\delta$ for the measured solutions are shown in Table 2.3. The ethanol solutions are abbreviated with E, while methanol and distilled water are abbreviated with M and W, respectively. The dielectric constant and loss tangent of distilled water that were used in the forward model are $\epsilon_r = 62.0883$ and $\tan\delta = 0.5152$ at 9.51 GHz for Device 1 and $\epsilon_r = 61.5693$ and $\tan\delta = 0.5245$ at 9.69 GHz for Device 2 [85]. As expected, the inverse model results shown in Table 2.3 agree with the forward model for the case of water.

Device 1 has higher insertion loss due to the larger sample holder volume, which makes it more susceptible to calibration error. Further, note from Fig. 2.13 that the calibration error is much higher in the 10 - 12 GHz range, which is the range where Device 1 operates. Therefore, the results from Device 1 are less accurate than those from Device 2. This is the main reason for the slight discrepancy between the results from the two devices, the other reason being that the supercoupling frequencies are slightly different for the two devices. It is interesting to note that the loss factor of the ethyl and methyl solutions reaches a maximum around 50-75% before decreasing again. These results are in very good agreement with those published in the literature (see for example [11, 7]). For the cases where there is no upper side-band 3 dB frequency, the quality factor is undefined and

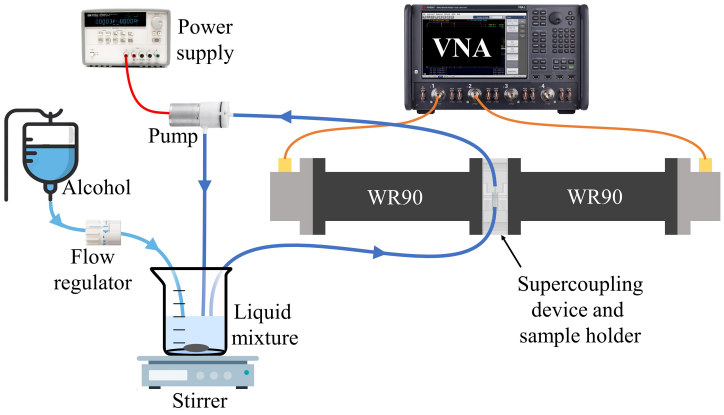
marked as NA in Table 2.3. The loss tangent of these cases is estimated from the lower side-band 3 dB frequency (i.e. repeating the processing flow from Fig. 2.9 using only the lower side-band 3 dB frequency).

2.7.2 Real Time Measurements

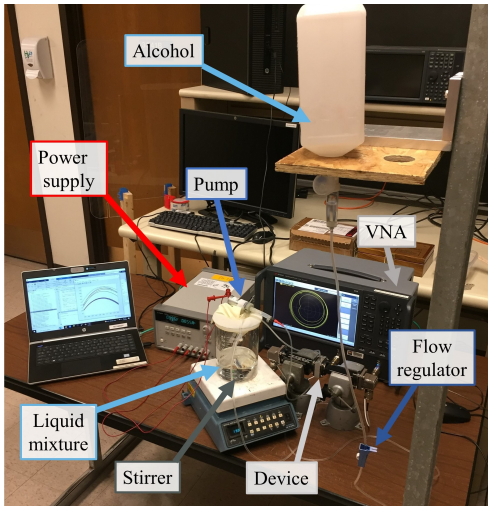
Two experiments were also conducted to demonstrate the ability of the device to monitor changes in a liquid's dielectric constant as a function of time. The schematic and picture of the setup for these experiments are shown in Figs. 2.14a and 2.14b, respectively. The liquid mixture was held in a large beaker on top of an automatic stirrer. A liquid pump was used to circulate the liquid mixture through plastic tubes into the supercoupling device and back into the liquid mixture. Device 2 was used for all the real-time measurements since it had greater immunity to waveguide calibration errors. The VNA was also set up to automatically measure the scattering parameters once every minute. The chemical composition of the liquid mixture was varied over time by adding additional liquid from a bottle, usually filled with alcohol, which was held above the large beaker. A flow regulator was also used to maintain a constant flow rate from the raised container into the liquid mixture.

For the first experiment, a liquid mixture made of 50 g of sugar and 500 ml of distilled water was placed in the large beaker. The raised bottle was filled with 400 ml of distilled water and 100 ml of ethanol to make a solution of 20% ethanol. The mixture composition was chosen to mimic the fermentation process of alcoholic beverages as the liquid in the beaker would start as a sugar-water mixture and end as a mixture of sugar, water, and 10% alcohol (by volume). It should be noted that the stirrer was not used in this experiment because the flow rate was set very low to allow time for the liquids to mix via diffusion.

Figure 2.15a shows the evolution of the mixture's dielectric constant as a function of time. The final alcohol concentration at the end of the experiment was expected to be around 10% by liquid volume. The alcohol concentration could not be estimated from the measured dielectric constant in this case because of the additional effect that the sugar had on the dielectric constant. However,



(a) Schematic of the real-time experimental setup.

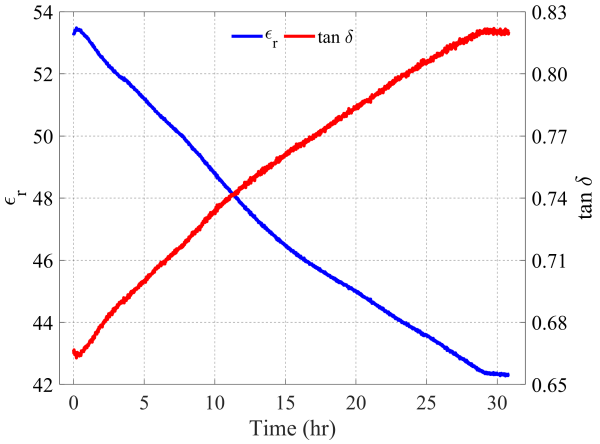


(b) Picture of real-time measurement setup.

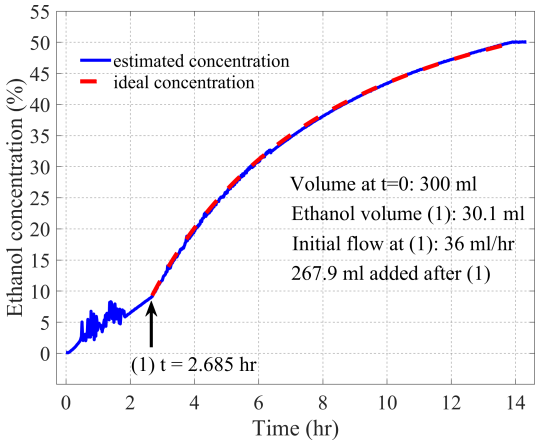
Figure 2.14: Experimental setup design and implementation for the real-time measurements.

it can be seen that small changes in ϵ_r and $\tan\delta$ were easily picked up by the measurement system. The variation in the measured value was typically less than 0.08 for ϵ_r and 0.004 for $\tan\delta$.

The second experiment was conducted to see if alcohol concentration could be estimated from the measured ϵ_r. The same experimental procedure as the last one was used, except that 300 ml of distilled water was poured into the large, bottom beaker, while the top container was filled with 309 ml of 100% ethanol so that a final concentration of about 50% would be achieved (about 9-10 ml of alcohol would remain in the top container and tubing when the dripping stopped). The flow rate was also initially set at roughly 12 ml/hr. It should be noted that the flow regulator was designed for saline solutions, and therefore it did not properly regulate the flow of the ethanol, which is more viscous than water. This led to some variation in the flow rate over time. The stirrer was used in this experiment to actively mix the two liquids throughout the measurement process. This was necessary because the alcohol would enter the beaker in streams that took time to dissolve. Additionally, without active mixing, the added alcohol would rise to the top of the liquid mixture and create a stratification between alcohol and water. The stirrer alleviated these behaviors, but streams of alcohol still entered the intake tube on occasion. These streams would



(a) Evolution of ϵ_r and $\tan\delta$ over time as a mixture of 20% ethanol is added to a mixture of sugar and water.



(b) Estimated concentration of ethanol over time as ∼300 ml of ethanol is added to distilled water. Concentration estimate is based on measured ϵ_r from table 2.3.

Figure 2.15: Experimental results showing in-line measurements of the permittivity of two solutions whose compositions changed over time.

cause the measured alcohol concentration to sporadically spike up. These effects diminished, though, as the volume of liquid in the beaker grew. Most of these spikes occurred in the first two hours of the experiment.

To estimate the concentration of alcohol from the measured transmission parameters, first the inverse model is used to find the dielectric constant and loss tangent from the measured scattering parameters as a function of time. Then, spot measurements in Table 2.3 are used to derive the relationship between alcohol concentration and ϵ_r for Device 2. A polynomial curve of ϵ_r versus percent concentration was fitted to the spot measurement points to make a simple model for estimating percent concentration from ϵ_r. This gives the percentage concentration of alcohol as a function of time, which is shown in Fig. 2.15b.

As mentioned earlier, major spikes in concentration subsided after the 2 hour mark. There were still some small spikes due to the streams that do not disappear until after the 6 hour mark. Once the initial large spikes subsided, the flow rate was increased to 30 ml/hr at about the 3 hour mark, indicated by (1) in Fig. 2.15b, and left as is until the alcohol bottle was empty. The flow rate was observed one more time and was found to be about 25 ml/hr at the 3.75 hour mark. Once again, it

appeared that the ethanol flow was not properly controlled by the flow regulator. Given that fluid flow through a long narrow tube of constant diameter is laminar and dominated by viscous forces, the flow rate drops exponentially following the Hagen-Poiseuille law [165]. The parameters of the exponential flow rate were obtained heuristically from observations of the flow rate over time and the resulting ideal alcohol concentration level is shown in the dashed red line in Fig. 2.15b. Since the measured concentration tracks the ideal (predicted) concentration very well, it can be concluded that accurate real-time tracking can be achieved with the proposed device.

These experiments provide quantitative verification that the proposed device is able to track changes in the dielectric constant and loss tangent of an evolving liquid. By replacing the VNA with a miniaturized circuit that can extract the resonance characteristics of a resonator [4], this device may become a compact, sensitive complex dielectric constant measurement tool that can be used for real-time monitoring of liquids in many industrial and scientific applications.

2.8 Conclusion

A device that can accurately measure the real-time complex dielectric constant of a wide range of liquids at X-band is presented. The device is based on the concept of energy squeezing or supercoupling through narrow rectangular waveguide channels. It exploits the strong fields generated inside the channel to enhance the wave-matter interactions between the electric field and the liquid under test. Three interpretations of supercoupling are discussed and used to motivate the design choices made for the device. To improve the measurement sensitivity, a large pocket is machined inside the channel that houses a sample holder. This approach is one of the novelties of this device and relies on a high precision micro-3D printed sample holder. The sample holder is carefully designed to prevent the formation of air bubbles and also to eliminate energy leakage through the feeding tubes.

Two versions of the device are fabricated: one for higher sensitivity, and another for higher accuracy. To account for fabrication tolerances, a forward model based on full wave simulations

is generated and optimized using a constrained Nelder-Mead algorithm. Using this optimized forward model, an inverse model is generated to find the complex dielectric constant from the measured scattering parameters of the device with the liquid running through the sample holder. An exhaustive error analysis is conducted to identify and minimize the different sources of error in the measurements. The largest error was found to be due to the imperfect waveguide calibration. This error could be addressed by using better calibration standards, a sliding load, or an alternate calibration procedure such as the Thru-Reflect-Line (TRL) calibration, which does not depend on a matched load [39].

Two sets of experiments were performed: one of spot measurements of alcohol-water mixtures, and another of real-time measurements of evolving alcohol-water-sugar mixtures. The results of the spot measurements are in very good agreement between the two devices and also with the published literature. The real-time experiments demonstrate the ability of the device to accurately track both rapid and slowly varying changes in the complex dielectric constant of a liquid mixture. Therefore, it provides a compact non-invasive solution to monitoring evolving liquid mixtures with a high degree of accuracy.

CHAPTER 3

EM Simulation Development and Characteristics

This chapter provides additional detail on the development and characteristics of a full-wave scattering model for corn fields, and is meant to supplement the material in Chapter 4. It elaborates on the simulation methodology for predicting radar backscatter from corn fields, which involves using a commercial, numerical electromagnetic solver to calculate the electromagnetic fields from 3D Computer-Aided Design (CAD) models of corn plants. It also describes the major structural elements of corn and how the differing plant components are electrically modeled. This chapter also validates modeling approaches with analytic or simulated results.

Corn is known by that name in the US, but it is also referred to as maize internationally. It is a robust, tall grass that produces cereal grain. Early corn plants were domesticated from wild teosinte plants by Indigenous peoples in southern Mexican about 9,000 years ago. Today's commercial varieties produce grain or kernels that are typically yellow or white, but there are many different varieties that can take on a range of colors [155].

This chapter is organized as follows. Section 3.1 discusses high-level considerations for a simulation methodology to calculate the radar backscatter from corn fields. Section 3.2 explains the electrical and geometric properties of corn plants that must be considered. Section 3.3 provides similar details for electrically and geometrically modeling a rough soil surface. Section 3.4 provides some simulation results to validate a choice made in developing the simulation methodology. And finally, Section 3.5 provides some simple analyses of how the radar backscatter from a corn field might change as a function of the incidence angle.

3.1 Simulation Methodology

Achieving a high-fidelity scattering model was the main goal for pursuing a full-wave methodology for calculating the radar backscatter from corn fields. Part of this goal, then, was to accurately represent the geometry of a corn plant. Often, a plant's shape is complex and describing it as a random collection of cylinders and flat disks falls short of reality. Such simple shapes are typically used in scattering models, though, because they can be analyzed with Maxwell's equations to provide scattering solutions. More complex shapes can generally only be electromagnetically analyzed with a numerical solver.

Such solvers are based on one of three general methods: the Finite-Difference Time-domain (FDTD) method, the Method of Moments (MoM), and the Finite Element Method (FEM). Very briefly, FDTD works by dividing the geometry into cubes or voxels, and then it simulates how electromagnetic fields disperse through the voxels at discrete time steps. It can easily provide broadband solutions since it operates in the time-domain, but the representation of the geometry is limited by the voxel size. On the other hand, MoM is a frequency-domain method that works by meshing the surface of an object with triangles and then calculating how the currents on the object's surface interact with each other and other surfaces. These interactions are captured in a "stiffness" matrix that is dense (every entry is filled). It typically does very well with conductive surfaces, and so is well suited for analyzing antennas. Finally, FEM is similar to MoM in that it operates in the frequency domain and needs a mesh of the object. It differs in that it meshes the whole volume of the object, the stiffness matrix is sparsely filled, and it typically does better with dielectric objects.

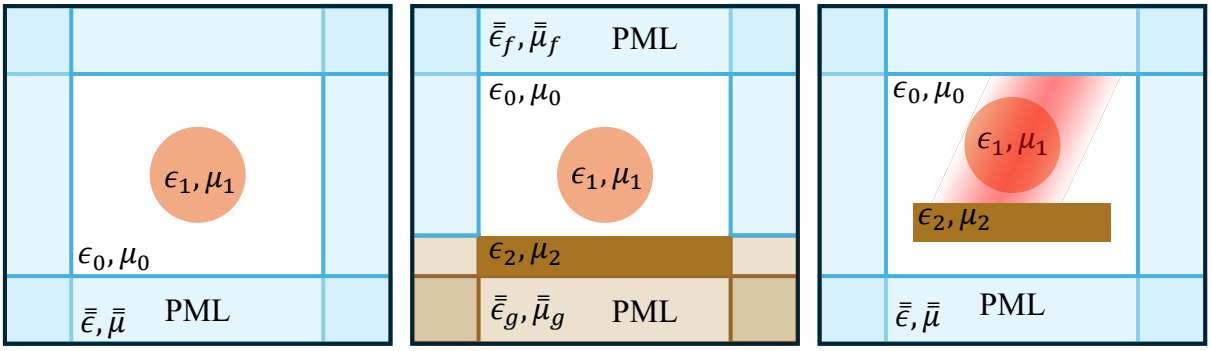
We chose to use a solver based on FEM because it could represent the plant's geometry more accurately than FDTD, and plants are primarily made from dielectric material. We also wanted to use a commercial solver since a custom solver could be time consuming to develop from scratch. The mathematical machinery behind FEM does require expertise to understand, but it is somewhat straightforward to implement. Computationally meshing 3D geometric objects is perhaps the more challenging task. It is also very beneficial to have some kind of user interface for interacting with

CAD objects, and that interface is also non-trivial to develop. Given these constraints, we decided to use ANSYS HFSS as the numerical solver. With that choice, there are several questions we had to answer. For instance, how could a CAD model of a corn plant be made? What would the electrical properties of the plant be? How would the shape and electrical properties of the soil be modeled? And finally, how should a simulation in HFSS be set up so that the backscatter from a corn field can be predicted, especially given the constraints of HFSS? The first few questions will be answered in later sections, and the last question will be addressed next.

3.1.1 Potential Simulation Configurations

It is a common task in HFSS to calculate the backscatter from an object in free space. This involves defining a region of free space in which the object is placed. That free space region is then surrounded by a layer of fictitious material called a Perfectly Matched Layer (PML). The permittivity and permeability tensors of the PML are specially designed so that any waves scattered by the object produce no reflections when they hit the PML, and are completely absorbed by it, thereby mimicking an infinitely-large simulation domain. This kind of set up is illustrated by Fig. 3.1a. Given this option, one way to go about getting a corn plant's backscatter might be to calculate the backscatter from one plant in free space. This can easily be done in HFSS, but it only provides the backscatter of one plant in isolation without considering interactions between other plants or the ground.

Another option in HFSS is to introduce a ground plane by putting the plant on top of a dielectric to represent the soil, and then two different PMLs can be applied to the soil and the empty space around the plant as shown in Fig. 3.1b. There are a couple of concerns with this approach, though. First, the PMLs are designed with respect to the permittivity of the material that they are meant to provide a reflectionless boundary for. This means that there will be a discontinuity in the PML's material properties where the PML for the air and the PML for the soil meet. This may result in artifacts. One could also just expand the computational domain so that a buffer of air surrounds the plant and box of soil. This can still be problematic, though. For one, the box needs to be big enough



(a) Object in free space.

(b) Object in free space over a ground plane.

(c) Object and ground plane in free space illuminated by a Gaussian beam.

Figure 3.1: Diagrams of HFSS simulation layouts for different scenarios.

so that the plant can be fully illuminated by its image in the ground plane. Second, energy that transmits into the soil will be reflected at the other side, and this will result in extra scattering that is not present in reality. Finally, the edges of the soil box would also produce additional scattering effects from diffraction.

That last issue could be mitigated with another approach, though. Up until now, it has been assumed that the excitation for the computational domain is a plane wave. HFSS has another source that makes sense: a Gaussian beam. The Gaussian beam would be more amenable since its illumination tapers off towards the edges. Thus, one could use that with the soil box as seen in Fig. 3.1c. However, this would just give the backscatter from one plant on a ground plane. How would other plants be simulated? Additional plants could be introduced in rows until there is a small patch of plants built up. But there would need to be enough of them such that the Gaussian beam sees a uniform medium of plants and soil and not the edges of the field. This means that there would need to be many plants in the simulation, which translates to an impractically large simulation. Figure 3.2 show's an example of such a simulation, where the Gaussian beam is illustrated with a transparent green cylinder, the solution frequency is at 1.25 GHz, and the computational domain's size is $4.6 \times 3.2 \times 2.9$ m, or $19 \times 13 \times 12$ wavelengths. It required 115 GB of RAM and 20 hours and 40 minutes of computer time to complete one adaptive pass in HFSS, which is not quite enough

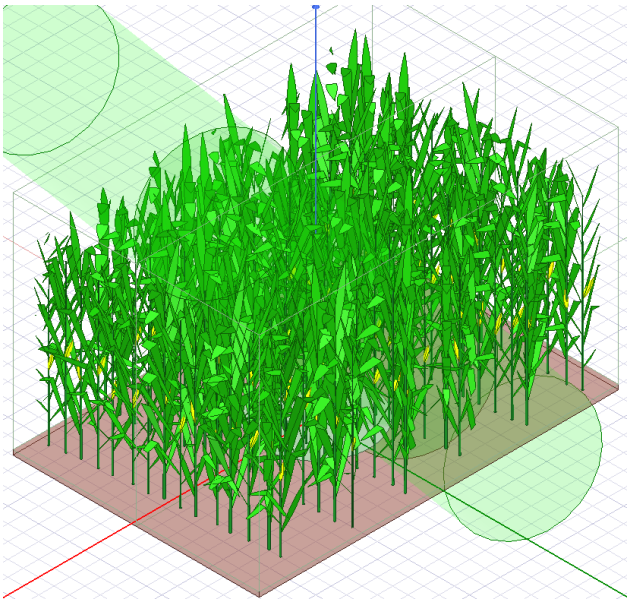
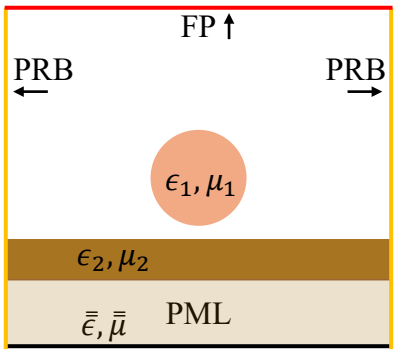


Figure 3.2: A 3D view of an HFSS simulation using a Gaussian beam illumination.

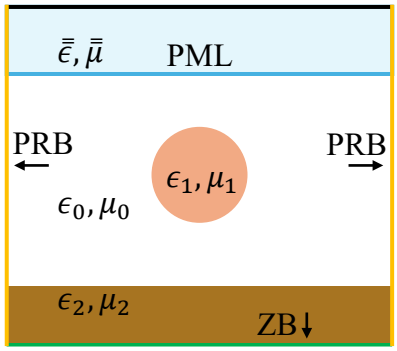
to achieve a good mesh, and this was all for just one incidence angle and polarization. That is impractical. Thus, is there a more computationally efficient way to do this?

There may indeed be a more efficient way to do this simulation within the constraints of HFSS, and that is by using periodic boundary conditions. This type of boundary essentially requires that the fields need to be equal at a pair of points on two periodic faces of a unit cell, except for a phase factor that depends on the frequency and scan direction. This works well with corn fields since there is already an aspect of periodicity in the field: corn field rows are typically spaced 76 cm apart, and there can typically be 5-6 plants per meter along a row. Thus, applying periodic boundaries makes the simulation act as if the backscatter is being calculated from an infinitely big field. This is a step in the right direction, but there are some issues to resolve about the excitation for the simulation, since a Gaussian beam will not work in a periodic context. The available excitations are plane waves, and an excitation called a Floquet port. The configuration for the boundaries of these two excitations are shown in Fig. 3.3, where the periodic boundaries and Floquet port are indicated with PRB and FP respectively. The plane wave excitation also requires an impedance boundary, which is indicated by ZB.

A Floquet port excites a periodic unit cell with different modes that are essentially periodic,



(a) Object in a periodic unit-cell with a Floquet port excitation.



(b) Object in a periodic unit-cell with a plane wave excitation.

Figure 3.3: Diagrams of HFSS simulation layouts with periodic boundaries.

free space plane waves whose wave vectors are defined by the unit cell's size and the frequency of operation. This type of excitation is frequently used to analyze periodic structures in HFSS. This was appropriate for our application, and thus we started by using this type of port. It will be seen later, though, that the plane wave excitation was used for the final simulation method. First, there are some important ramifications for the results of the simulation if periodic boundaries are used.

Perhaps the most important consequence arises from the fact that scattering from a periodic surface only occurs at discrete angles, rather than a continuum that one might expect from a rough surface, for example. The transverse wavenumbers of the allowed scattering angles are given by the following equations for a rectangular periodic lattice:

$$k_{xm} = k_{0x} + \frac{2\pi m}{a} \tag{3.1a}$$

$$k_{yn} = k_{0y} + \frac{2\pi n}{b}, \tag{3.1b}$$

where k_{0x} and k_{0y} are the Cartesian free space transverse wavenumbers of an incident wave, a and b are the unit cell dimensions along the x- and y-axis respectively, and m and n are integers. The transverse wavenumbers are taken from $\vec{k} = \hat{x}k_0\cos(\phi_s)\sin(\theta_s) + \hat{y}k_0\sin(\phi_s)\sin(\theta_s) + \hat{z}k_0\cos(\theta_s)$, where k_0 is the free space wavenumber, and ϕ_s and θ_s are the azimuthal and elevation scan angles of the incident plane wave using spherical coordinates. Equation (3.1) is a result of the periodic

boundary requirement. Then, because the scattering from a periodic surface is a discrete spectrum of plane waves, this means that there are only a finite number of incidence angles where one of the reflected plane waves will be in the backscatter direction. Those angles are given by the following formulae

$$\theta_i = \arcsin\left(\frac{\lambda}{2}\sqrt{\left(\frac{m}{a}\right)^2 + \left(\frac{n}{b}\right)^2}\right) \tag{3.2}$$

$$\phi_i = \arctan\left(\frac{na}{mb}\right), \tag{3.3}$$

where λ is the wavelength, and the angles are referred to as Bragg angles.

This observation allows us to better consider how big the unit cell should be. Ideally, we would like to determine the radar backscatter from corn at any arbitrary angle. Perhaps the smallest possible unit cell size would be 76×17 cm because of the row and inter-plant spacing. At 1.25 GHz, this would result in a relatively small number of angles. If, instead, a spacing of approximately 2° between Bragg angles was desired, then that would require a larger unit cell size. That angular resolution is achieved with a unit cell that is 152×136 cm in size, which corresponds to two corn rows with about 8 plants per row. The locations of the Bragg angles for those two lattice sizes (at least in the first octant of a unit sphere) can be seen in Fig. 3.4, where red points are the Bragg modes for the 76×17 cm lattice, and yellow points are for 152×136 cm lattice. The unit cell size could be increased to achieve a finer angular resolution if desired. This, of course, has to be balanced with computational cost. It seems that the 152×136 cm size is a good compromise between angular resolution and computational cost.

Having a larger unit size is where problems with the Floquet port excitation begin to crop up. In HFSS, these ports can only handle 100 Floquet modes, including TE and TM modes. This means that only a unit cell size of about 76 x 51 cm can be achieved because of the mode limitation. The only way around this is to use a plane wave excitation. Using Floquet ports would be preferred because one Floquet simulation calculates the response from both polarizations and many incidence angles. With the plane wave excitation, however, a simulation must be run for

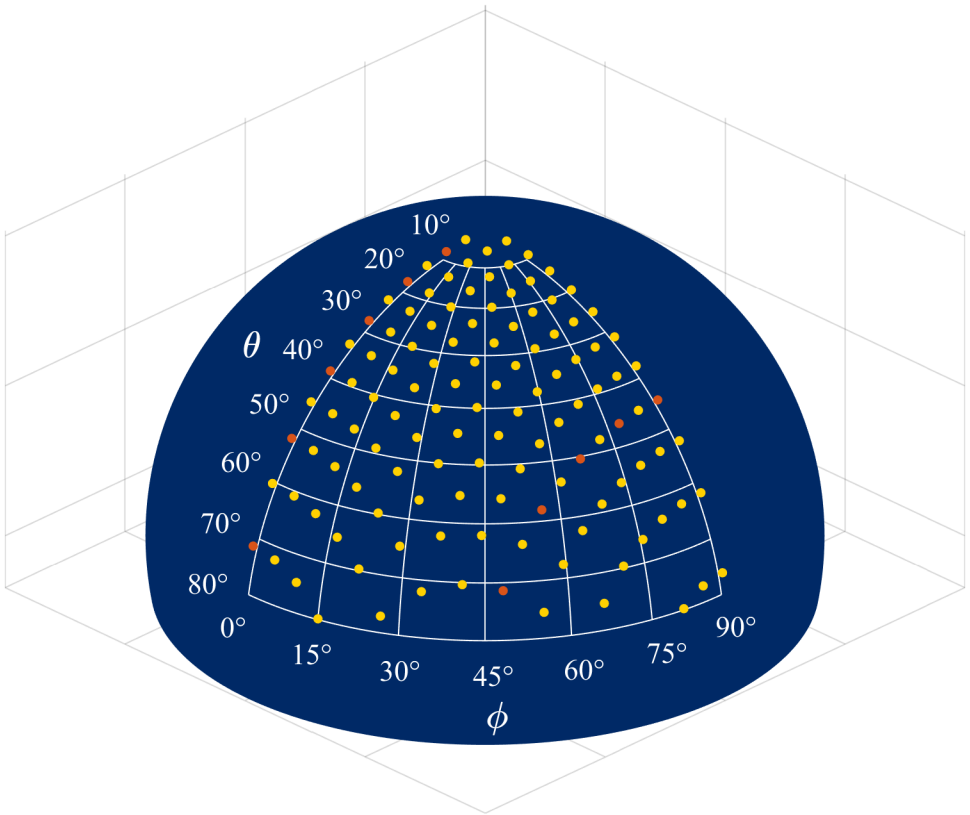


Figure 3.4: Bragg angles in the first octant for 76×17 cm (red dots) and 152×136 cm (yellow dots) rectangular lattices.

each polarization and incidence angle. This increases the computational burden, but it does allow the problem to solved.

This last development is the final piece for summarizing the simulation methodology that will be used: HFSS will be used to solve for fields within a computation domain defined by a unit cell with periodic boundaries, a plane wave excitation, with the inside of the cell being filled with plants and a soil layer. Now the plant and soil structure of the simulation can be discussed.

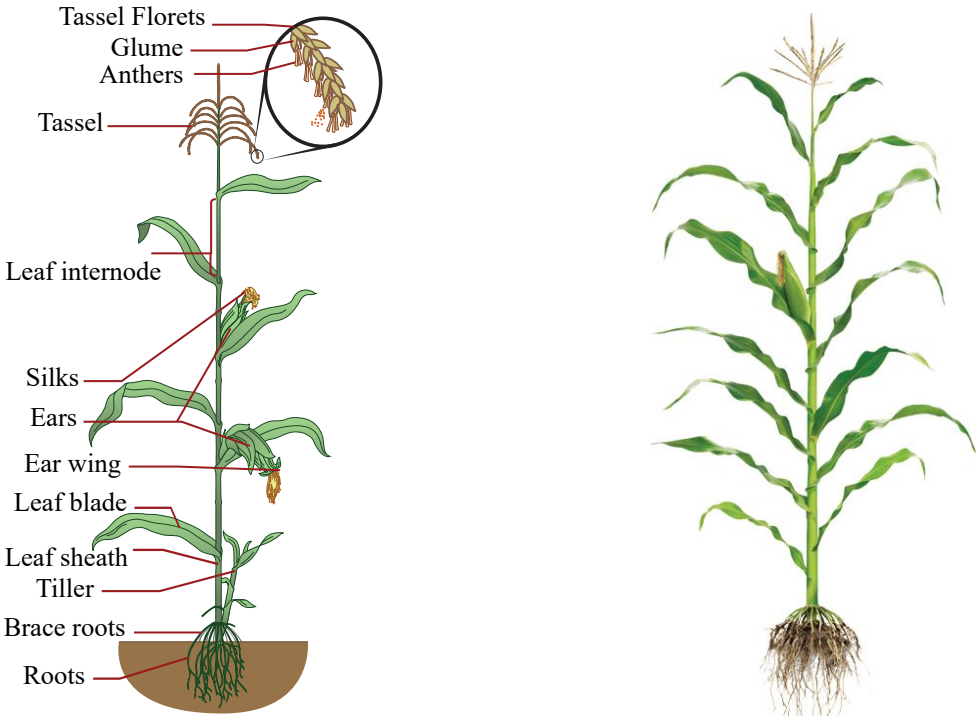


Figure 3.5: High-level anatomy of a corn plant, with a labeled diagram (left) left and an example plant (right).

3.2 Adapting Corn Plants for The Simulation Methodology

3.2.1 Corn Plant Description

There are several components that make up the structure of a mature corn plant, and they are diagrammed in Fig. 3.5. The main plant components are the stalk, leaves, and ears. The stalk of a mature plant can range in size from 1.2 to 4 m tall. Commercial plant varieties usually have one or perhaps two ears per plant. There are also usually around 10 to 16 leaves on a mature plant.

There are several additional components on corn plants. Going from the top to the bottom of the plant, tassels form the male reproductive part of the plant, producing pollen that will ideally be dropped onto the silks of the ears, which make up the female reproductive organ. The glume are leaf-like structures in the flowering cluster of the tassel that surround the male reproductive organ, or stamen, which are made up of anthers and filaments. The spaces between leaves are known as the leaf internodes, and the connection point of each leaf is known as a node. The stalk's nodes

usually exhibit a thicker and stiffer knot of plant material compared with the internodes of the stalk. The nodes also exhibit a collar-like structure where the leaf sheath splits and folds over to form the leaf. The ears of the plant produce kernels and also have silks and ear wings. Each kernel of an ear is connected to a silk, and that silk must be pollinated in order for the kernel to fill and mature. The leaves of the plant usually alternate which side of the plant they grow on. Each leaf contains a stiff spine along its length. A tiller is a separate stalk that grows from the base of the main stalk and is often seen as a nuisance since it diverts nutrients away from the main stalk. Finally, the stalk is supported by roots and brace roots. The brace roots radiate out above the soil line near the bottom of the stalk and help provide extra stability for the plant.

After considering the structure of corn, it was decided that the stalk, leaves, and ears would be the primary contributors to microwave scattering. This is because the tassels contain very little biomass and would probably contribute very little to the backscatter. Tillers were also ignored since they are usually removed if possible. Ear silks were also ignored because, like the tassel, they contain very little biomass and would likely not contribute much to the backscatter as well.

3.2.2 Electromagnetic Representation of Corn Components

The next task was to determine how to represent each of the main components of a corn plant—the stalk, leaves, and ears—in a full-wave electromagnetic simulation. The main aims to satisfy would be maintaining structural and electromagnetic accuracy.

Most biological material can be classified as a dielectric to characterize its interaction with electromagnetic waves. Thus, it is important to assign a realistic value of permittivity to the stalk, leaves, and ears. It would also be helpful if the permittivity could be derived from a quantity that is easier to measure than the dielectric constant. These needs were recognized by researchers some time ago, and the work of Ulaby and El-Rayes provides an empirical formula that can relate the gravimetric moisture content of plant material to its permittivity [145]. The gravimetric moisture content is defined as the weight of water in the plant divided by the total weight of water and plant material. Their work was also based on experiments with corn plants, so their formula is likely to

be a good approximation for the permittivity of a corn plant. Their formulation is given below in (3.4).

$$\epsilon_v = \epsilon_r + v_f\epsilon_f + v_b\epsilon_b \tag{3.4a}$$

$$\epsilon_r = 1.7 - 0.74m_g + 6.16m_g^2 \tag{3.4b}$$

$$v_f = m_g(0.55m_g - 0.076) \tag{3.4c}$$

$$\epsilon_f = 4.9 + \frac{75}{1 + jf_0/18} - j\frac{18\sigma}{f_0} \tag{3.4d}$$

$$v_b = \frac{4.64m_g^2}{1 + 7.36m_g^2} \tag{3.4e}$$

$$\epsilon_b = 2.9 + \frac{55}{1 + \sqrt{jf_0/0.18}} \tag{3.4f}$$

$$\sigma = 1.27 \tag{3.4g}$$

Here, ϵ_v is the permittivity of plant material, and it is made up of a nondispersive residual component ϵ_r, a free-water component $v_f\epsilon_f$ where v_f is the volume fraction of free water and ϵ_f is its permittivity, and a bound-water vegetation component $v_b\epsilon_b$ where v_b is the volume fraction of bound water and ϵ_b is its permittivity. The additional variables are the gravimetric moisture content m_g, the observation frequency in GHz f_0, and the ionic conductivity of aqueous solutions in siemens per meter σ. Exemplary plots of how the permittivity changes versus moisture content are shown in Fig. 3.6.

Th relationship from Ulaby and El-Rayes in [145] allows individual dielectric constants for the stalk, ear, and leaves to be determined from their individual gravimetric moisture contents. It should also be understood that the formulas in (3.4) may not always be correct. Work by Sharma et al. has shown that the above formulas can overestimate the permittivity of tissue in corn plants [131]. They also noted that the plant's tissue at the nodes and internodes is different. Internodes typically have less moisture than the nodes do. This leads to a roughly periodic dielectric profile in the stalk. Again, Sharma et al. showed that an appropriately selected, uniform dielectric constant

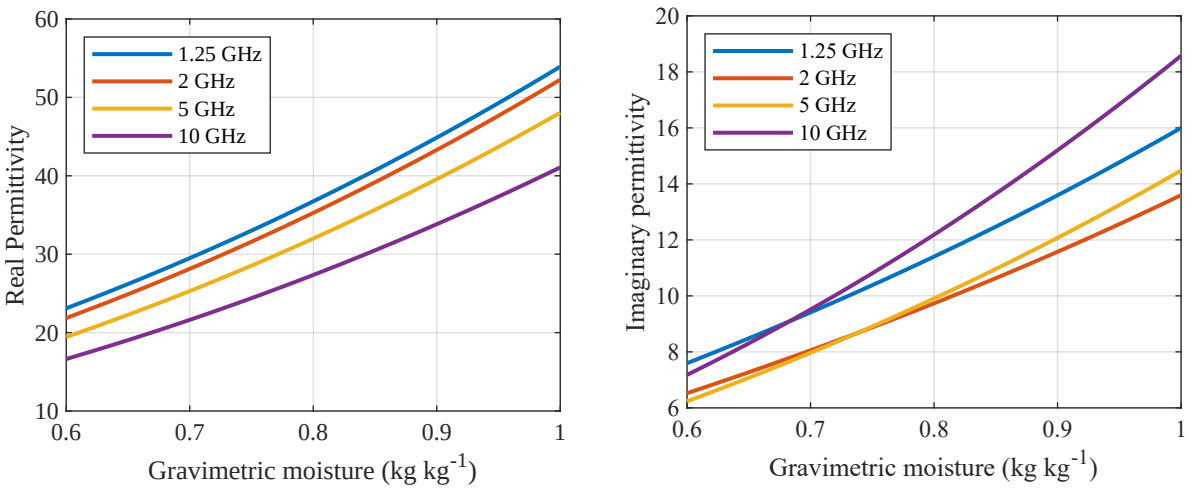


Figure 3.6: Change in vegetation dielectric constant versus gravimetric moisture and frequency.

can still adequately model scattering from the stalk [131]. With these limitations in mind, the formulas from Ulaby and El-Rayes will be used to specify the dielectric properties of the corn plant's components. What remains is to determine how to model the structure of each corn plant component.

The stalk of a corn plant can be represented by a straight, tapered cylinder or cylindrical frustum. The stalk does develop bends as it matures at the nodes near where the ears develop, however much of the stalk remains straight and upright. The leaves on a corn plant are geometrically complex with curves and ruffles. They are also quite thin at around 200 μm. This can present a problem in an FEM simulation where an excess number of elements may be used to mesh a thin leaf. Thus, we use an approximation for the leaves by representing them as a surface, rather than as a volume. This can be done because of work by Senior et al. [129]. This approximation treats the leaf as an infinitesimally thin resistive sheet, where the sheet resistance or impedance is given by

$$Z_{sheet} = \frac{-j\eta_0}{k\tau(\epsilon_r - 1)}, \tag{3.5}$$

where η_0 is the free space impedance, k is the wavenumber, τ is the leaf thickness in meters, and ϵ_r is the relative dielectric constant. Taken to the extremes, an impedance of zero effectively operates as a perfect conductor, while at an impedance approaching infinity, the leaf ceases to exist.

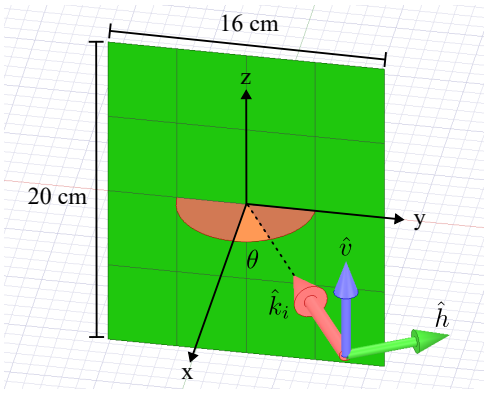


Figure 3.7: HFSS simulation illustration of backscatter from a thin leaf.

A leaf's backscatter can be given in a closed-form expression with the impedance sheet approximation using a Physical Optics (PO) approach. Given below are the expressions for the backscatter from a rectangular sheet with width a and height b as a function of the incidence angle θ as derived in [129].

$$\sigma_{E,H}(\theta) = |\Gamma_{E,H}|^2 \sigma_{pec} \tag{3.6}$$

$$\Gamma_E = \left(1 + \frac{2Z_{sheet}}{\eta}\cos\theta\right)^{-1} \tag{3.7}$$

$$\Gamma_H = \left(1 + \frac{2Z_{sheet}}{\eta}\sec\theta\right)^{-1} \tag{3.8}$$

$$\sigma_{pec} = 4\pi\left[\frac{ab}{\lambda}\cos\theta\,\mathrm{sinc}(ka\sin\theta)\right]^2. \tag{3.9}$$

An exemplary comparison between the PO approach and a full-wave simulation in HFSS gives a sense for how well this approximation works. This was done for a rectangular leaf with $a = 16$ cm, $b = 20$ cm, $\tau = 200$ μm, $\epsilon_r = 29.5 - j9.41$, and $Z_{sheet} = 751 - j2275$ Ω at an observation frequency of 1.25 GHz. The simulation setup is indicated by Fig. 3.7, where $\hat{k}_i$, $\hat{v}$, $\hat{h}$ are the unit vectors for the incident wave, vertical, and horizontal polarizations, respectively. The results of the comparison are shown in Fig. 3.8. It can be seen that the PO and full-wave solutions are in excellent agreement for most of the incidence angles considered.

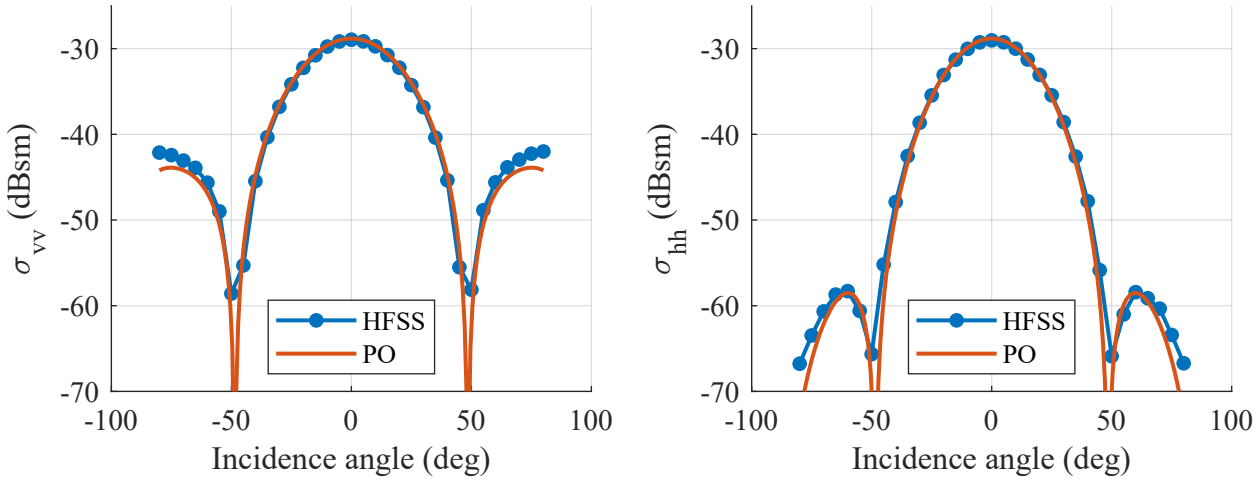


Figure 3.8: Backscatter from a thin leaf as simulated with HFSS and a physical-optics (PO) approximation for vertical (left) and horizontal (right) polarizations.

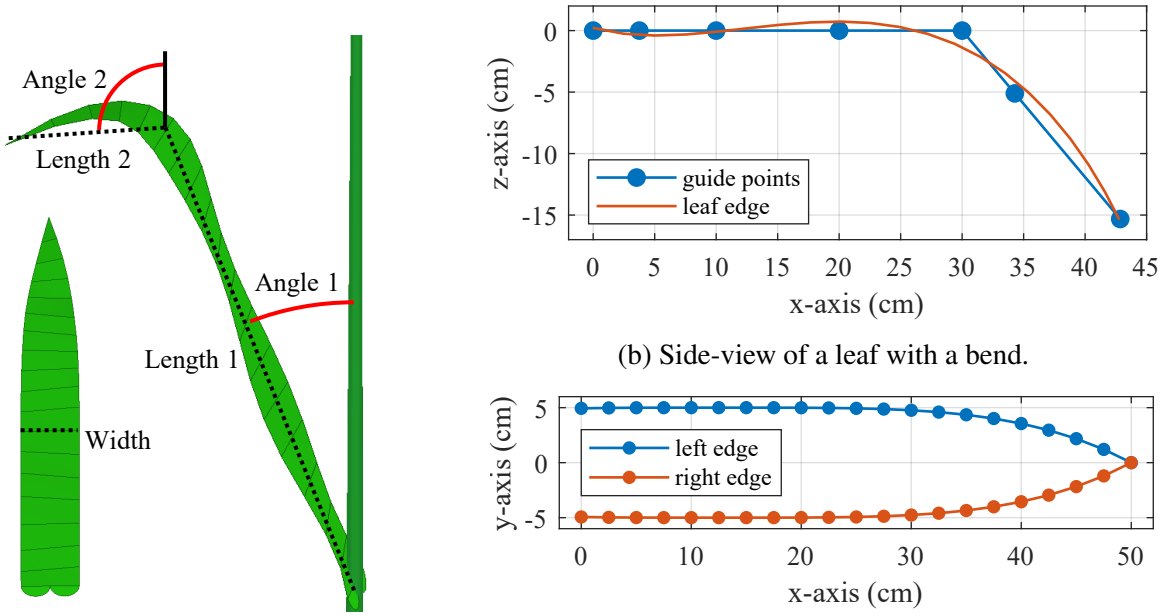
3.2.3 Geometric Representation of Corn Components

3.2.3.1 Leaves

The structure of the leaf is specified with 3-5 variables that are illustrated in 3.9a: total leaf length (length 1 + length 2), leaf width, and the leaf's angle with respect to the stalk (angle 1). Leaves can exhibit a bend near the end of the leaf. In such cases, the length from the stalk to the bend is length 1, the length from the bend to the leaf's tip is length 2, and angle 2 is used to specify the bend's angle. The leaf structure is specified in HFSS in several steps: (1) create two equation-based lines that form the side edges of the leaf, (2) connect these curves with the surface "connect" function, and (3) add two half-circles to the back to emulate the leaf collar.

The first step is accomplished by defining each edge as a parametric function that is given by

$$
\begin{aligned}
x(t) &= L\left(\alpha_4 t^4 + \alpha_3 t^3 + \alpha_2 t^2 + \alpha_1 t + \alpha_0\right) \\
y(t) &= \mp\frac{128W}{81}\left(t - \frac{1}{4}\right)^4 \pm \frac{W}{2} \\
z(t) &= \pm A \sin\left(2\pi t \frac{L}{T_w}\right) + L\left(\beta_4 t^4 + \beta_3 t^3 + \beta_2 t^2 + \beta_1 t + \beta_0\right) \\
&\quad 0 \le t \le 1,
\end{aligned}
$$



(a) Diagram of measurements of a corn leaf.

(b) Side-view of a leaf with a bend.

(c) Top-down view of leaf edges for a flat leaf.

Figure 3.9: Diagrams of leaf measurements and CAD design.

where W is the leaf width, L is the leaf length, A is the amplitude of the ruffles on the leaf edges, T_w is the period of the leaf ruffles, and the α and β coefficients are yet to be determined. The $\pm$ or $\mp$ in the y- and z-coordinates indicate that two lines are required. If there is no bend present on the leaf, then all the coefficients are zero except α_1, which is one. The equations for this case are given below.

$$
\begin{aligned}
x(t) &= Lt \\
y(t) &= \mp \frac{128W}{81}\left(t - \frac{1}{4}\right)^4 \pm \frac{W}{2} \\
z(t) &= \pm A \sin\left(2\pi t \frac{L}{T_w}\right).
\end{aligned}
$$

If there is a bend, though, a least squares approach is used to determine the coefficients α and β. This is done by using several guiding points for the least squares fitting. This is illustrated in Fig. 3.9b, where blue circles indicate the guide points, and the resulting leaf edge is shown in red for a leaf where $L_1 = 30$, $L_2 = 20$, and the bend angle $\theta_b = 50°$ (or angle 2 in Fig. 3.9a). The guide

points for the parameter t and the x and z locations are dynamically defined based on the leaf's specifications with the following vectors

$$\begin{aligned}
\boldsymbol{t} &= 1/L * [0, 0.125L_1, 0.333L_1, 0.667L_1, L_1, L_1 + 0.333L_2, L]^T \\
x_0 &= L_1 + L_2/3\cos(\theta_b) \\
x_1 &= L_1 + L_2\cos(\theta_b) \\
\boldsymbol{x} &= [t_0, t_1, t_2, t_3, t_4, x_0, x_1]^T \\
z_0 &= -L_2/3\sin(\theta_b) \\
z_1 &= -L_2\sin(\theta_b) \\
\boldsymbol{z} &= [0, 0, 0, 0, 0, z_0, z_1]^T,
\end{aligned}$$

where boldface type indicates a vector and $L = L_1 + L_2$. The width of the leaf varies by the 4th power along its length such that it reaches the nominal width one-quarter of the way along the leaf ($t = 1/4$), is slightly narrower at the beginning ($t = 0$), and tapers to 0 at the tip. This is illustrated in Fig. 3.9c for a flat leaf with a width of 10 cm. Finally, the ruffles are $180°$ out of phase between the left and right edges. The ruffle period T_w is nominally 30 cm, but this is adjusted when the leaf model is generated such that there are an integer number of half-cycles along the length of the leaf.

3.2.3.2 Ears

The geometry for the corn ears is based on measurements of ear length and radius. The shape of the ear is defined heuristically with an approximate shape that can then be scaled to fit the length and radius requirements. The shape is a body of revolution around the z-axis, and its outline is given by

$$\begin{aligned}
\boldsymbol{z} &= L_{ear}[0, 0.15, 0.17, 0.19, 0.23, 0.48, 0.83, 0.93, 0.98, 1.00]^T \\
\boldsymbol{x} &= \pm r_{ear}[0.4, 0.6, 0.8, 0.95, 1, 1, 0.85, 0.7, 0.4, 0.1]^T.
\end{aligned}$$

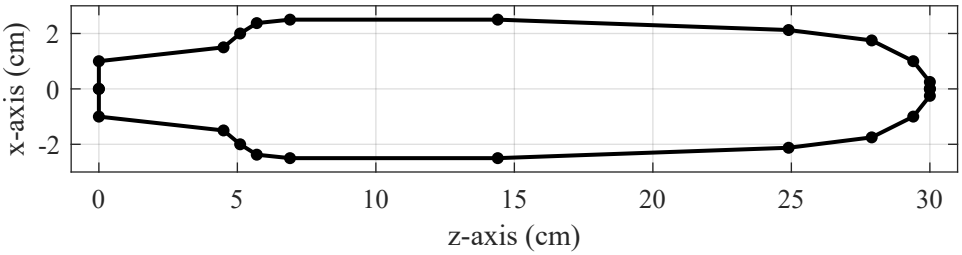


Figure 3.10: Ear outline.

This outline is illustrated in Fig. 3.10 for an ear 30 cm long with a 2.5 cm maximum radius.

3.2.3.3 Stalk

The stalk is based on measurements of stalk length, bottom circumference, and top circumference. These measurements are then used to define a frustum for the stalk's shape.

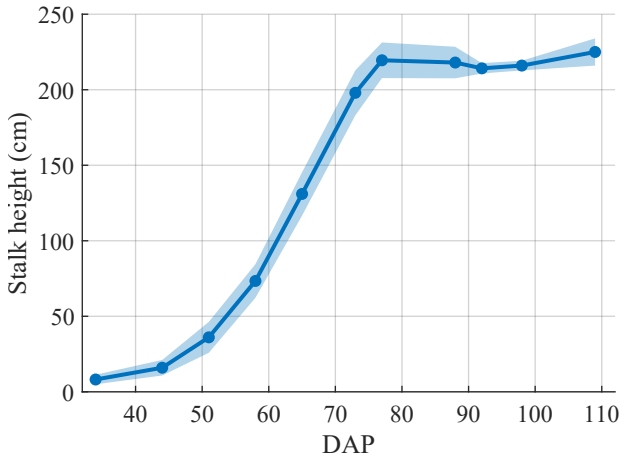
The CAD models for the stalks, leaves, and ears of a corn plant are each created first in HFSS with templates, and the resulting CAD model is exported and saved. A corn plant is then assembled from the previously created components. Each piece is sized, oriented, and located in accordance with the angles and positions defined by the plant dataset from the University of Florida.

3.2.4 University of Florida Dataset

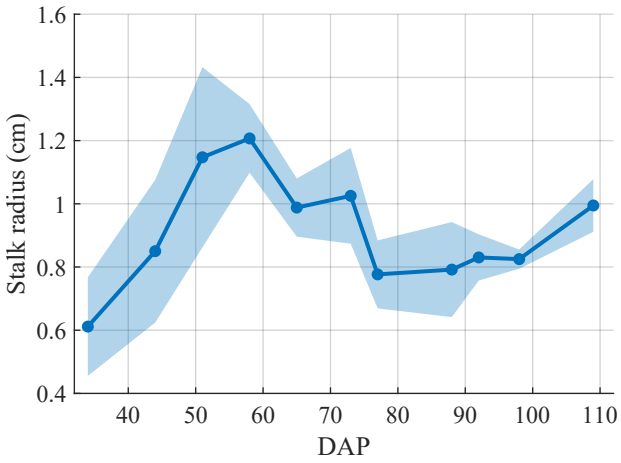
Information on the geometry of each plant component is provided by a dataset from the University of Florida [62]. The dataset lists each component and its measurements as found on real corn plants over the course of a complete growth cycle. Each component was captured at specified days since it was planted, or the DAP. For the stalk, this would include height and top and bottom circumferences. For the leaves, this would include leaf height, width, length 1, angle 1, and length 2 and angle 2 if there is a bend present. If an ear was present, then its height (position on the stalk), length, radius, and angle from the stalk were recorded.

The entries from each of these items was then organized into a dataset that could be analyzed for relationships between measurements and the DAP, as well as with respect to the measurements of other plant components. This analysis is captured in Figs. 3.11–3.13. The surface plots show

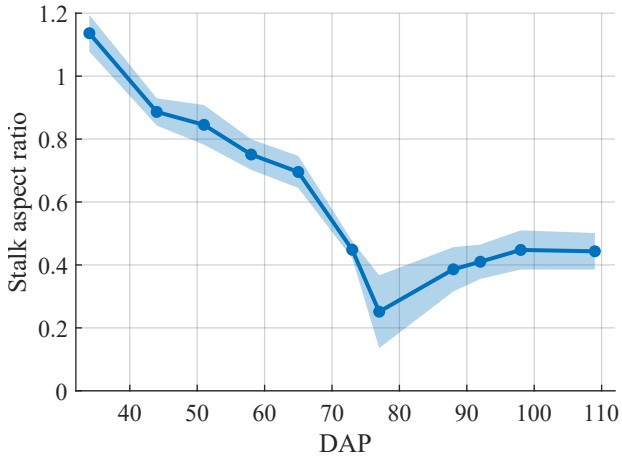
versions of the data that have been smoothed from the original. The solid lines in those plots (where applicable) indicate the average value for that quantity, while the shaded area shows one standard deviation away from the average. The DAP of each measurement is indicated with circular markers because measurements were not taken every day. For the 3D plots, the average value is given by the surface in solid colors, and the deviation is indicated by the lighter, transparent surfaces. All the surface plots use the DAP or the normalized height of the plant component (norm. h) as the independent values. The normalized height of a plant component describes where it is on the stalk, with 0 being at the bottom, and 1 at the top. To illustrate how this is used, consider Fig. 3.12b, which shows the total leaf length. This surface indicates that the longest leaves (about 80 cm) start appearing around DAP 60 and occur about halfway up the stalk. The normalized leaf separation in Fig. 3.12a is also with respect to the height of the stalk. Figure 3.12e is the only surface plot without an indication of the deviation. This is because the bend probably was calculated by taking the number of leaves with a bend at a particular DAP and height on the plant, and then dividing it by the total number of leaves at that DAP and height. The stalk radius in Fig. 3.11b shows the average of the stalk's top and bottom radii, and the stalk aspect ratio in Fig. 3.11c shows the ratio between the top and bottom radius.



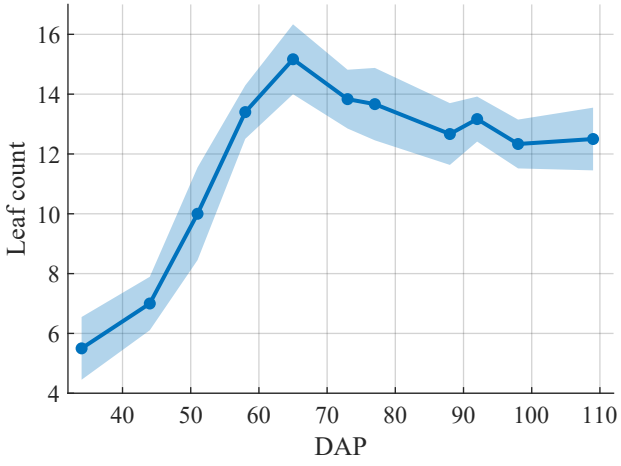
(a) Stalk height.



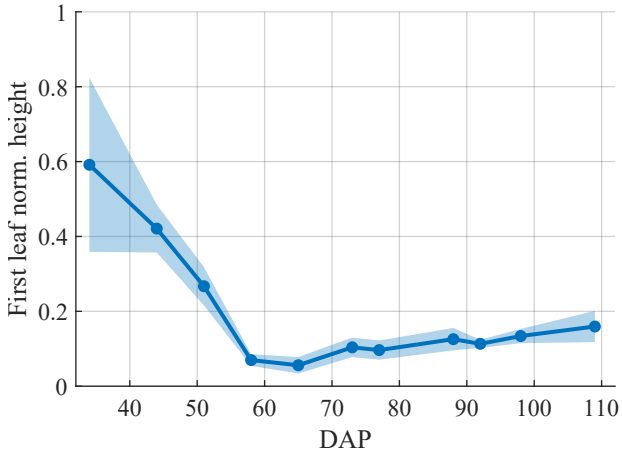
(b) Stalk radius.



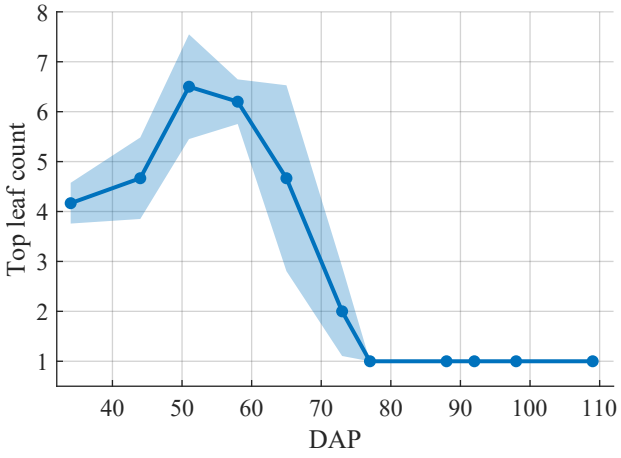
(c) Stalk aspect ratio.



(d) Leaf count per stalk.

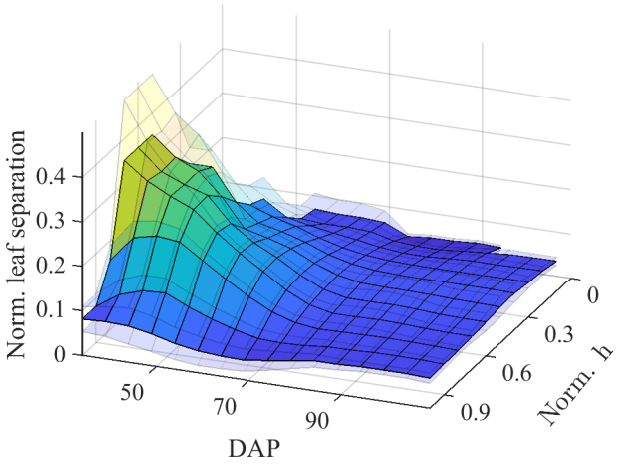


(e) Normalized height of a stalks first leaf.

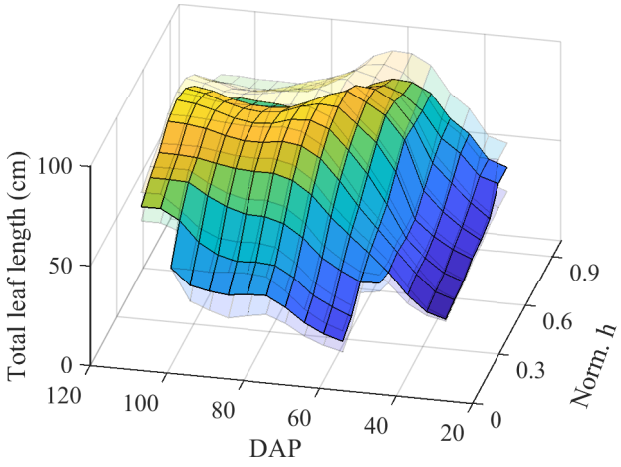


(f) Number of leaves at the top of the stalk.

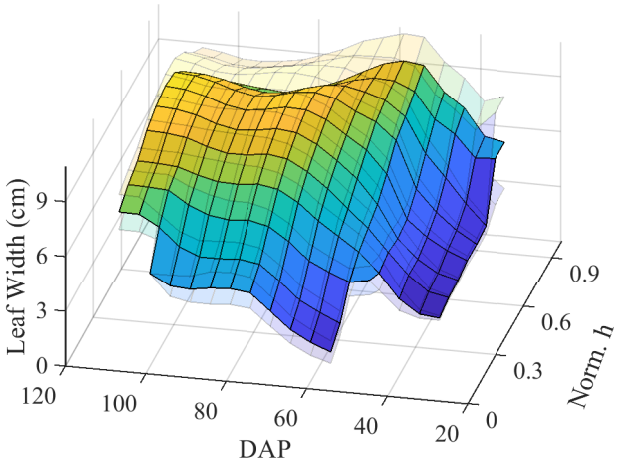
Figure 3.11: Corn stalk metrics versus the DAP based on data from the University of Florida.



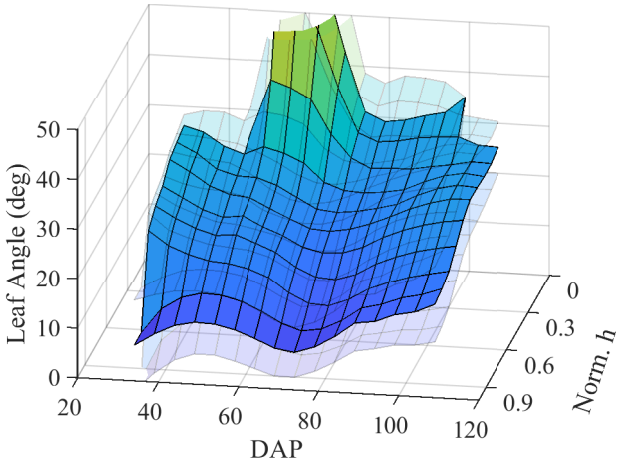
(a) Separation between leaves.



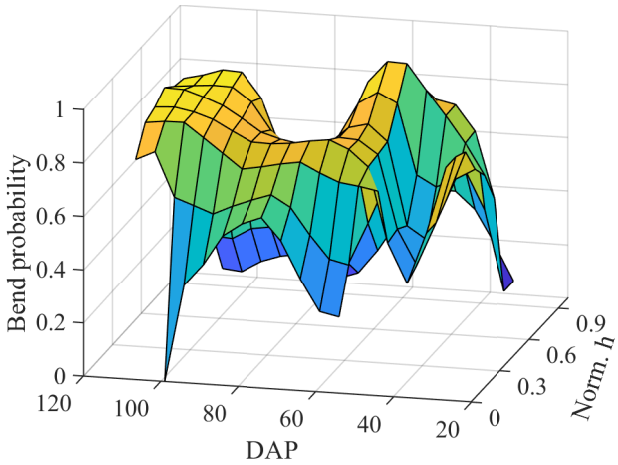
(b) Total leaf length.



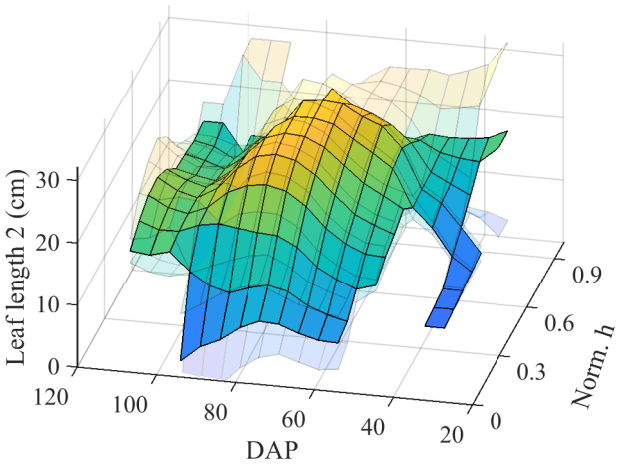
(c) Leaf width.



(d) Leaf first angle from stalk.

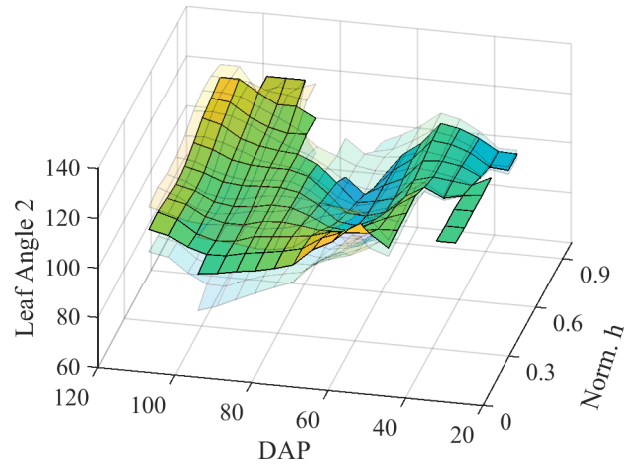


(e) Probability of a bend in a leaf.

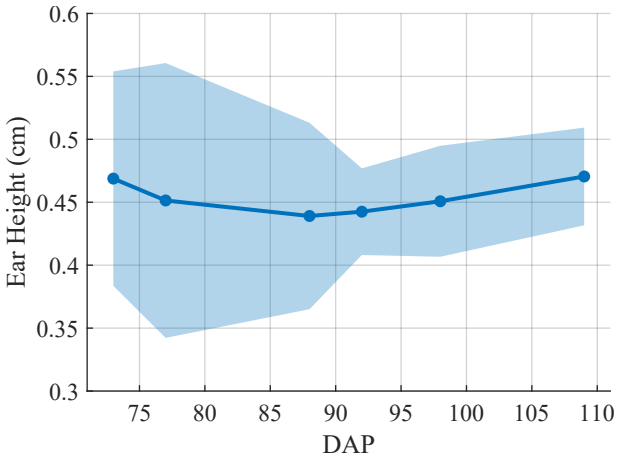


(f) Length of bent portion of leaf.

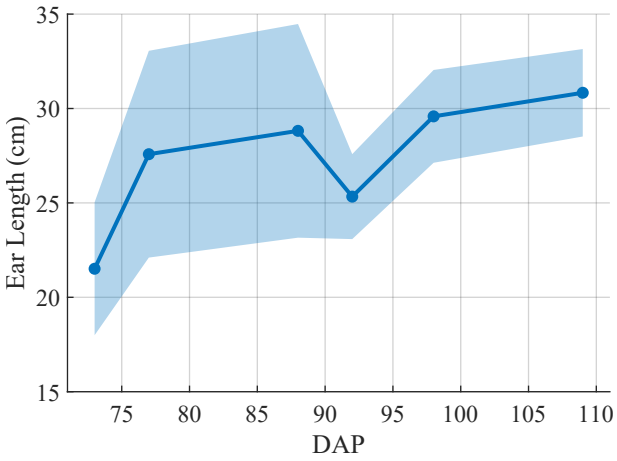
Figure 3.12: Metrics for corn plant leaves versus the DAP based on data from the University of Florida.



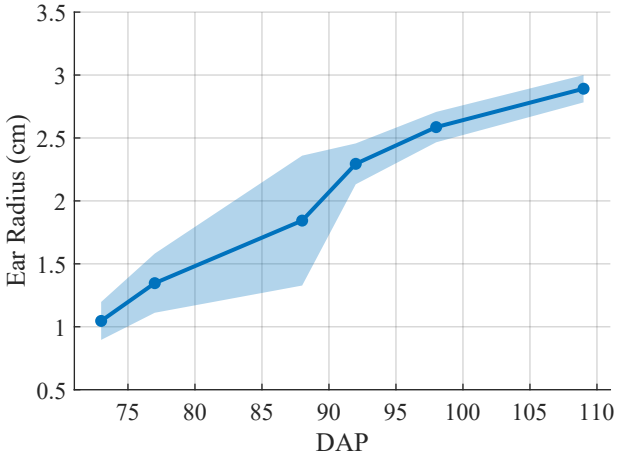
(a) Leaf bend angle.



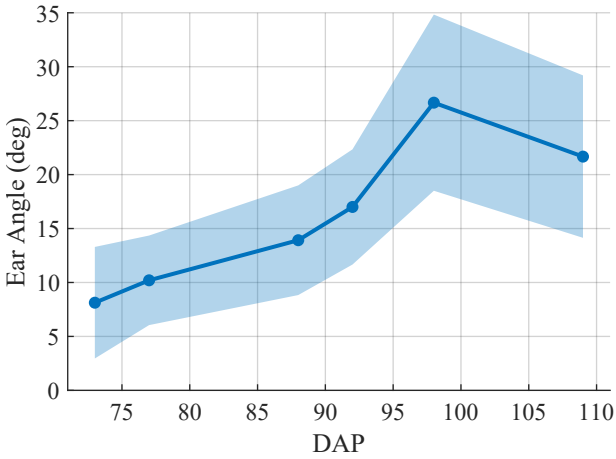
(b) Height of ear.



(c) Ear length.



(d) Ear radius.



(e) Ear angle vs DAP.

Figure 3.13: Metrics for corn plant leaves and ears versus the DAP based on data from the University of Florida.

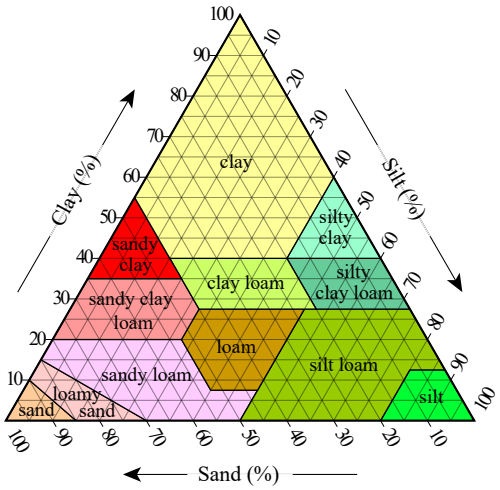


Figure 3.14: Soil texture diagram from [27].

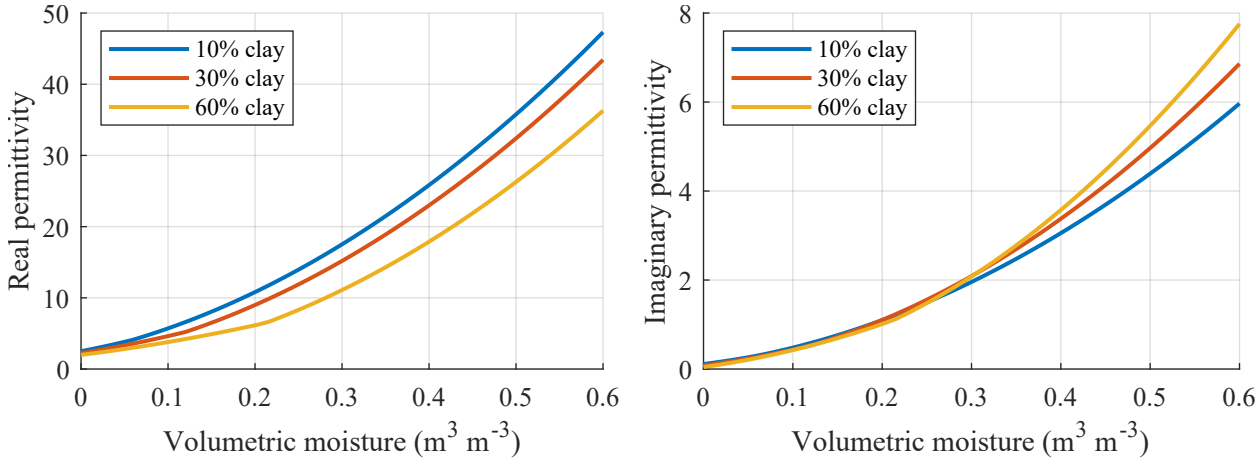
The data from each of those figures can be used to generate realistic CAD models of the corn plant components and to assemble those components together to make a realistic, data-based corn plant.

3.3 Soil Model

Like the plant model, the model used for the soil includes (1) the dielectric properties of the soil and (2) a 3D CAD model of the soil surface. Each of these are explained below.

3.3.1 Soil Dielectric Constant

The dielectric constant of soil is driven by its material composition. A major component of that is any water dispersed in the soil since water has a very high dielectric constant at microwave frequencies. The water content or SMC is also a quantity that can rapidly change. The other major components of soil that are important for describing its texture and composition are its clay, silt, and sand content. These soil components are categorized based on soil particle sizes, where clay includes grain sizes from 0-2 μm, silt includes 2-50 μm grains, and grain sizes of 50-2000 μm are classified as sand. There are 12 different soil texture classifications in the US that are based on the



(a) Real soil permittivity.

(b) Imaginary soil permittivity.

Figure 3.15: Permittivity for soil versus water content as formulated by Mironov et al. in [86].

relative composition of clay, silt, or sand in a soil [30]. These classifications can be organized as a soil texture triangle as defined by the USDA and shown in Fig. 3.14.

The soil permittivity is specified using the formulas developed by Mironov et al. [86], which relates the soil's clay content and volumetric water content to the permittivity. The characteristics of this formulation are shown in Fig. 3.15 for 1.25 GHz. It can be seen that increased clay content lowers the real part of the permittivity, increases the imaginary part of the permittivity (more loss), and of course wetter soils have a higher overall permittivity.

3.3.2 Soil Structure

The physical structure of a soil surface is very important for deriving its scattering characteristics. Soil scattering falls under the consideration of scattering from rough surfaces. In the literature, these surfaces (at least for soil) are represented by a zero-mean Gaussian process where the height of the soil at any point along its surface is given by $z(x, y) \sim \mathcal{N}(0, h_{rms}^2)$, where $\mathcal{N}$ indicates a normal distribution with mean 0 and variance h_{rms}^2. The heights of two adjacent points are related by the correction function, which usually depends on the distance R between them for an isotropic surface. This looks like $\rho(z_0, z_1) = \rho(R)$, and there are a few choices for $\rho(R)$ such as a Gaussian,

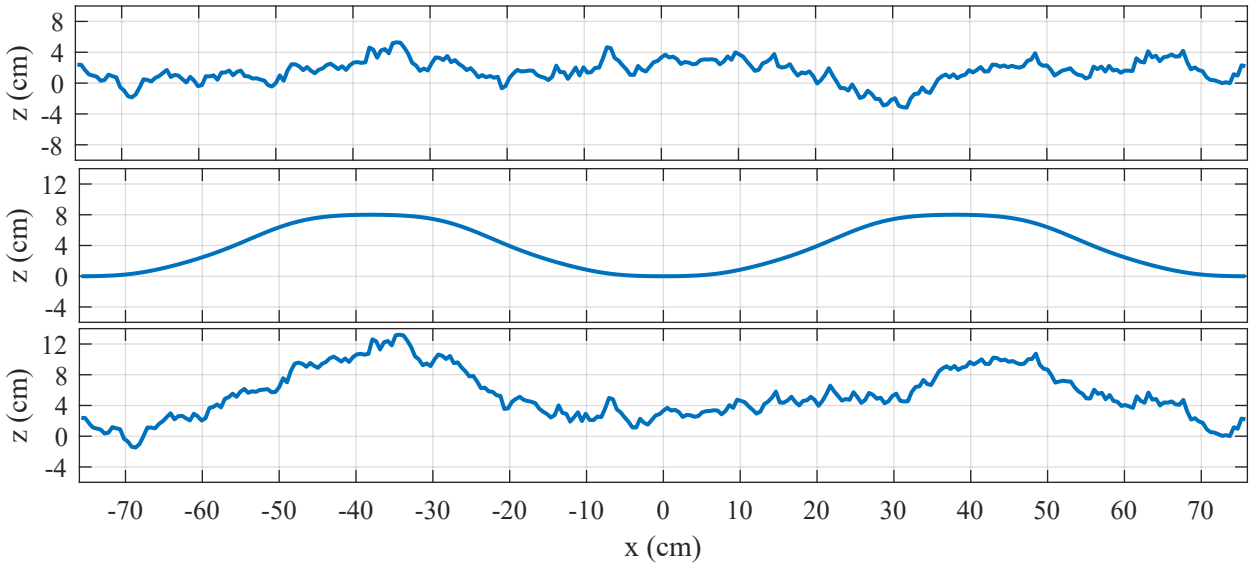


Figure 3.16: A 1D profiles of soil surfaces: (top) a Gaussian rough surface with an exponential correlation function, (middle) a furrow structure defined as a combination of sinusoids, and (bottom) their summation.

exponential, or power correlation function. Typically, the correlation function of natural surfaces can be approximated by the exponential or power correlation function. There is also a measure called the correlation length l_{corr} that indicates how correlated adjacent locations are, and thus how smooth the surface might be. The correlation length is defined as the distance where the correlation equals e^{-1} for most correlation functions, but not all. A 1D example of a Gaussian rough profile with an exponential correlation function is shown in the top subplot of Fig. 3.16. Additionally, $h_{rms} = 2$ cm and $l_{corr} = 12$ cm for that profile.

There can also be other structural features of the soil profile in an agricultural field besides a random roughness component. Many fields undergo tilling that introduce parallel ridges and troughs, or furrows, into the soil surface's profile. This could be modeled by using a combination of sinusoids, and this is shown in the middle subplot of Fig. 3.16 to represent the furrows. In that example, the spacing between furrows is 76 cm, which is a typical row spacing for corn fields. A random rough height component can also be added to the furrow profile to give a rough furrow profile. That is shown in the bottom subplot of Fig. 3.16.

A Gaussian random soil profile can be straightforward to generate with the right software tools

like MATLAB or NumPy and SciPy. There are a few aspects that must be carefully considered, though. The MATLAB function `mvnrnd` makes it easy to make the soil profile. It can accept two arguments `mu` and `Sigma`, where `mu` is a vector of average values and `Sigma` is a covariance matrix. If one would like to create N random heights to make up the soil profile, then `mu` would be a length N vector of zeros, and `Sigma` would be an $N \times N$ covariance matrix, where the covariance will be defined based on h_{rms} and the correlation function, which will mainly be a function of the lateral distance between two different points.

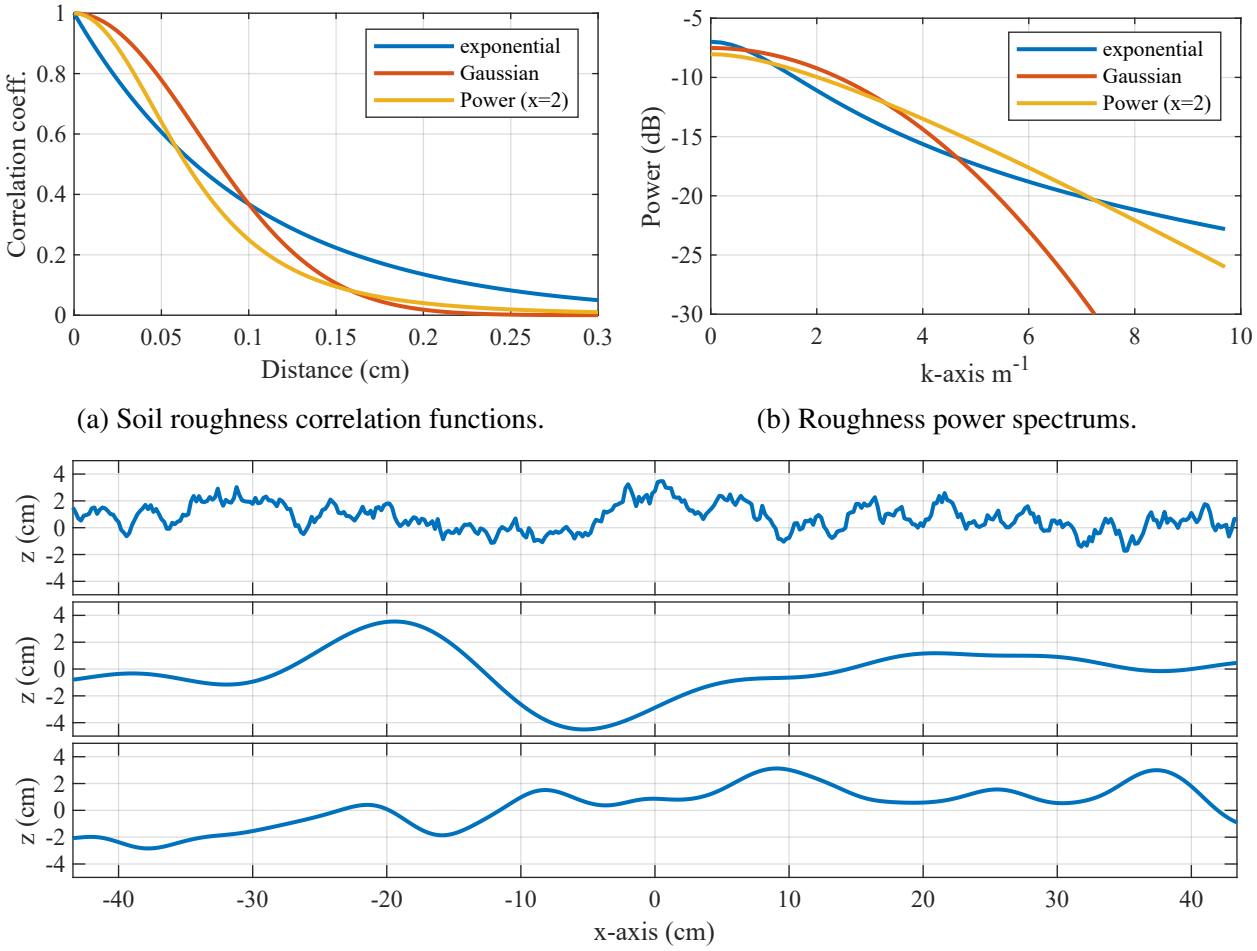
The point that requires careful consideration is when using a function like `mvnrnd` to generate profile heights that can then be used to define a mesh for a CAD model of the soil. The soil profile must be sampled at discrete locations in order to do this. If the distance between sample locations is too big, then the CAD surface profile will not have the desired correlation function characteristics. This is very similar to the problem of Nyquist sampling of a time-domain signal like audio: the sample rate has to be at least twice as much as the highest frequency in the audio.

3.3.2.1 Determining Sampling Period

The soil profile's correlation function can also be characterized in the frequency domain using the power spectrum of the rough surface, which is a scaled version of the Fourier transform of the correlation function. The power spectrums $W(k)$ for a Gaussian, exponential, and power correlation function can be seen in Fig. 3.17, along with the associated correlation functions and some 1D profile examples. Their equations are also given below.

$$\begin{array}{lll} \text{Gaussian} & \text{Exponential} & \text{Power } (x=2) \\ w(r) = e^{-r^2/l^2} & w(r) = e^{-r/l} & w(r) = \dfrac{1}{(1+r^2/l^2)^x} \\ W(k) = l\sqrt{\pi}e^{-k^2l^2/4} & W(k) = \dfrac{2l}{1+k^2l^2} & W(k) = \dfrac{\pi l}{2}(|k|l+1)e^{-|k|l} \end{array} \tag{3.10}$$

We note that each power spectrum has nearly infinite support over all spatial frequencies. This means that there will be some amount of aliasing if we sample a rough surface with any of these



(a) Soil roughness correlation functions.

(b) Roughness power spectrums.

Figure 3.17: Plots of the exponential, Gaussian, and power correlation functions, their associated power spectrums, and 1D profile examples: exponential (top), Gaussian (middle), power (bottom).

power spectrums, and that will reduce how accurately a 3D mesh can represent the desired soil surface. How much aliasing can be tolerated then?

To perhaps answer that question, consider a study by Chen et al. that discusses some analytic rough surface models [23]. They derive an expression for the polarimetric scattering cross section σ^0_{qp} of a rough surface in equation (18), and it shows that σ^0_{qp} is proportional to the power spectrum, evaluated at a point in k-space that depends on the transverse incident and scattered wave vectors $\vec{k}_s$ and $\vec{k}_i$: $\sigma^0_{qp} \propto W^{(n)}(k_{sx} - k_{ix}, k_{sy} - k_{iy})$, where W is the power spectrum. In the case of backscatter, this becomes $W^{(n)}(2k_{ix}, 2k_{iy})$, or $W^{(n)}(2k_0 \sin\theta_i)$ if the power spectrum is isotropic. Thus, if we take the specific case of a 1.25 GHz wave that is incident on the ground at $\theta_i = 60°$, then the power spectrum will be evaluated at $W^{(n)}(45.38\,\mathrm{rads/m})$. This means that the sampling

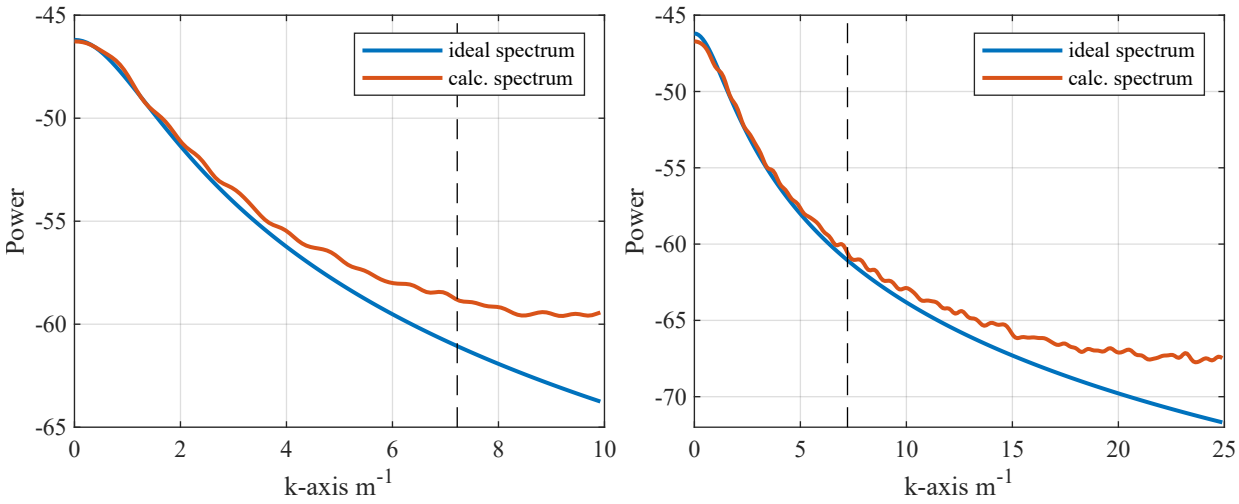


Figure 3.18: Comparison of the power spectrum of a sampled, exponential surface with its ideal spectrum, with $\Delta x = 5$ cm (left) and $\Delta x = 2$ cm (right).

period of the rough surface should be small enough so that the power spectrum of the sampled surface at $45.45\,\mathrm{rads/m}$ is close to the ideal power spectrum of the surface. The radial spatial sampling frequency is given by $\Omega_s = 2\pi/\Delta x$. Following the Nyquist rule, $\Omega_s = 91\,\mathrm{rads/m}$, and Δx should at most be 6.9 cm between samples.

But this sampling period is only just enough to accommodate 45.38 rads/m, which means that the power spectrum of the sampled surface will be evaluated at the spectrum's edge where aliasing effects will be greatest. Thus, a finer sampling period must be used. This is illustrated by Fig. 3.18, where the average power spectrum of a 1D profile with a sampling period of 5 cm is compared to another with a sampling period of 2 cm. The same surface statistics were used in each case: $h_{rms} = 1$ cm, $l_{corr} = 12$ cm, an exponential correlation function, and a profile length of 2 m. The average spectrums were computed using Bartlett's method for spectrum estimation with 1,000 independent spectrums. The average, calculated spectrums are shown in red, with the ideal spectrums without aliasing shown in blue. The spatial frequency of interest 45.38 rads/m or 7.22 m^{-1} is shown as the black, dashed line. It can be seen that the error due to aliasing in the 5 cm case is significant, and in the 2 cm is very small. This shows that the sampling period can be chosen such that the sampled rough surface's power spectrum, on average, is very close to the ideal spectrum at the spatial frequency of interest. It also shows that using the Nyquist criteria for determining the sampling

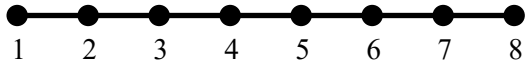


Figure 3.19: Sample points along the x-axis of a 1D surface profile.

period is insufficient, at least for an exponential correlation function.

3.3.2.2 Creating a Periodic Surface

The other fine point about creating the soil profiles comes into play because of the periodic boundaries that will be utilized in the simulation method. This means that the generated rough surfaces must also be periodic. How this can be done is considered in the following example. Let us say that we restrict ourselves to a 1D surface profile and only consider eight sample points that we need to determine the height for as shown Fig. 3.19. If we use `mvnrnd`, we need a vector of means `mu` for each point and a matrix of covariances between each sample point C. The mean is straightforward: it's all zeros. The covariance matrix can be filled in a loop where each entry will be given by (assuming an exponential correlation function)

$$d_{mn} = |x_m - x_n| \tag{3.11}$$

$$c_{mn} = h_{rms}^2 e^{-d_{mn}/l_{corr}} \tag{3.12}$$

$$C = \begin{bmatrix} c_{11} & \dots & c_{1N} \\ \vdots & \ddots & \vdots \\ c_{M1} & \dots & c_{MN} \end{bmatrix}. \tag{3.13}$$

Here, c_{mn} are the entries of the 8×8 matrix, and d_{mn} is the Euclidean distance between each sample point. In the normal case, the shortest distance (besides 0) will be between adjacent points, and will fill entries on the diagonals on either side of the main diagonal of the matrix. The longest distance will occur between the end points, and this will fill the entries in the top right and bottom left corners. Using the `mu` vector of zeros and C with `mvnrnd` will provide a random surface profile with the desired characteristics, but it will not be periodic. How can this be adjusted so that

a periodic profile is obtained?

Notice that if the profile is periodic, then the endpoints are actually the same point. Also, point x_1 would only be separated by one sample from x_7, rather than the nominal six samples. The longest possible distance, then, would be 3, since the periodic distance of x_1 to x_4 is the same as x_1 to x_5 because x_1 and x_8 are the same point. To reflect this observation, the distance between points needs to be modified:

$$d_{mn} = |x_m - x_n| \tag{3.14}$$

$$\tilde{d}_{mn} = \min(d_{mn}, L - d_{mn}) \tag{3.15}$$

$$\tilde{c}_{mn} = h_{rms}^2 e^{-\tilde{d}_{mn}/l_{corr}}. \tag{3.16}$$

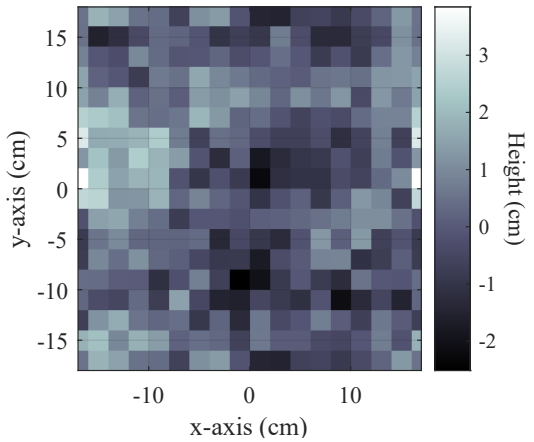
$$\tilde{C} = \begin{bmatrix} \tilde{c}_{11} & \dots & \tilde{c}_{1N} \\ \vdots & \ddots & \vdots \\ \tilde{c}_{M1} & \dots & \tilde{c}_{MN} \end{bmatrix}, \tag{3.17}$$

where L is period of the profile. It is possible to create periodic surfaces by extending this method to 2D. Figure 3.20 shows an example of a periodic 2D surface, and Fig. 3.21a shows a 3D view of a rough surface. Another consequence of having a periodic profile is that, like scattering, the power spectrum is only nonzero for discrete spatial frequencies. And it turns out that the values of these spatial frequencies, that of scattering and periodicity, are the same.

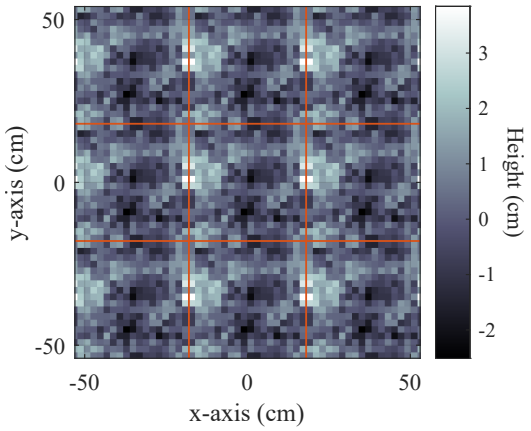
To see why this is, the power spectrum of a periodic surface is first derived as follows. In 1D, begin with the correlation function $w(x)$ of a non-periodic surface such as the exponential one. This can made periodic by first truncating it with a rectangular window of length L and then convolving it with a pulse train of period L:

$$\tilde{w}(x) = \left(\text{rect}\left(\frac{x}{L}\right) \cdot w(x)\right) * \sum_{n=-\infty}^{\infty} \delta(x - nL). \tag{3.18}$$

These steps are equivalent to convolving the power spectrum W with a sinc function and then



(a) Single tile of a rough, periodic surface.



(b) Nine rough, periodic tiles arranged to demonstrate periodicity.

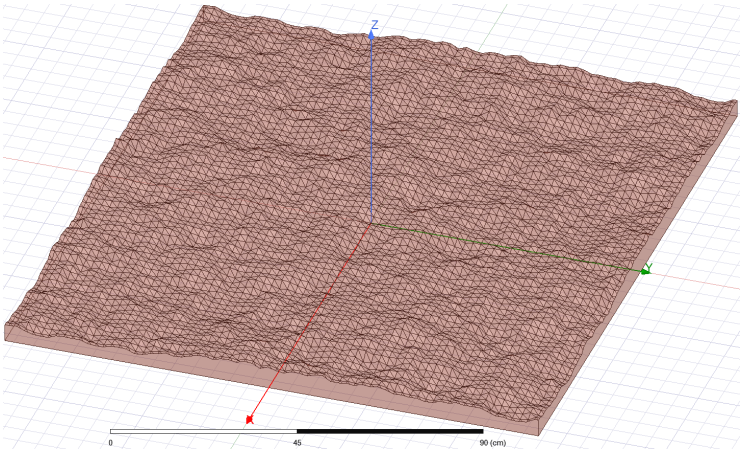
Figure 3.20: A 2D version of a periodic rough surface.

multiplying it with another pulse train

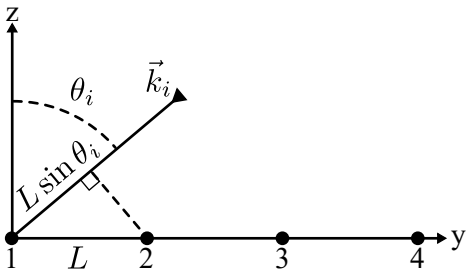
$$\tilde{W}(k) = \left(L \operatorname{sinc}\left(\frac{kL}{2}\right) * W(k) \right) \cdot \frac{2\pi}{L} \sum_{n=-\infty}^{\infty} \delta\left(k - n\frac{2\pi}{L}\right). \tag{3.19}$$

This last function is only nonzero for $k = 2\pi n/L$. When it comes to the allowed θ_i for backscatter, that can be derived as follows for the 1D case.

Consider Fig. 3.21b, which shows an infinite array of periodically spaced scatterers along the y-axis. The spacing between them is L. This array is illuminated by an incident plane wave with wavevector $\vec{k}_i$ at an angle θ_i. It can be seen that the scattered waves from point 1 and 2 will constructively interfere in the backscatter direction if the distance $2L \sin\theta_i$ is some multiple of a wavelength, or $2k_0 L \sin\theta_i = 2\pi m$. The expression $2k_0 \sin\theta_i$ can be found in the argument of the power spectrum W earlier in section 3.3.2.1. Rearranging the equation in terms of this quantity, we obtain $2k_0 \sin\theta_i = 2\pi m/L$, which expresses the same valid k-space values as the prior derivation for the spectrum of a periodic surface.



(a) 3D view of a periodic rough surface.



(b) Regularly-space scattering points on a line.

Figure 3.21: A 3D view of a rough, periodic surface (left) and a diagram of a plane wave incident on an array of regularly-spaced points (right).

3.4 Plane Wave Equivalence Validation

Earlier, Section 3.1 explained that the Floquet port excitation for the periodic simulation was replaced by a plane wave excitation in HFSS due to the mode limit for a Floquet port. Making this switch was tested by performing a simulation experiment to verify that both excitations would produce similar results. The experiment ran five random realizations of three different scenarios: 1) a Floquet port excitation with a PML on the bottom, 2) a Floquet port with an impedance boundary on the bottom, and 3) a plane wave excitation with an impedance boundary on the bottom. 3D views of the plant and simulation structure for each scenario are shown in Fig. 3.22. A realization was created by randomizing the orientations of each plant. The plant structure was also the same across different scenarios. A flat soil layer 7 cm thick was also included in all simulations with a permittivity of $19.4 - j0.9$. The backscattering coefficient values from these simulations were then calculated for $\phi_i = 0°$ and $\theta_i = 39.1344°$ and are compared in Table 3.1, where PML, Z, and PLW are the labels for the first, second, and third scenarios respectively. The average backscatter is also shown. It can be seen that the differences between the methods are less than 1 dB, except for realization 4 of σ^0_{vh} and realization 1, 3, and 5 of σ^0_{hv}. These differences are small enough on

Table 3.1: Comparing the backscattering coefficient of three simulation configurations to assess if the plane wave excitation can replace the Floquet port excitation.

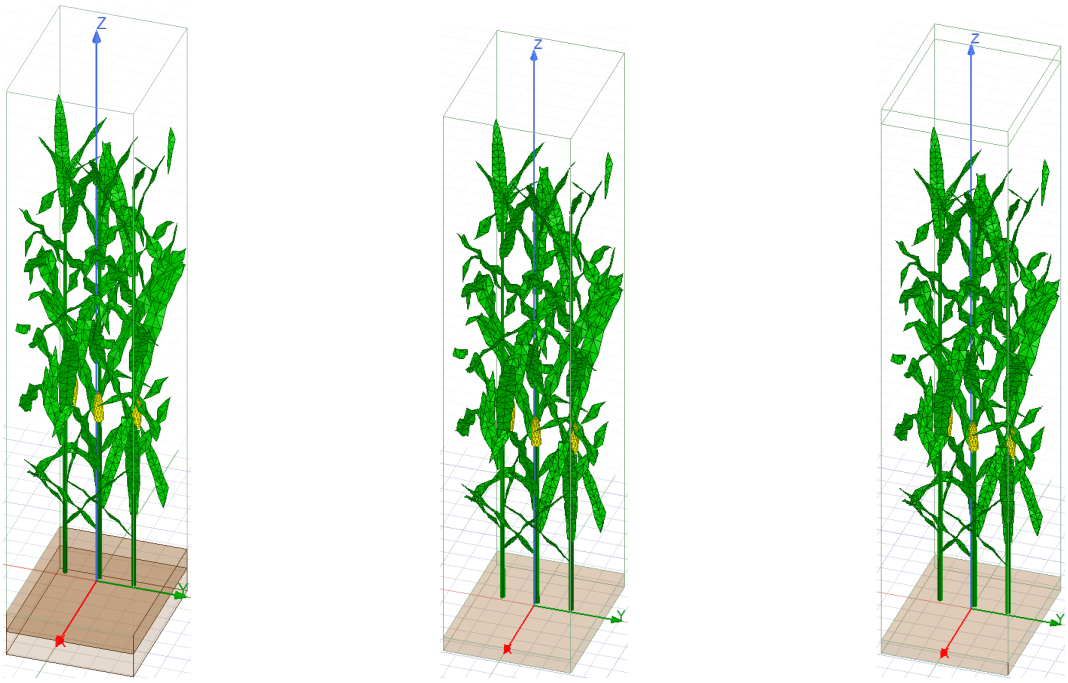
	σ^0_{vv} (dB)			σ^0_{hh} (dB)			σ^0_{vh} (dB)			σ^0_{hv} (dB)		
Real.	PML	Z	PLW	PML	Z	PLW	PML	Z	PLW	PML	Z	PLW
1	-1.26	-1.10	-1.11	-6.67	-6.61	-5.89	-32.5	-31.6	-32.6	-32.5	-31.5	-33.1
2	-6.65	-6.66	-6.55	-4.56	-4.62	-4.21	-29.0	-28.2	-28.9	-29.0	-28.2	-27.9
3	-5.76	-5.61	-5.51	-6.12	-6.10	-5.67	-30.7	-30.7	-31.3	-30.6	-30.9	-32.9
4	-0.07	0.05	0.00	-5.44	-5.33	-4.69	-27.6	-27.9	-29.6	-27.6	-27.9	-27.8
5	-1.88	-1.75	-1.80	-3.20	-3.15	-3.04	-34.7	-34.6	-34.1	-34.4	-34.7	-39.4
Avg.	-2.42	-2.30	-2.31	-5.02	-4.99	-4.57	-30.2	-30.0	-30.9	-30.2	-30.0	-30.6

average, though, that it is reasonable to replace using a Floquet port with a PML on the bottom with a plane wave excitation and an impedance boundary on the bottom of the simulation domain.

3.5 Canopy Row Structure

Section 3.1 discussed some of the implications of using periodic boundaries to simulate the radar backscatter from a field of corn plants. This section takes a closer look at some of the effects that may be observed from a vegetation canopy with a regular structure like rows.

The physical structure and the material properties of corn plants are important for predicting their backscatter coefficient. The physical relationship between plants, namely their physical locations, is also important because corn is usually found in large corn fields where the plants are planted in relatively straight rows that are regularly spaced with a consistent number of plants in each row. This creates a somewhat periodic 2D lattice that can display similar features as a strict periodic lattice. One of these features is that the backscatter coefficient is not just a function of the incidence angle with respect to elevation, as is often observed with scattering from natural terrain, but it is also a function of the incidence angle with respect to the azimuth incidence. This feature can be identified from the circular crop fields in Fig. 3.23, which shows a SAR image of σ^0_{vv} taken by NASA's UAVSAR around July 2012 near the Rosamond dry lake in California, where illumination is coming from the bottom of the image. It is not known if these are corn fields, but assuming



(a) Floquet port excitation, PML termination.

(b) Floquet port excitation, impedance termination.

(c) Plane wave excitation, impedance termination.

Figure 3.22: 3D views of different simulation configurations to test replacing the Floquet port with a plane wave.

the plants in these fields are planted in concentric, circular rows, then the azimuthal incidence angle, with respect to the row direction, progresses from being parallel, to perpendicular, and back to parallel again when scanning across a field. It can be seen that the backscatter is indeed a function of the row direction with respect to the incident transmitted wave from the radar; it is brightest when the rows are perpendicular to the wave. Another example of this can be seen in Stiles et al., with respect to wheat fields [137]. The specific scattering behavior is strongly influenced by the spacing between plants in this case, and thus some simple analyses were carried out to characterize these effects.

3.5.1 Row and inter-plant spacing characteristics

The spacing between rows in corn fields is determined by the equipment used for cultivation. The most common row spacing is about 30 inches, or 76 cm. The nominal spacing between plants can

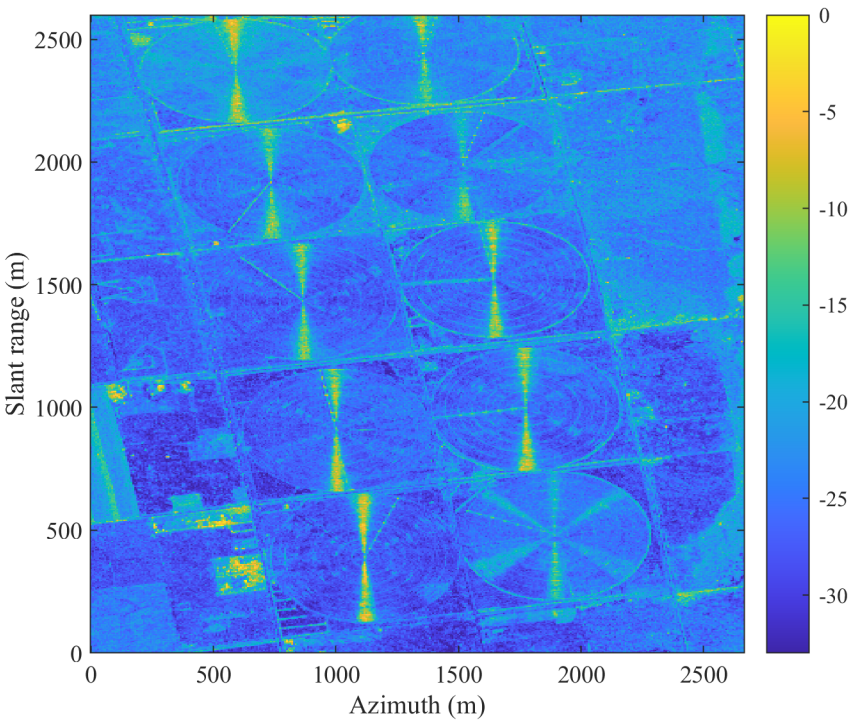


Figure 3.23: Calibrated σ^0_{vv} SAR image in dB taken by NASA's UAVSAR of circular agricultural fields near Rosamond dry lake, CA, using a slant-range projection, with illumination coming from the bottom of the image.

vary from 16-20 cm, and it has a larger variance. This can be ascertained from some websites such as R.L. Nielson of Purdue University [96] and also in-field samples. The inter-plant spacing was measured between 94 different plants in a corn field to provide an insight into the plant spacing. A histogram (in probability density) of the spacings between these plants can be seen in Fig. 3.24. The mean spacing is 17.5 cm, while the standard deviation is 6.5 cm. As can be seen, though, the distribution is not Gaussian. Much of the distribution resides between 12 and 20 cm, but a sizable portion also exists beyond 25 cm. That region exists because of gaps in the row where a seed did not get planted or none of the planted seeds grew. This distribution could be approximated with a shifted Rayleigh distribution. This type of distribution is also compared with the sampled spacings in Fig. 3.24. The shift amount and σ parameter of the Rayleigh distribution are provided in the legend.

When building a simulation of a corn field with 3D models of plants, each plant in the simulation

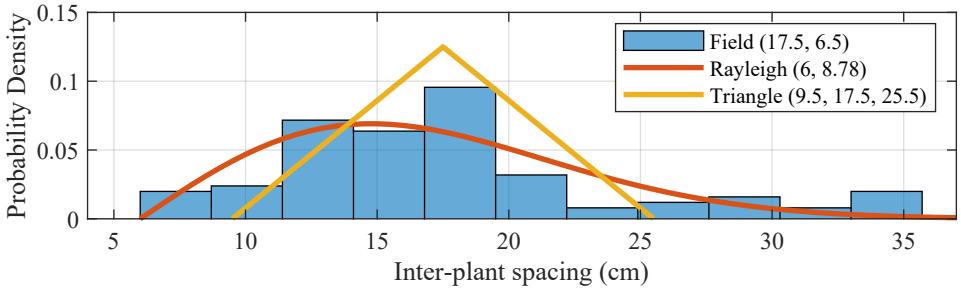


Figure 3.24: Sampled and potential spacing distributions.

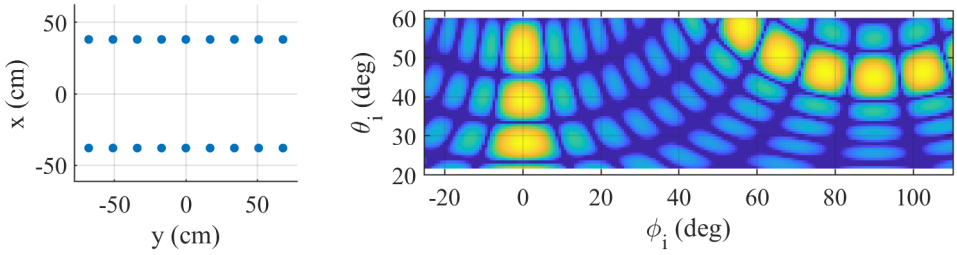
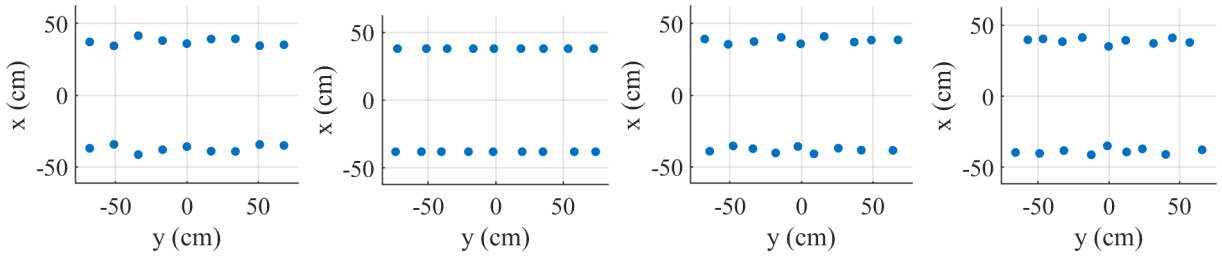


Figure 3.25: Point locations (left) and a heatmap (right) of the backscattered power from those points versus the incidence angle.

must have a location, and this is determined by the row and inter-plant spacing. Using an ideal spacing rule of something like 76×17 cm is perhaps not the best representation of reality. The spacing should be a little random. One way of doing this is to add a random offset with a uniform distribution to a plant's nominal location. Doing this causes the spacing between plants to have a triangular distribution. If a random offset of -4 to 4 cm is added to the plant's location along the row direction, which has a nominal 17.5 cm spacing, then the inter-plant spacing's distribution will look like the triangle function (the yellow curve) in Fig. 3.24, whose limits and mode are also given in the legend.

3.5.2 Effect of Plant Spacing on Backscatter

A simple analysis was performed to assess how the spacing between plants could affect the backscattering behavior. This was done by taking a finite group of points and, assuming plane wave illumination at 1.25 GHz, coherently adding the single-scattering reflections from each point. Each point represented a corn plant's location, and thus the nominal spacing between points was 76×17

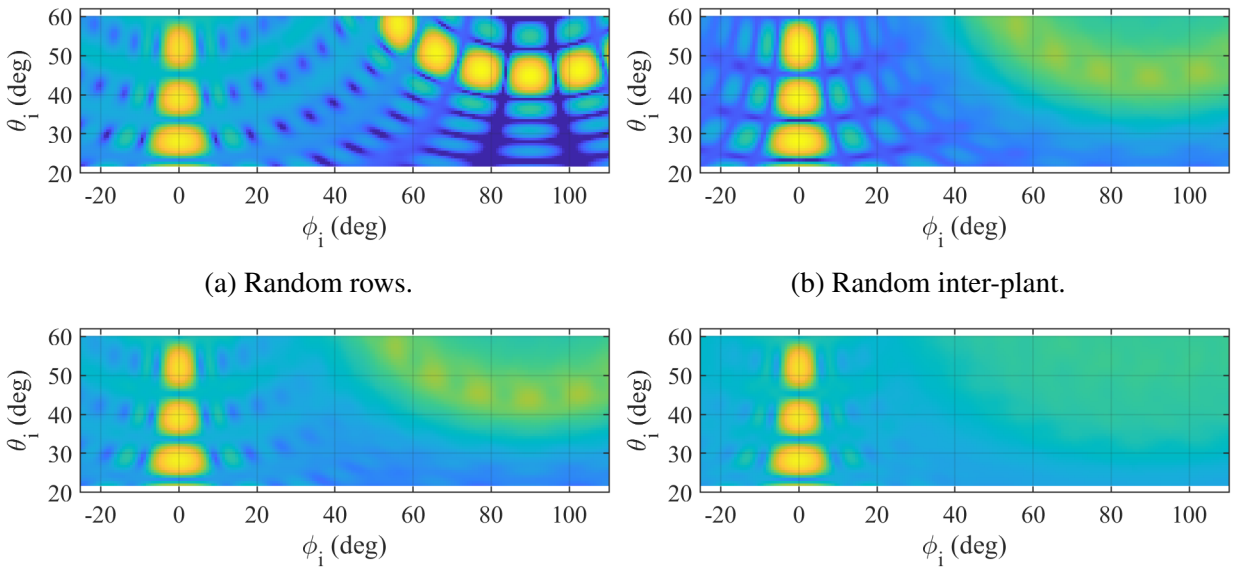


(a) Random rows. (b) Random inter-plant. (c) Both random. (d) Rayleigh inter-plant.

Figure 3.26: Illustration of point locations under different randomization schemes.

cm, and the group of points consisted of two rows with about 9 points per row. The total power from the sum of the reflections was then calculated for many incidence angles, both in ϕ_i and θ_i, so that a heatmap could be created that showed the angular distribution of the backscattered power. The result of this process for an ideal scenario with strict spacing between all points is shown in Fig. 3.25, where the left panel illustrates the point locations and the right panel shows a heatmap of the backscattered power versus incidence angle. The backscattered power is also normalized. The locations of the Bragg modes are evident at the bright spots along $\phi_i = 0°$ and the arc of bright spots near $\phi_i = 90°$. Sidelobes can also be seen, and the size or width of the bright spots depends on the spatial extent of the group of points for which this process was applied to. Using more locations (more rows and columns) would lead to narrower bright spots. This scenario highlights the angle-dependent scattering behavior of a periodic lattice and what could be expected from an ideally spaced field of plants. The goal of the analysis here, though, is to gain some insight into how randomized plant locations might affect the backscattered power's behavior versus incidence angle.

Thus, the process above was followed for four additional scenarios. The first scenario only randomized the points' spacing between rows by adding a uniform, random ± 4 cm to each point's x-location. One iteration of these locations can be seen in Fig. 3.26a. Additionally, the normalized backscatter was calculated and averaged over 1,000 random realizations of point locations. The results of this can be seen in Fig. 3.27a. Randomizing the row locations led to additional scattering near $\phi_i = 0°$ in the areas that would normally be nulls in the ideal case. The second scenario only



(a) Random rows.

(b) Random inter-plant.

(c) Both random.

(d) Rayleigh inter-plant.

Figure 3.27: Heatmaps of average, normalized backscattered power versus incidence angle for each of the location randomization schemes.

randomized the inter-plant spacing by adding a uniform, random ± 4 cm to each point's y-location. One iteration of this can be seen in Fig. 3.26b, and the backscattered power is shown in Fig. 3.27b. It can be seen that the arc of Bragg modes around $\phi_i = 90°$ almost becomes washed out entirely, and it appears that the average power has once again been spread over areas previously occupied by nulls in the ideal case. This can be seen more strongly for the third scenario, where both the row and inter-plant spacing are randomized by adding a uniform, random ± 4 cm to the x- and y-location of each point, and the points and their backscattered power are shown in Figs. 3.26c and 3.27c. The last scenario again randomizes the row locations with a uniform, random ± 4 cm offset, but the inter-plant spacing is determined by a shifted Rayleigh distribution with an offset of 6 cm and with $\sigma = 8.78$ cm. The point locations and average backscattered power can be seen in Figs. 3.26d and 3.27d. It can be seen that the Bragg modes along $\phi_i = 0°$ remain intact, the arc of Bragg modes around $\phi_i = 90°$ are completely washed out, and the few nulls still visible are shallow.

The main finding of this analysis is that non-uniform spacing between corn plants in a field can significantly affect the distribution of the average backscattered power with respect to the incidence

Table 3.2: Simulation parameters for the corn patch simulations associated with Fig. 3.28.

Parameter	Value
Center frequency	1.25 GHz
Unit cell size	184 x 182 cm
Realizations	5
Soil moisture	5%
Soil Clay %	7.1
Soil dielectric	$7 - j0.3$
RMS height	1.5 cm
Correlation length	10 cm
Correlation function	exponential

Parameter	Value
Average stalk height	82.3 cm
Average stalk width	2.1 cm
Row spacing	92 cm
Inter-plant spacing	13 cm
Stem moisture	94.7%
Stem dielectric	$49 - j14.7$
Leaf moisture	86.7%
Leaf dielectric	$42.1 - j12.8$
Leaf Z	$498 - j1594$

angle. It is also possible for the Bragg modes associated with parallel illumination of the rows to be completely wiped out. This indicates that the azimuth dependence of scatting from corn field could be classified into three regimes: backscatter from looking across or perpendicular to the rows, backscatter looking down or parallel to the rows, and backscatter from viewing the rows at an oblique angle. The backscatter may not be a strong function of the azimuth incidence in the latter two regimes. These characteristics may be borne out by the SAR image in Fig. 3.23, where for a few of the fields, the backscatter is strongest when the fields are viewed at a presumably perpendicular aspect relative to the row direction, and then relatively uniform outside of that.

3.5.3 Backscatter Behavior Versus Angle for a Small Patch of Plants

Finally, one last experiment was performed to better characterize the backscatter behavior of a corn field versus incidence angle. This experiment used HFSS to calculate the backscatter at many different incidence angles from a field of corn following the simulation methodology outlined summarized earlier in this chapter and explained in Chapter 4. Five different random realizations were used to estimate the average backscatter. Corn plants of medium size were used, and an example of these can be seen in Fig. 3.28. Several relevant parameters for the simulation are also given in Table 3.2. Unlike the previous analysis, the spacing between plants in this case was nominally 92×13 cm, and a unit cell size of 184×182 cm was used. The position of the plants was also randomized by adding a uniform random offset of $\pm$ 2 cm to the x-location (perpendicular

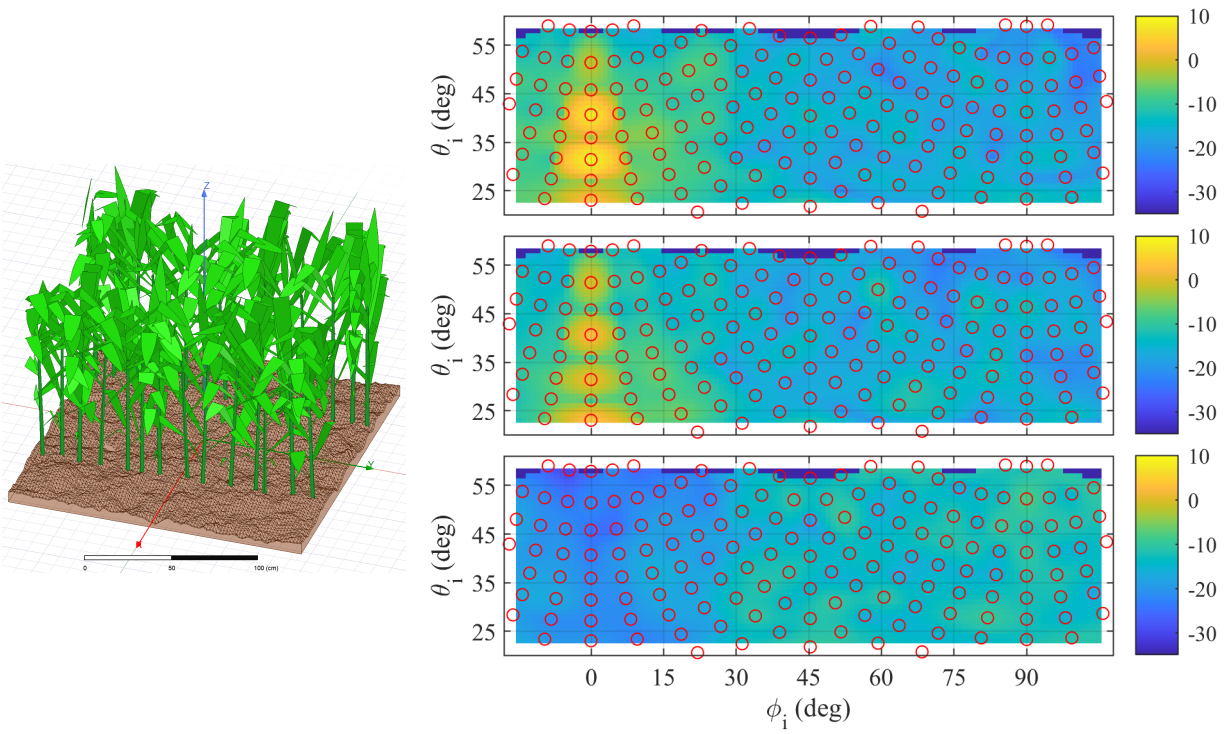


Figure 3.28: HFSS corn patch simulation model (left) and heat maps of the average backscatter (right) for σ^0_{vv}, σ^0_{hh}, and σ^0_{hv} in dB, going from top to bottom.

to the row) and $\pm$ 4 cm to the y-location (parallel to the row). The plant spacing in this case also changes the location of Bragg modes such that the arc of modes near $\phi_i = 90°$ in the previous analysis are not present. The Bragg mode at $\phi_i = 90°$ is near $\theta_i = 67.4°$ and would thus not be visible.

The results of these simulations are shown on the right side of Fig. 3.28 as heatmaps of the polarimetric backscattering coefficients σ^0_{vv}, σ^0_{hh}, and σ^0_{hv}, going from the top to the bottom. The Bragg angles associated with this size of unit cell are indicated by red circles on top of the heatmaps: with periodic boundaries, it's only possible to have a scattering component in the backscatter direction at these locations. The backscattering coefficients at other incidence angles were approximated by interpolation, using the "natural" interpolation method in MATLAB's `griddata` function. The Bragg modes present from the row spacing can be seen around $\phi_i = 0°$, with σ^0_{vv} generally being more prominent. The backscatter level between $30° \leq \phi_i \leq 105°$ is also relatively constant. It's interesting to note that there is not much cross-pol power at the Bragg

modes visible in the co-pol maps. The results again show that the backscatter can be quite strong when observing a corn field across its rows, and weaker but more consistent at oblique angles.

CHAPTER 4

Full-Wave Numerical Scattering Model for Corn

4.1 Introduction

Corn, or maize, is a widely grown crop around the world. Corn made up 28% of the harvested land in 2017 in the U.S. alone and had a market value of $51.2 billion [98]. Many experiments have used microwave radar to study corn fields to see if soil moisture (SM), vegetation water content (VWC), biomass, or growth stage can be measured [144, 61]. These parameters are important because of their roles in the water and carbon cycles, but they could also help growers employ efficient irrigation strategies and predict crop yield [149, 41, 20, 66]. Radar is generally a valuable sensor because of its ability to operate in most weather and lighting conditions. Radar on satellites like SMAP [38] or NISAR [160], whose launch date is under review at the time of this work's writing, also make it possible to globally monitor agricultural fields. Accurately estimating SM or growth stage requires a scattering model that links those quantities with the backscatter measured by a radar. Corn has historically been a difficult plant to model because of its large electrical size and dense, structured canopy.

In general, scattering models for corn can be classified into four types: coherent, single scattering theory (SST) models based on the distorted Born approximation [22, 89, 131, 146], incoherent methods using radiative transfer (RT) theory [131, 124], semi-empirical models [54, 78, 60, 12], and hybrid strategies that utilize results from numerical methods [106, 49]. Each of these models have their respective weaknesses and strengths.

Approaches based on SST and RT are computationally efficient because they use ideal canonical shapes that have analytical scattering solutions like cylinders and ellipsoidal disks to represent plant components like stems, branches, and leaves. They also typically ignore near-field multiple scattering effects. Single scattering theory and radiative transfer models differ from each other in that SST attempts to maintain coherent effects, while RT ignores phase and only calculates power transfer. Both methods also require a list of ancillary data to make realistic predictions. Semi-empirical methods are more straightforward to develop, but they can be difficult to generalize. Hybrid methods are newer and require more computer resources. They may also be more accurate than the other approaches because they use full-wave electromagnetic solvers such as the method of moments (MoM) or the finite element method (FEM) to compute scattering from one plant, or a part of one. Hybrid methods have only recently been explored, with SST and RT based approaches making up the majority of research efforts with regard to scattering from corn.

Ulaby and Bush [144] made early scatterometer measurements of corn. They used their results to make a semi-empirical model that correlated the radar backscatter coefficient σ^0 with a unique descriptor of plant development called the "normalized plant water content," but for frequencies between $8-18$ GHz. Ulaby also developed another simple model for the phase difference [146], which was later validated by Barber *et al.* [12] using SMAPVEX12 and ALOS-2 corn field scattering data. Based on that model, Barber *et al.* showed that the phase difference is most sensitive to the stalk height and the angle of incidence.

Several works highlight the importance of accurately representing the geometry of a scatterer (corn plant) with the fundamental scattering elements used in the model. The Michigan microwave canopy scattering model (MIMICS) was an early effort to model radar backscatter by representing the geometry of forests more accurately than its predecessors [147]. Sarabandi et al. [124] also developed an early model for predicting wave transmission through a corn canopy by using an ABCD matrix approach and restricting the analysis to a 2D scattering scenario. Their model agreed well with measured data for vertical polarization, but not horizontal polarization due to the incorrect orientation of the leaf elements in the model. Another early SST-based model was created

by Chuahan et al. [22]. They made detailed measurements of plant components like stalk and leaf sizes to use as inputs to calculate the average scattering. Their results indicated sensitivity to the model's representation of the stalk, and they suggested that a refinement of it may be necessary. Although they did not work with corn, Lin et al. [73] developed a coherent scattering model for trees that was also based on SST, and it used a unique tree architecture generator based on fractal Lindenmayer systems. They found the structure had a significant effect on the extinction and scattering profiles of the generated trees.

More recent work by Monsivais-Huertero et al. [89] also shows that the geometrical representation of a corn plant is important. They attempted to reflect a corn plant's changing structure over the course of a growing season. The growth was accounted for using a generative algorithm that modified individual scatterers appropriately according to the time of the growing season. The algorithm also put vegetation scatterers in a periodic arrangement in accordance with the row-structure. The model was validated against data from a ground-based L-band scatterometer. Their results showed improved accuracy over a model with randomly-placed scattering elements.

Researchers have also found that multiple scattering effects can be significant for scattering from vegetation. Sarabandi et al. [122] used dielectric cylinders to represent a stalk canopy and applied analytical methods for calculating interactions between adjacent stalks up to 2nd order without appealing to SST, which were used in a Monte-Carlo simulation and RT approach. They verified that the RT approach was not accurate outside of its region of validity, such as when the medium is dense and near-field interactions become important, which is true for corn. Additionally, Oh *et al.* created a model that could be used for scattering from rice fields [100]. They used an impedance surface to represent the ground that allowed them to obtain the exact half-space Green's function. The problem could then be solved using the method of moments (MoM). They found that the cross-polarized backscatter is significantly influenced by multiple scattering.

Soil roughness is another important feature that studies seek to account for. Chiu *et al.* [26] developed an SST-based model for soybeans and included interactions between stems and a rough soil layer. They compared their simulation with measured data at L-band and C-band. They found

that the stem and rough soil interaction could significantly impact the cross polarization scattering at L-band.

Many investigations indicate that the azimuthal incidence angle is important for scattering from vegetation with row structure, as is seen for many agricultural crops. Stiles *et al.* [135] formulated a model for scattering from grasslands that used SST, accounted for the non-uniform illumination of plant components, and addressed periodic rows of grasses that can be found for cultivated plants like wheat. Their model and experimental data [137] showed that the backscatter is significantly affected by the illumination angle with respect to the row direction. More recently, Sharma et al. [131] investigated corn backscatter at L-band over a growing season using ground-truth data and two models: one based on SST, and a second based on RT. They used a ground-based scatterometer that scanned across a field from -60° to 60° to collect experimental data, where 0° looked across the rows. They found that the backscatter from azimuth incidence angles less than $\pm 16°$ was significantly stronger than from the other angles. Bouchat et al. [17] also observed different values of σ^0 from corn when viewing it across and parallel to the rows.

It is perhaps no coincidence that SST- and RT-based scattering models are prevalent and well-developed. For early researchers, computationally efficient models were desirable because of the relatively limited computing resources available. Since then, computing technology has progressed enormously, and the prevalence and capability of high performance computing (HPC) systems has been spurred on by applications like machine learning (ML). The current wealth of computing resources provides today's researchers the opportunity to investigate vegetation scattering models with numerical methods.

Some of the most recent work with numerical methods has been conducted by Gu et al. [49]. Their approached used a two-step method, where in the first step, the T-matrix of a single plant was derived using results from a full-wave numerical solver. In the second step, multiple scattering effects were accounted for with the calculated T-matrices and with the Foldy-Lax multiple scattering equations. The approach was applied to wheat plants, and the results showed good agreement with large full-wave simulations. Applying the same approach to corn may not be straightforward

because of overlap between plants in a corn field. Adaptations of the approach for corn have been investigated [45].

The current research on radar scattering models for corn and vegetation make it apparent that a good model for corn ought to include an accurate representation of the plant's geometry, account for multiple scattering effects, be able to incorporate a rough-soil surface, and handle the periodicity present in a corn canopy.

The goal of this work is to present a method for accurately predicting backscatter from corn that is based on a full-wave electromagnetic solver. Recent advancements and easier access to high performance computing (HPC) may alleviate the high computational cost of this approach. Ideally, the simulation should be able to (1) faithfully represent the plant's geometry, (2) accurately account for interactions among plant constituents and other adjacent plants, (3) account for interactions between the plants and the soil surface, and (4) reflect the row structure of the canopy. The novelty of the proposed method lies in the fact that it is a computationally tractable full-wave simulation that uses accurate, data-based 3D models to represent the vegetation's structure. A high-fidelity simulation like the one presented here will lead to an increased understanding of corn's scattering characteristics. This work utilizes real-world synthetic aperture radar (SAR) data to validate the simulation's accuracy.

This work is organized as follows. The next section describes how the model works and some of its limitations. The third gives an overview of the SAR dataset that was used for validation. The fourth compares predictions of the radar backscatter coefficient with SAR data and an SST-based model to evaluate the simulation. The fifth section discusses some of the results from that comparison, while the sixth section draws conclusions with suggestions for future research.

4.2 Scattering Model Description

The scattering simulation for a corn field has two major parts: 3D CAD models of corn plants and an FEM-based electromagnetic solver. We used the commercially available ANSYS HFSS for the

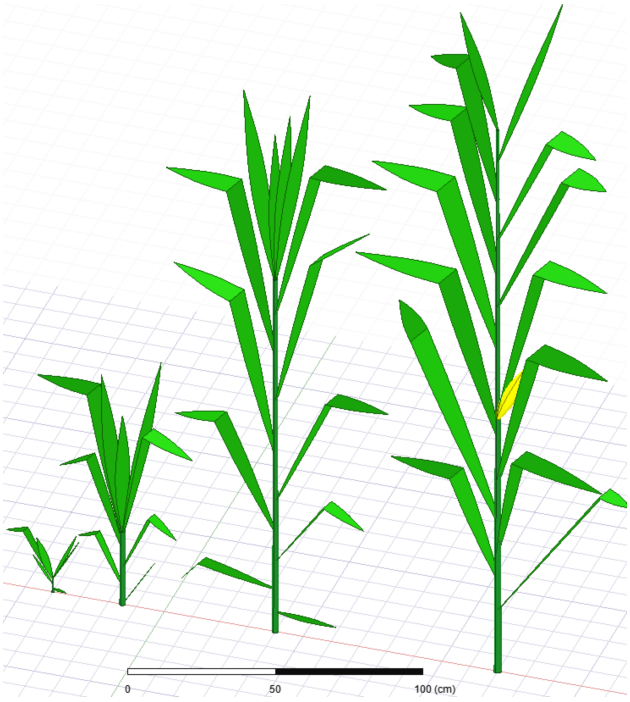


Figure 4.1: Samples of corn plant geometries based on field measurements for four growth stages.

electromagnetic solver.

4.2.1 Plant 3D CAD Model

The University of Florida collected geometrical information from corn plant samples in 2016 and 2018 at Citra, Florida in order to create realistic 3D plant models. These measurement efforts were also carried out in connection with the Delft University of Technology. They were done by taking plant samples from a corn field throughout the growing season and making measurements of their geometry. For each plant sample, they measured the following quantities: stem height, stem circumference at the top and bottom of the plant, leaf starting height, leaf length, leaf width, angle between the stem and leaf, angle of the leaf tip, ear starting height, ear length, ear maximum circumference, and the angle between the stem and the ear.

Based on these measurements, they developed a computer program which can automatically generate corn plant CAD models. The program can use the measurements from 2016 and 2018 as inputs to generate 3D CAD models for each plant. An example of what individual plants look like

can be seen in Fig. 4.1. These 3D CAD models represent the more substantial components of a corn plant. Plant components like tassels, nodes, internodes, and ear husks are not included in the plant's geometry because their effect would likely be small and would unnecessarily increase the computational cost. These data-based CAD models provide the starting point for calculating the radar backscatter from a corn field.

4.2.2 Electromagnetic Analysis

The programmatically generated plant CAD models are electrically analyzed via FEM in HFSS. An overview of the simulation configuration can be seen in Fig. 4.2. The size of the computational domain is large compared to the illuminating wavelength, and it is also large enough to include a couple rows of plants in order to capture some of the randomness present in a corn field. Periodic boundary conditions are applied to the front, back, left, and right boundaries of the computational domain. This type of boundary effectively replicates the structure inside the unit cell to create an infinite periodic structure. This was done to (1) limit the size of the computational domain, (2) to include multiple-scattering effects among plant constituents and adjacent plants, and (3) to avoid edge diffraction effects, which exist in simulations with a finite ground-plane. The top of the domain is terminated by a perfectly matched layer (PML) to absorb scattered energy. A dielectric slab, which can be given a rough top surface, represents the soil layer and is located below the plant canopy to account for soil-plant interactions. The bottom of the soil layer was originally terminated with another PML, but simulation results showed a significant reflection at the soil-PML boundary. To address this issue, the bottom of the computational domain is assigned an impedance boundary, which results in only a very small reflection from the bottom of the domain.

The simulation is also configured so that the structure is excited by a plane wave. This excitation requires that the scan direction, or phase delay, between periodic boundaries matches the propagation delay of the incident wave. An iterative solver was chosen for the matrix inversion due to the sparse nature of the FEM stiffness matrix. The delta energy convergence criteria used for the adaptive meshing was set to 0.025 J/J, which is higher than a preferred value of 0.008

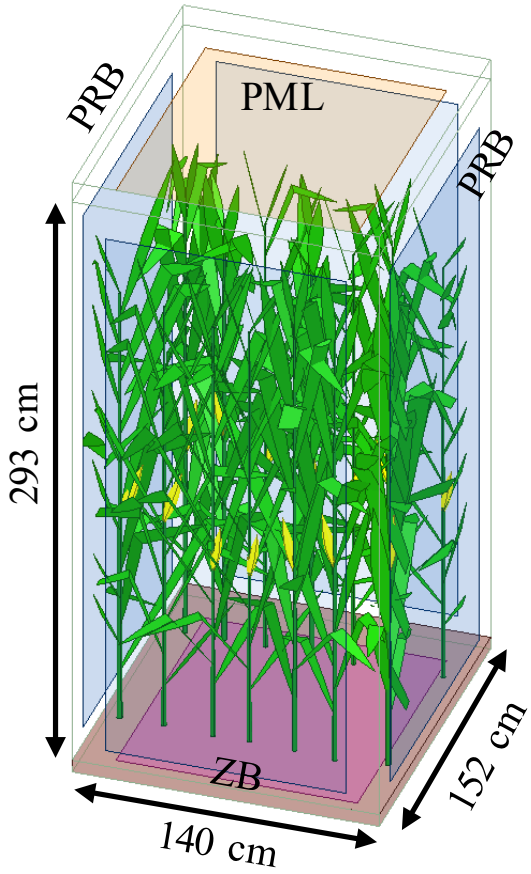


Figure 4.2: 3D view of the electromagnetic simulation. Periodic boundaries (PRB) are applied to the left, right, front, and back sides of the simulation domain. A PML boundary is used on the top, while an impedance boundary (ZB) is used on the bottom of the soil layer. The soil layer is a dielectric material that is shown in brown near the bottom.

J/J. This was done to reduce the computation cost and only had a small effect on the convergence of the results. The large electrical size of the simulation domain produces a large mesh, which is susceptible to dispersion errors. However, HFSS uses tetrahedral finite elements that have been shown by Wu *et al.* to exhibit lower dispersion errors because of phase error cancellation [156]. Based on the findings from Wu *et al.*, the maximum phase error of simulations in this work may be below 5°.

Predictions of the backscatter coefficient σ^0 are produced by setting up the plant geometry with the correct material parameters and simulating it at an appropriate incidence angle. This is done for multiple random realizations of plant geometry, which is explained more below. The monostatic

radar cross-section (RCS) is then calculated using the scattered fields from the top surface of the computational domain. The ensemble average of the calculated RCSs from each realization is then divided by the area of the unit cell to produce an estimate of σ^0.

The simulation configuration described above with the data-based 3D plant models is the main contribution of this work. While the configuration is not complicated, it is also not obvious. There were a few issues that had to be addressed such as including soil interactions, how many plants to include while keeping the computational cost down, and how large of a period should be considered with the periodic boundaries. The answers to these issues are not obvious, and thus the simulation configuration is a novel, balanced solution.

4.2.2.1 Implications of Periodic Boundaries

Using periodic boundaries in HFSS means that the field distributions on corresponding sides of the computational domain will have the same magnitude, but different phases. For example, the left and right sides of the computational domain are parallel to the xz-plane. If the electric fields on these sides are considered, then the periodic boundary condition is

$$\vec{E}_{right}(x, y_0 + L_y, z) = \vec{E}_{left}(x, y_0, z)e^{-j\phi}, \tag{4.1}$$

where ϕ is an additional phase factor and L_y is the unit cell's length along the y-axis. HFSS allows this phase factor to be specified. For incident-wave simulations, it is the same as the phase delay of the incident wave traveling across the unit cell. Thus, if the incident wavevector is $\vec{k} = (k_x, k_y, k_z)$, then $\phi = k_y L_y$.

With periodic boundaries, the simulation configuration will essentially calculate the scatter from a 2D periodic surface made up of the unit cell. Scattering from such a surface is made up of a discrete angular spectrum of plane waves whose wave vector components are given by

$$k_{xmn} = k_{0x} + \frac{2\pi m}{L_x} \tag{4.2}$$

$$k_{ymn} = k_{0y} + \frac{2\pi n}{L_y} \tag{4.3}$$

$$k_{zmn} = \sqrt{k_0^2 - k_{xmn}^2 - k_{ymn}^2}, \tag{4.4}$$

where a rectangular lattice is assumed, k_{0x} and k_{0y} are the transverse components of the incident wave, m and n are integers, and L_x is the length of the unit cell along the x-axis. A scattered plane wave is evanescent if k_{zmn} is purely imaginary.

Backscatter from a 2D lattice only occurs for specific incidence angles or Bragg modes given by

$$\theta_i = \arcsin\left(\frac{\lambda}{2}\sqrt{\left(\frac{m}{L_x}\right)^2 + \left(\frac{n}{L_y}\right)^2}\right) \tag{4.5}$$

$$\phi_i = \arctan\left(\frac{nL_x}{mL_y}\right), \tag{4.6}$$

where λ is the free space wavelength. Ideally, we would like to obtain backscatter estimates for arbitrary incidence angles. To help accommodate that, the number of possible scattering angles can be increased by increasing the size of the simulation domain or unit cell. This allows the backscatter to be calculated at a large number of angles, and perhaps interpolated for non-Bragg incidence angles.

4.2.2.2 Plant Component Representation and Material

The plant geometry has three primary components: a stem, leaves, and one or two ears. The stem is represented with a dielectric circular frustum, the ears with dielectric ogives, and the leaves are simply represented as resistive sheets. Electromagnetically, the leaves are replaced with impedance

boundaries. This simplifies the computation by reducing the size of the mesh needed for the simulation. It is an approximation that is justified because leaves are often very thin (about 200 μm) with respect to the wavelength ($\sim$24 cm at 1.25 GHz). Senior et al. [129] and Sarabandi [116, p. 310] have also demonstrated that using an impedance-surface to model scattering from leaves agrees well with real-world measurements. Their formulation was used with an $e^{j\omega t}$ time convention to calculate the appropriate impedance based on the leaf's permittivity and thickness:

$$Z_{sheet} = \frac{-j\eta_0}{k_0\tau(\epsilon_r - 1)}. \tag{4.7}$$

Here, η_0 is the free space impedance, k_0 the free space wavenumber, τ the leaf thickness, and ϵ_r the relative permittivity. The dielectric constant of the leaves, stem, and ears were determined using the relationship developed by Ulaby et al. [145], which relates the gravimetric moisture content m_g to the dielectric constant.

The structure of each plant is defined by the programmatically generated CAD models that are in turn based on measurements taken from real plants. However, the placement of a plant and its orientation in the simulation can be specified. Because of this, we applied a uniformly distributed random tilt with respect to the vertical axis of $\pm 2^\circ$ or $\pm 3^\circ$ to each plant in a random direction between 0° and 360°, along with a uniformly distributed random rotation of the plant between 0° and 360°. The physical location of the plant in the simulation was also randomized with respect to the nominal spacing between plants. Corn plants are typically planted with 20 cm between plants and 76 cm between rows. The plant locations were randomized by putting plants at their nominal locations determined by the spacing and then adding a uniformly distributed random offset of ± 2 cm to the plant's location across rows, and ± 4 cm to its location along a row. Additionally, there are typically several different CAD models of the plant to choose from for one stage of growth. The CAD model was also randomized with respect to which CAD model was used at each plant location among the available models for one growth stage. This randomization process is important for creating independent realizations of the plant structure used in the simulation, while keeping

the material permittivities constant.

4.2.2.3 Soil Representation and Material

The soil layer was represented with a dielectric substrate, which is the brown portion of the simulation structure seen in Fig. 4.2. The soil can be given a rough profile to model the rough soils typically seen in agricultural fields. The dielectric constant of the soil layer was estimated using the model from Mironov *et al.* [86] that relates volumetric moisture m_v to dielectric constant. It was assumed that soil moisture was constant as a function of depth, which is reasonable as long as the moisture profile is continuous [120].

4.2.2.4 Balancing Model Computational Cost and Accuracy

Because of this model's high computational cost, it is important to quantify the relationship between computer resources and accuracy in the estimated backscatter. We analyze this relationship by assessing how many simulation realizations are needed to achieve a specified tolerance around the backscatter estimate, such as ± 2 dB. Put more formally, we want the sample average Z_n to be within ϵ of the true average μ with probability p. Additionally, if ϵ is specified in dB, then the inequality

$$P(\mu 10^{-\epsilon/10} \leq Z_n \leq \mu 10^{\epsilon/10}) \geq p \tag{4.8}$$

could be used to help determine the number of realizations or samples N needed to achieve the required tolerance.

We assume that a backscatter estimate produced by the simulation can be modeled as an exponentially distributed random variable. This is a reasonable assumption for scattering from generally uniform natural targets like corn fields (see [76], pg. 177). Averaging N exponentially distributed random variables produces a χ^2 distribution with $2N$ degrees of freedom. We use the following form of the χ^2 probability distribution function (PDF)

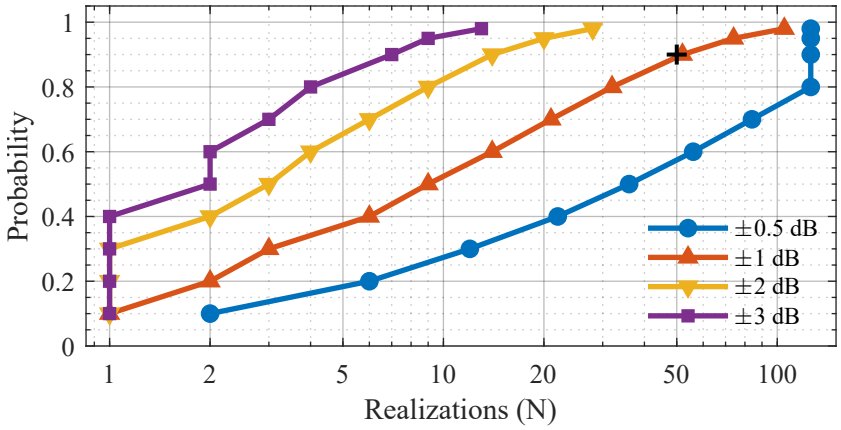


Figure 4.3: Level curves relating number of realizations, error interval, and confidence level (probability). The black marker indicates what was used in this study.

$$f_X(x, N) = \frac{x^{N-1} N^N e^{-Nx}}{\Gamma(N)} \tag{4.9}$$

to characterize the sample average's distribution. Curves can be calculated that relate the number of realizations N, the confidence level p, and the error interval ϵ. Several of these curves are shown in Fig. 4.3.

From those curves, it can be seen that a 90% confidence interval of ± 1 dB can be achieved with 50 simulation realizations. Fifty realizations were used in this study.

4.3 Study Site

This work leverages data from the Soil Moisture Active Passive Validation Experiment of 2012 (SMAPVEX12) in order to evaluate the accuracy of the proposed scattering model. The SMAPVEX12 experimental campaign was conducted to acquire active and passive microwave observations over a long period of time to facilitate soil moisture retrieval algorithms for the SMAP satellite [84]. The campaign's survey area included agricultural and forested regions near Manitoba, Canada. The survey area is outlined in the left panel of Fig. 4.4. Calibrated measurements of σ^0 were collected during the campaign by NASA's UAVSAR, which is an aircraft-based, fully polarimetric L-band ($f_0 = 1.26$ GHz) SAR. Many different kinds of measurements were also per-

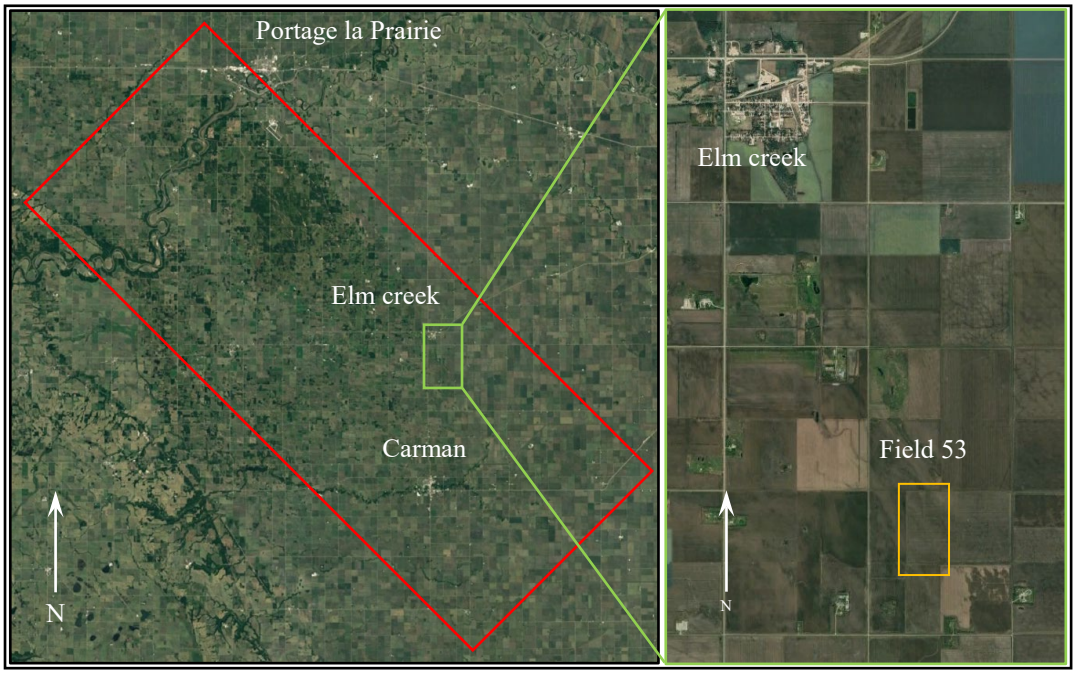
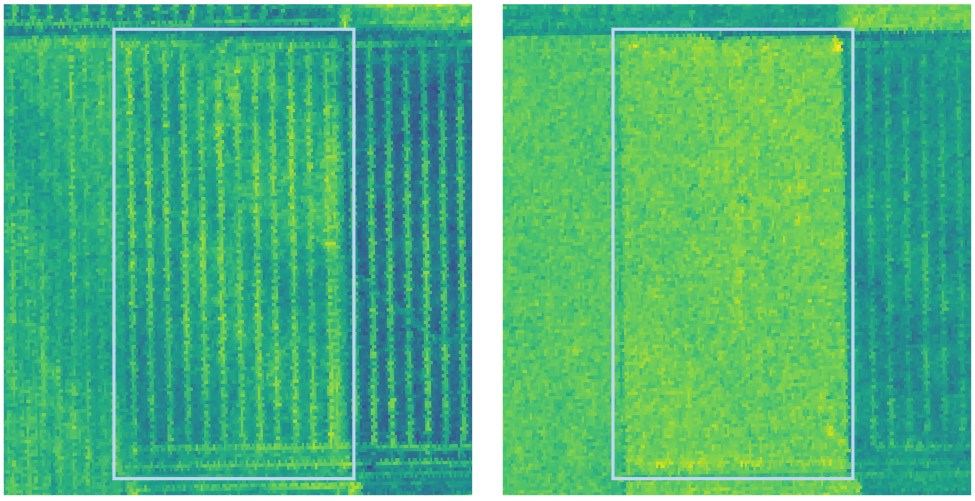


Figure 4.4: Satellite image of the SMAPVEX12 experiment region in Manitoba, Canada [33]. The total area imaged by UAVSAR is shown in red on the left panel. The right panel is a closeup of corn field 53, which is used for validation in this study.

formed throughout the survey area. Relevant ancillary measurements for this work include soil moisture, crop type, plant gravimetric moisture content, stalk height and diameter, soil texture, soil roughness, and crop row direction. All observed data (both ancillary and radar) used in this study come from a corn field with the field identifier 53. This corn field is outlined in the right panel of Fig. 4.4.

The UAVSAR made four consecutive passes over the experiment area on each day that it flew to gather data. It traveled in a north-west direction on each pass so that the imaged terrain would be on the left of the aircraft (see Fig. 4.4). The flight lines were offset from each other so that each pass imaged the same area at different incidence angles. This multi-pass data was used to create incidence-angle normalized data following a novel method in [87]. However, only SAR data from one pass was used in this study. The pass was chosen such that the SAR illuminated field 53 at an incidence angle of $\sim$40°. SAR images of σ^0_{vv} for field 53 are shown in Fig. 4.5. The row features visible on DoY 169 are spaced about 120 ft apart, and are likely due to tractor tracks. For that day,



(a) DoY 169 (b) DoY 199

Figure 4.5: SAR images of σ^0_{vv} of field 53, which is highlighted in blue. Row-like features for early-season corn (169) are likely tractor tracks.

only pixels between the tracks were used for comparison with the model.

The ancillary data for corn field 53 includes several measurements that are shown in Fig. 4.6. The stalk height and average biomass make up the top two panels. Unsurprisingly, those panels show how the plant's height corresponds with biomass, and it is also apparent that water makes up the bulk of the vegetation's weight. The gravimetric moisture level of different plant components is shown in the third panel from the top. They remain relatively constant over time, with only some slight drying later in the season. Soil moisture is in the bottom panel and shows the average soil moisture with ± 1 standard deviation (shaded area). It can be seen that the soil starts out relatively moist and then dries out as the season progresses. Finally, the rows in field 53 were oriented north to south.

The soil roughness was measured with a pinprofilometer to characterize the soil structure at the beginning of the season on June 13. The RMS height and correlation length of the soil in field 53 were estimated to be 1.26 cm and 11 cm, respectively. Agricultural fields in this area generally relied on rain irrigation for water. Thus, irrigation furrows are not required, and were not likely to be a feature of the soil profile.

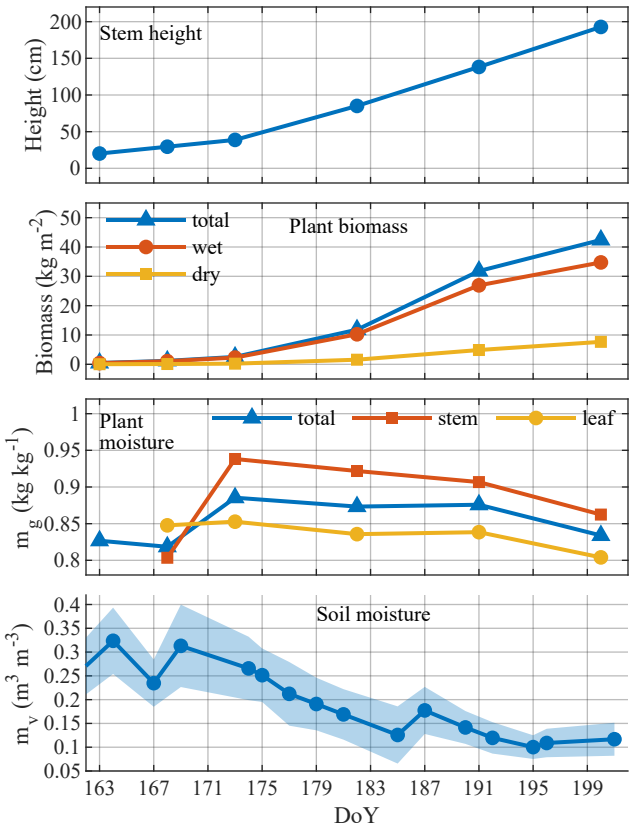


Figure 4.6: Averaged ancillary data from field 53 over time. From top to bottom: stem height, plant biomass weight, gravimetric moisture content of plant components, and soil volumetric moisture content.

4.4 Model Validation

Radar data from SMAPVEX12 was used to validate the predictions of the scattering model. It is important to match the model's input parameters (plant geometry, moisture levels, etc.) to the *in situ* field conditions. The SMAPVEX12 ancillary data helps tremendously in this regard. The measured stalk heights and circumferences from SMAPVEX12 were used to modify the original stalk geometry data from the University of Florida to create 12 unique plant CAD models for each growth stage used for validation, where the growth stages were matched by comparing stalk heights. However, some characteristics were not recorded. These include any tilt of the stalk from vertical and the specific leaf structure. Thus, the original leaf structure from the University of Florida's data was used in these models. Two days from the experimental campaign were selected

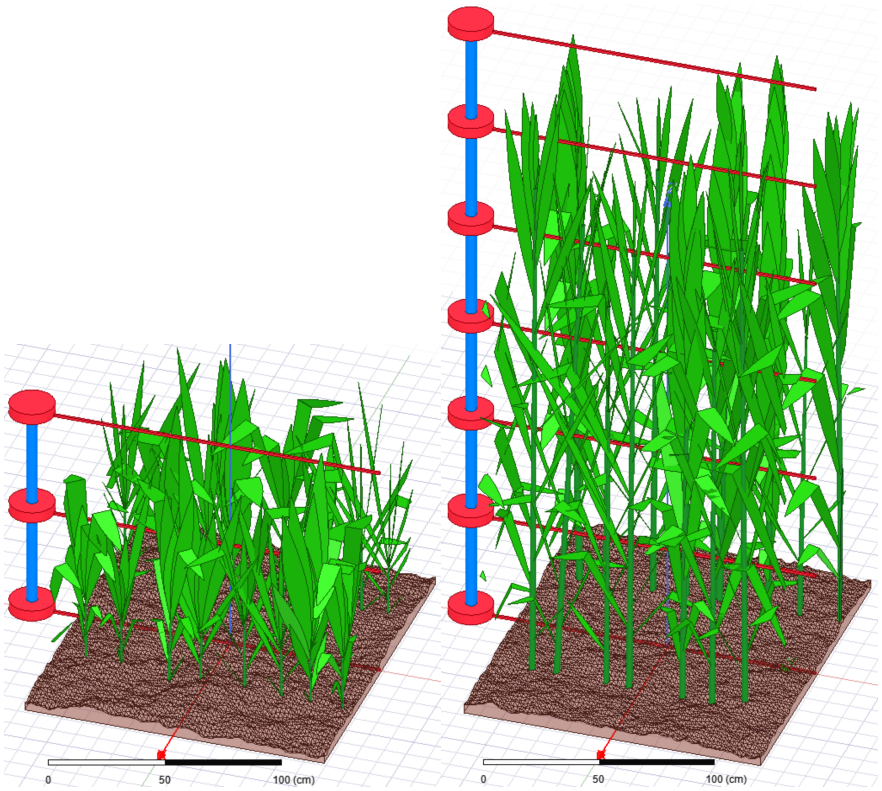


Figure 4.7: A single simulation realization from DoY 169 and 199, going from left to right. Each simulation is one of 50 total random realizations. The red disks are 10 cm thick, 20 cm wide, and spaced 50 cm apart and are only included for scale.

for comparison to evaluate the ability of the model to predict backscatter. They were chosen to predict the backscatter from small and mature, but not yet fruiting, plants. The specific days that were used were June 17 and July 17, 2012, or the 169^{th} and 199^{th} days of the year (DoY). Again, the plant and soil material properties in the HFSS simulations were determined using [145] and [86].

Table 4.1 shows the nominal corn plant parameters that were used to set the material permittivities and plant geometry. The table also shows the permittivity that was used for each material in the simulation. The soil moisture level for DoY 199 was not known because there was no soil moisture measurement on that day. It was likely somewhere between 0.07 and 0.18 because there was rain the day before. To address this unknown, an iterative process was used that executed the HFSS simulations for that day with different soil moisture values until good agreement was at-

Table 4.1: Model input parameters.

DoY	169	199
$m_{g,stalk}$	0.804	0.862
$m_{g,leaves}$	0.848	0.804
$m_{v,soil}$	0.21 – 0.27	0.07 – 0.18
Clay %	29.1	29.1
h_{stalk}	29.5 cm	200 cm
d_{stalk}	1.17 cm	2.27 cm
$\epsilon_{r,stalk}$	$37.1 - 11.5j$	$41.7 - 12.7j$
$\epsilon_{r,leaves}$	$40.5 - 12.4j$	$37 - 11.5j$
$\epsilon_{r,soil}$	$17.5 - 2.4j$	$7.1 - 0.8j$
Stalk tilt	$\pm 2°$	$\pm 3°$
h_{rms}	1.26 cm	1.2 cm
l_{corr}	11 cm	13 cm

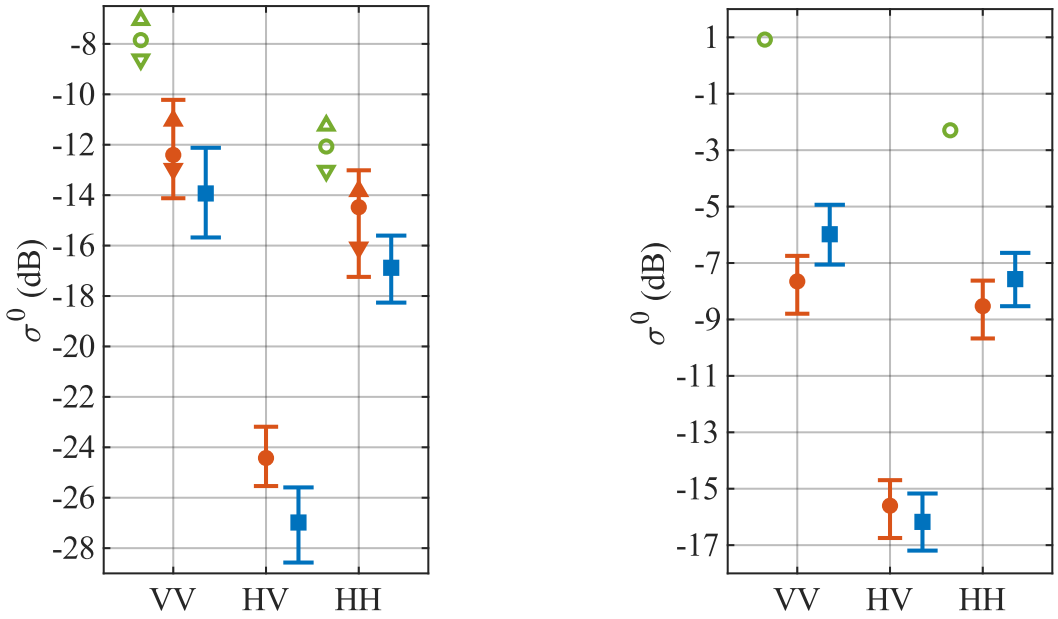
Table 4.2: Simulation input parameters for the DoY 169 variations indicated by the markers.

	m_v	h_{rms}	l_{corr}
▲	0.27	1.26	11
●	0.23	1.26	11
▼	0.21	1.2	13

tained, and that value was 0.16. The experimental campaign ended just as tassels started to emerge on the plants, so no plant had ears during the UAVSAR flights. The geometric plant structure used for each day is illustrated in Fig. 4.7. The unit cell size for all of the simulations was 152 x 136 cm, with an average plant spacing of 17 cm for plants in the same row, and 76 cm between rows. A rough soil profile was also used in the simulations that was parameterized by the RMS height (h_{rms}), correlation length (l_{corr}), and an exponential correlation function. The roughness parameters were made slightly smoother on DoY 199 to account for erosion. The model was also solved at $f_0 = 1.25$ GHz.

4.4.1 Comparison of Models Against SAR Measurement

It is reasonable to directly compare the results from HFSS with the SAR data since they each had roughly the same incidence angle. Field 53 was illuminated at $\phi_i \approx -45°$ and $\theta_i = 42°$, where $\phi = 0°$ corresponds to north and $\phi = 90°$ corresponds to west. The HFSS simulations were



(a) DoY 169 (b) DoY 199

Figure 4.8: Simulated σ^0 (red, filled markers) compared with σ^0 data from UAVSAR for field 53 (blue squares) and SST predictions (green, unfilled markers). Whiskers around the red markers indicate the 90% confidence interval as defined by (4.8), while circles show the mean value. Whiskers on the blue markers indicate the 1st and 3rd quartiles of the SAR data, while the circles indicate the median.

executed at an incidence angle of $\phi_i = 42.965°$ and $\theta_i = 40.306°$, which is a backscatter Bragg mode. The predictions of the SST-based model were obtained following the approach of Sharma *et al.* [131], with several modifications that are detailed in Appendix A.

Figure 4.8 compares the predictions from the SST-based model, the proposed model, and the SAR data shown in open green markers, filled red markers, and filled blue, square markers, respectively. The upwards triangle, circle, and downwards triangle markers represent different sets of input parameters for DoY 169 and are given in Table 4.2. This was done to show the possible variation in backscatter values because of natural variation in each of the input parameters. For DoY 169, there is good agreement between the third set of inputs (downward triangles) of the proposed model and the measured SAR data, except for the cross-pol, which is overestimated. There is also good agreement for DoY 199, with σ^0_{vv} being underestimated. All predictions from the SST model overestimate the backscatter by at least 5 dB for all polarizations.

Table 4.3: Computation statistics of a single realization.

DoY	169	199
Median RAM (GB)	20.6	44.6
Max RAM (GB)	28.3	57.2
Median Time (hr)	1.2	4.3
Max Time (hr)	2.4	4.8

4.4.2 Computation Performance

The simulations were executed on the Great Lakes high performance computing (HPC) system at the University of Michigan. The computation statistics for each day of comparison are summarized in Table 4.3. Each realization was solved at one incidence for both vertical and horizontal incident polarizations. The mesh generated for vertical incidence was reused in the horizontal incidence simulation to speed up simulation time.

4.4.3 Backscatter Sensitivity to Soil Moisture and Vegetation Water Content

The simulation was also used to see how sensitive the backscatter may be to SM and VWC by varying the dielectric constant of the soil and plant components. This was also done for the two different growth stages that were used for validation.

The results of sweeping SM and VWC (via the moisture content of the plant components) are shown in Fig. 4.9. The top panels show the backscatter from the small plants, while the bottom panels show the same for the mature plants. At least 15 realizations were solved for each growth stage and moisture level. A flat soil was used in these simulations except for the soil moisture sweep for DoY 169, which was done with a rough soil since its impact would be more pronounced. The shaded areas show the 90% confidence interval. The results used for validation are also included, and can be seen at $m_g \approx 0.82$ and $m_v \approx 0.21$ for DoY 169, and $m_g \approx 0.82$ and $m_v \approx 0.16$ for DoY 199.

It can be seen that the backscatter for both stages increases with SM, except for the last point of the HH polarization for DoY 199. For DoY 169, the backscatter changes by 4.2 dB for VV, 3.0 dB

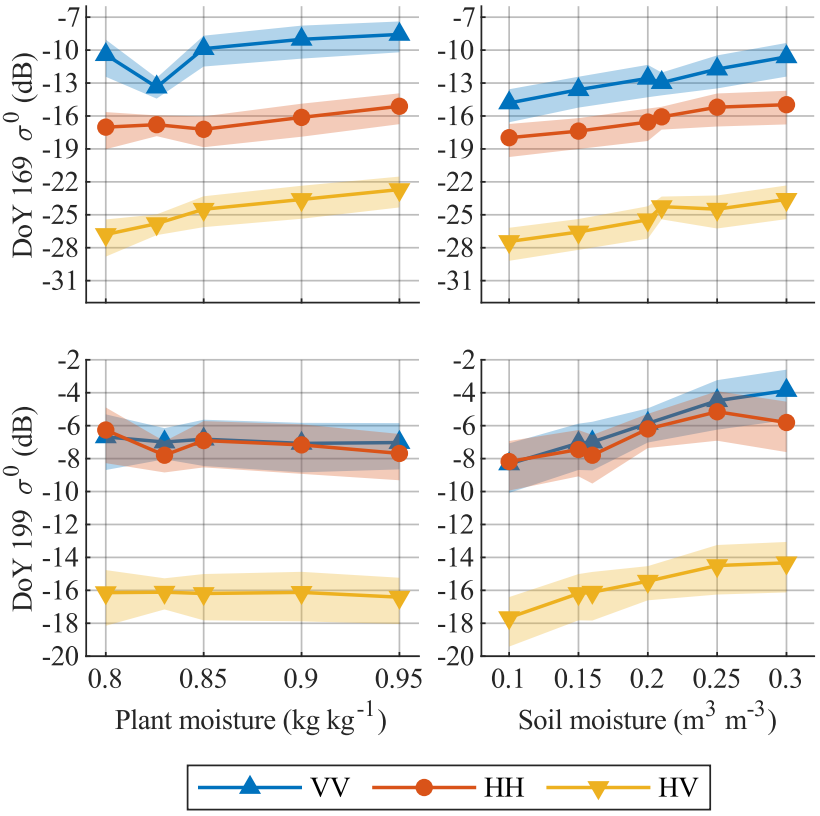


Figure 4.9: Average backscatter from sweeping SM and VWC for the early and mature growth stages. Again, the shaded areas show the 90% confidence interval, where at least 15 realizations were computed for each sweep point.

for HH, and 3.8 dB for HV as m_v changes from 0.1 to 0.3. For DoY 199, the backscatter changes by 4.3 dB for VV, 2.4 dB for HH, and 3.3 dB for HV over the same range of m_v. This shows that the backscatter from a mature corn field is somewhat less sensitive to SM than one with small plants. For simplicity in changing the VWC, the gravimetric moisture content (m_g) was made the same for all plant components, which significantly increased the VV scattering for DoY 169 from its nominal value. These results can be seen in the panels on the left-side. For DoY 169, both VV and HH increase by 1.9 dB, while HV increases by 4.1 dB as m_g increases from 0.8 to 0.95. However, there is virtually no change in backscatter for DoY 199, except for the HH polarization that decreases by 1.4 dB.

4.5 Discussion

Other studies have also shown similar qualitative trends in the sensitivity of backscatter to soil and plant moisture as predicted by the simulation results given in Fig. 4.9. For instance, the observations from Chauhan *et al.* show a positive correlation between backscatter and soil moisture for a corn canopy 92 cm high [22]. This is also seen in the results given by Vermunt *et al.* for both early and mature plants [150]. The measurements from Vermunt *et al.* also show an increase in backscatter with vegetation water content for early plants, and a saturation in the total measured backscatter around the emergence of tassels for mature plants. This characteristic is also present in the results from Sharma *et al.*, although it is not as clear in their case because cobs are present in many of their measurements for the mature growth stage [131].

Single-scattering theory-based models typically use a few scattering mechanisms like volume scattering or the soil-vegetation bounce to explain, at a first order approximation, the contributions from different vegetation or soil components. However, a corn plant has many large scattering components, and there are also adjacent plants in the near-field. In this case, the scattering mechanisms cannot be easily and correctly decomposed into individual mechanisms. The proposed technique attempts to mimic that same situation, and thus this technique does not lend itself to an analysis of quantifying different first-order scattering mechanisms.

One could still attempt to analyze the main scattering mechanisms at play in the SAR backscatter data in Fig. 4.8 and the sensitivity analysis results in Fig. 4.9. For instance, the SAR data shows an increase of at least 8 dB for all polarizations in going from DoY 169 to 199. It could reasonably be presumed that volume scattering is the dominant scattering component on DoY 199 based on the increased backscatter, the higher vegetation content, and the low soil moisture in Fig. 4.6. However, for corn at L band with non-sloped soil, the dominant component of σ^0 is the coherent interaction of the vegetation and soil as indicated by previous work by Sharma *et al.* [131] and Monsivais-Huertero *et al.* [89, 88], which can produce a similar increase in the backscatter during the growth season. Thus, the soil-vegetation bounce is likely the dominant scattering component for this study, which implies that it is still possible to have significant sensitivity to SM for the

mature plant on DoY 199.

Additionally, the plant moisture sensitivity analysis in Fig. 4.9 indicates that the backscatter may be insensitive to changes in plant moisture content for mature plant canopies. This seems unexpected considering the increased backscatter in going from DoY 169 to 199. If volume scattering were the dominant scattering component, then increasing the plant moisture content should increase the backscatter. However, the vegetation-soil bounce is the dominant component for mature growth stages, as established by the previous analysis of [131] and [89, 88]. This means that canopy attenuation will affect the backscatter, and the attenuation will increase with plant moisture. Thus, there may be a balancing effect where the increased plant moisture slightly increases volume scattering, but the vegetation-soil bounce is reduced due to the increased absorption in the canopy. The backscatter would then be relatively stable as plant moisture increased. This is perhaps the most likely explanation for the plant moisture analysis in Fig. 4.9.

Predictions from the proposed model were not compared with a radiative transfer model (RT). This was done because most recent work done on corn-field scattering has shown that SST-based models are more accurate (see [131, 49]). Additionally, RT models usually assume that the scattering medium is sparse and the size of any scatterers are small compared to the illuminating wavelength. This allows phase and extinction matrices to be defined. This is not the case for a corn field, though, because stalks are as tall as the medium and there are multiple stalks in the near-field of each other. In that case, it is not clear how the phase and extinction matrices should be specified.

4.6 Conclusion

The cultivation of corn could be enhanced by using radar to estimate quantities like soil moisture, biomass, or growth stage of the corn field. Accurate scattering models are needed to do this, though, and such models should be able to account for the plants geometry, intra- and inter-plant interactions, interactions between plants and a rough soil surface, and also reflect the row structure of the corn canopy. Numerical scattering models can meet these criteria because of their high

fidelity and precision. And even though such models are computationally very expensive, today's abundant computational power may alleviate the cost of such a model.

The commercial electromagnetic solver HFSS was used to develop a numerical scattering model for corn. The plant geometry was defined with 3D CAD models of corn plants based on data collected by the University of Florida and the Delft Technical University. Periodic boundary conditions were employed in the simulation to limit the computational domain's size. Restrictions from these boundaries were also addressed. The accuracy of the model was assessed by comparing its predictions with SAR data obtained during the SMAPVEX12 experimental campaign. Ancillary data measured during the campaign provided the inputs required by the HFSS simulation. Good agreement was observed between the model's predictions and the measured SAR data. Additionally, an experiment was conducted on the numerical model's sensitivity to soil moisture and plant moisture content changes. The observed behavior is in agreement with existing studies. These are encouraging results and indicate that this model may have predictive power in estimating corn backscatter characteristics.

Additional work is needed to reach the goal of measuring soil moisture and biomass with this scattering model. An inversion algorithm needs to be developed and would involve running the model for many different types of scenarios to build an accurate forward model or datacube. A machine learning algorithm could then be trained on the data to accurately infer soil moisture or biomass from backscatter information, which could then be used by other researchers. Future research could also be undertaken to use this model for predicting brightness temperature measurements.

CHAPTER 5

Inverse Model for Radar Sensing of Corn

5.1 Introduction

Monitoring earth's changing climate requires regular measurements of important variables. Scientists have long recognized the importance of two of them: soil moisture content (SMC) and above ground biomass (AGB) [82]. Soil moisture plays an important role in the water cycle, can affect weather patterns over land [14], and is necessary for plant growth, which is also important in agriculture. Biomass can be used as an indicator of carbon stock in the carbon cycle, and it can also be used to forecast crop yields [79]. Both SMC and AGB can be measured with instruments or sampling techniques on the ground, but such measurements are difficult to do at scale across wide areas of land. Because of this, synthetic aperture radar (SAR) has long been investigated as a potential sensor for these variables.

SAR can image wide swaths of terrain with high resolution and operate in most weather conditions during the day or night. Satellites equipped with SAR can also obtain images at regular intervals over time, and radio waves from a SAR can easily penetrate through agricultural vegetation when they operate at low microwave frequencies in L- or C-band [36]. These capabilities make it possible for SAR-equipped satellites to sense SMC and AGB over large areas at regular intervals with enough resolution to see individual agricultural fields. The challenge with doing that accurately, though, lies in the fact that radar backscatter measurements are a complex function of the soil moisture, biomass, frequency, incidence angle, the physical structure of the soil, rocks,

topography, or plants that make up the terrain, and the dielectric properties of those materials. This makes it difficult to directly relate a SAR backscatter measurement to a particular level of SMC or biomass.

Nonetheless, researchers have explored how radar might be used to measure SMC and biomass for at least three decades. The approaches that have been taken may be categorized in three ways: empirical models, semi-empirical models, and physical models. Each approach relies on measured data and expert knowledge to differing degrees. Empirical approaches typically only work well in specific situations, while semi-empirical and physical or analytical models can generalize more easily. Extensive analytical models have been developed in the past for vegetation components like leaves [68, 118, 127], branches, tree trunks [125, 72, 123, 95], grasses [138, 136, 137], and needles [119, 153]. These models have been used in more general forward models to estimate polarimetric radar backscatter from different vegetation-covered terrains [147, 73, 26, 136, 137]. These models do not require measurements to specify them since they are usually derived from first principles like Maxwell's equations. They do require several ancillary variables to specify the model, though. Because of that, there are usually fewer observable features than ancillary variables, making physical models difficult to invert.

Empirical approaches were some of the earliest to be employed. These could range from using truck-mounted scatterometers to collecting empirical data [32], to using multifrequency logarithmic models to tailor the frequency used to the level of AGB, or using tomographic SAR to suppress ground level backscatter [16]. Empirical methods also make use of machine learning (ML) techniques by training the ML algorithm on measured data. An early example of this approach was used by Pierce et al. [107]. There are a wide range of ways that empirical machine learning can be used in radar remote sensing. Regressive artificial neural networks can be trained on different polarimetric decompositions like the Freeman-Durden decomposition or others [105, 74, 77]. Different machine learning algorithms can also be used such as support vector regression or random forest regression [67, 77]. Studies of these approaches indicate that there is not yet one approach that performs effectively for every scenario: a neural network with a polarimetric decomposition

[74] may work well in one case, while using σ^0_{vv} with support vector regression is better in another [67].

Semi-empirical approaches also had an early start with the water cloud model (WCM) proposed by Attema and Ulaby for predicting σ^0 from SMC and AGB, and it has served as a building block for subsequent approaches [6, 15] or in combination with physical models [94]. The work of Oh et al. on an semi-empirical backscattering model is also an important building block for directly estimating SMC [101, 99], or in combination with the WCM [40], or with different polarimetric decompositions [53]. Change-based algorithms are another type of semi-empirical approach that relies on a time-series of measurements to make estimates of *changes* in SMC. The reasoning is that soil and plant conditions will not change quickly, while SMC will. Thus, backscatter changes on short timescales mostly come from changes in SMC. Some examples of this approach are the algorithm used by the Advanced Scatterometer (ASCAT) [152], and another that uses the co-pol ratio [104].

Finally, approaches with physical models are usually based on analytic formulas or full-wave numerical methods, with there being several notable examples for rough surfaces [44, 158, 55]. There are also notable models for vegetation based on radiative transfer [147, 18], and others based on single scattering theory and the distorted Born approximation [22, 73, 26, 89, 131]. With a physical model, it must be inverted to produce estimates of SMC or AGB. The inversion is often carried out by minimizing some type of cost function [63], but ML techniques can also be applied by training the ML algorithm from data produced by the physical model, and then later applying it to measured data. The flexibility of these algorithms also allows partial information about SMC or vegetation structure to be incorporated into the inversion, which can improve performance [9, 8, 59].

Given the extensive research on AGB and SMC retrieval with radar, we found that there were not many numerical, full-wave physical models tailored for corn fields, and modeling their backscatter is typically challenging because of their large electrical size, high density, and semi-periodic arrangement or row structure [124]. This has been partially addressed by previous work

[112], but a retrieval method was still needed. Thus, this work seeks to use the physical model in [112] for estimating SMC and biomass levels in corn fields. This is done by building a multivariate spline macromodel on top of the numerical physical model to make inversion easier. The macromodel is then inverted with a regularized cost function combined with a residual, artificial neural network (ResNet) to estimate SMC and plant height, which is used as a surrogate for AGB. In the context of previous work, this proposed method uses a physical model for the forward function, while the inverse function is based on a cost function minimization combined with ML. The primary contributions of this work are (1) using a full-wave scattering model for SMC and growth stage retrieval and (2) using an inversion technique combining classical and ML methods.

The remainder of this work is organized as follows. Section 5.2 provides a brief description of the physical model that will be inverted to make SMC and AGB estimates. Section 5.3 then explains the inversion techniques that are used. Section 5.4 gives details on the dataset of SAR, SMC, and AGB that is used to validate the overall retrieval method. Section 5.5 presents the retrieval results. Section 5.6 discusses some aspects of the results, and finally Section 5.7 summarizes the findings of this work and points toward future avenues of investigation.

5.2 Forward Model

The forward model used in this work consists of two parts. The first is a simulation methodology that uses a full-wave solver to calculate the polarimetric backscattering coefficient σ^0_{pq}, which will also be referred to as the backscatter, from fields of corn. This is referred to as the full-wave model. The second piece is a multivariate spline macromodel of the full-wave model that allows the results of the full-wave model to be readily generalized for various combinations of constitutive parameters.

5.2.1 Full-Wave Model

The full-wave model is defined by (1) the material properties of corn plants and of the soil, (2) the geometry or structure of both of those, and (3) the numerical electromagnetic analysis that is used to estimate the backscatter based on (1) and (2). The material properties, specifically the dielectric constants, of the plant and soil are defined using relationships that are already available. The dielectric constant of the plant material is specified based on the work of Ulaby and El-Rayes [145], where the gravimetric moisture content is used to estimate the dielectric constant. In this work, a gravimetric moisture content of 0.8 was used for the stalks and ears, while a content of 0.72 was used for the leaves. The soil's dielectric constant comes from the work of Mironov et al. [86], where the volumetric soil moisture content and the soil clay percentage determines the dielectric constant. This work used a constant 15% clay percentage for deriving the soil dielectric constant from the SMC.

The plant structure is defined using allometric relationships that are derived from field measurements of corn plants. The University of Florida, in conjunction with the Deflt Technical University, collected measurements on corn plant structures over the course of an entire growth cycle [62]. Some of the relevant allometric relationships can be seen in Fig. 5.1 as a function of the day after planting (DAP)–a measure of growth stage–including the stalk height and ear radius. Some relationships like the leaf length, however, depend on more than just the growth stage of the plant. This is illustrated by Fig. 5.2a, where the surface shows the leaf length versus the DAP and the normalized position of the leaf on the stalk, where 0 corresponds to the bottom, 0.5 the middle, and 1 the top of the stalk. It can be seen that the longest leaves are found for mature plants ($60 \leq \mathrm{DAP} \leq 110$) that occur near the middle of the stalk. The stalk width in Fig. 5.1b is the average of the measured diameter at the top and bottom of the stalk. The top's diameter decreased over time, which also caused the average to decrease as well. The relationships in Figs. 5.1 and 5.2a, along with the additional allometric data, allowed us to programmatically generate 3D CAD models of corn plants whose dimensions were based on the statistics of the allometric measurements. It should be noted that at least one other 3D corn model has also been developed, but it was

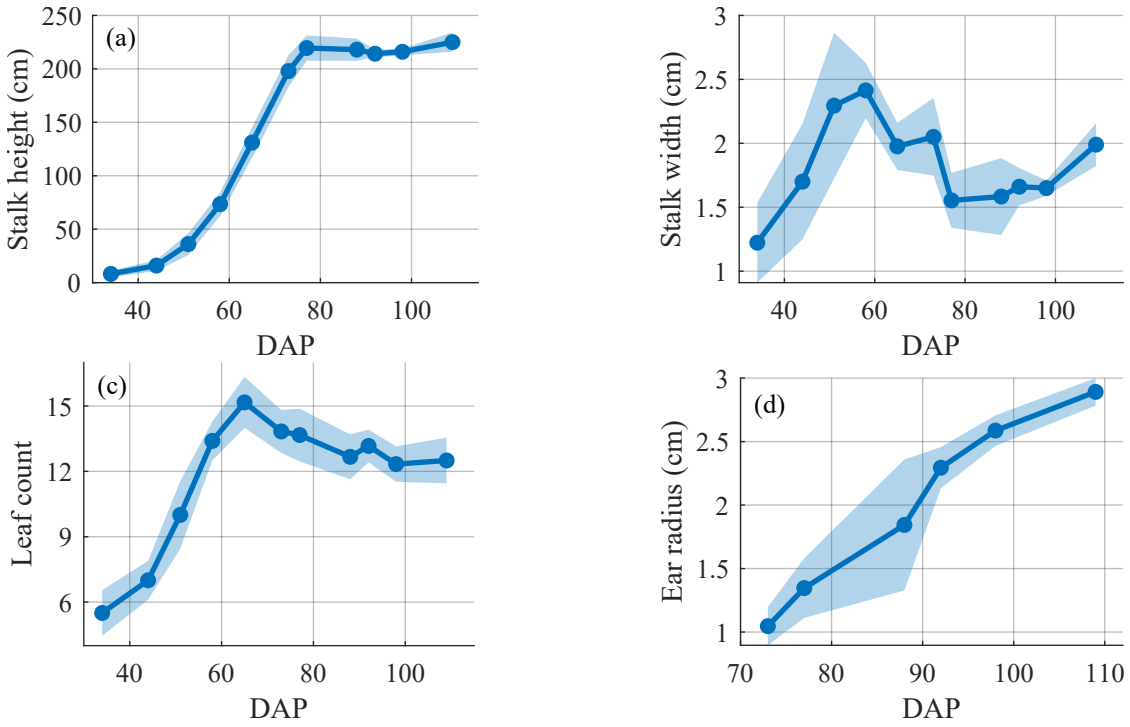
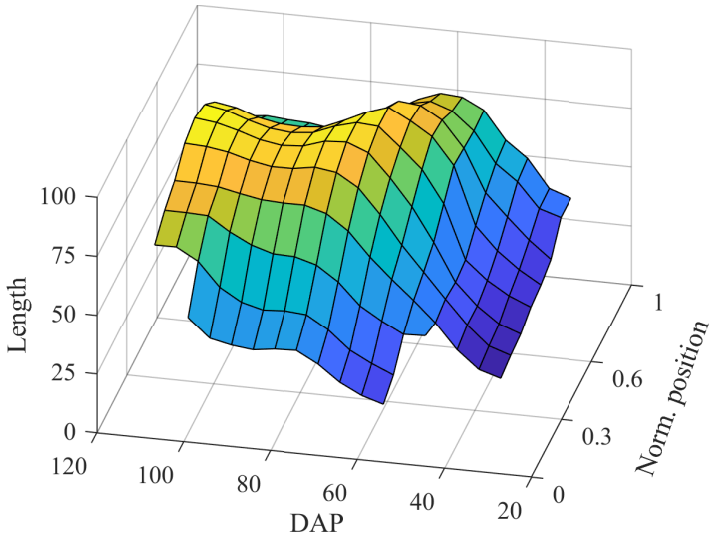


Figure 5.1: Corn allometric relationships recorded by the University of Florida versus DAP: (a) stalk height, (b) stalk width, (c) number of leaves, and (d) ear radius.

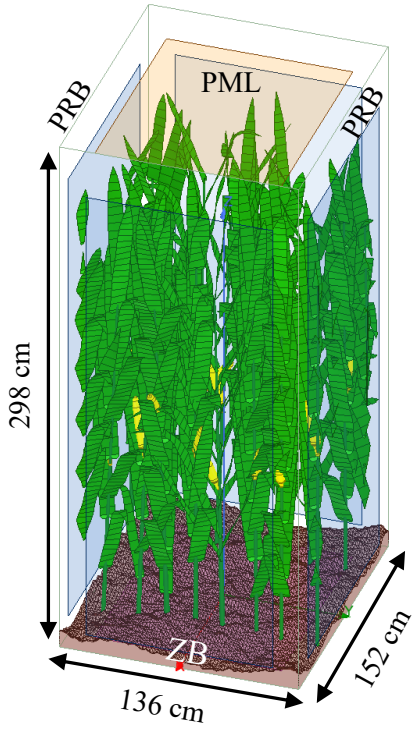
not explored in this work [163].

The soil's structure is characterized with a Gaussian profile that has an RMS height h_{rms}, correlation length l_{corr}, and correlation function. This means that the height of any point on the soil surface is expressed as a Gaussian random variable with zero mean and standard deviation h_{rms}, and the correlation between two different points is defined by the correlation length and function. An exponential correlation function with $l_{corr} = 12$ cm was used to define the soil's height profile.

Finally, the numerical electromagnetic analysis used in the full-wave model relies on the Finite Element Method (FEM) as implemented in Ansys HFSS to analyze how electromagnetic fields would interact with corn plants. There are two unique aspects of the electromagnetic analysis. The first is that the plant's leaves are represented with resistive surfaces rather than thin volumes to reduce the computational complexity. This approximation is supported by previous work done by Senior et al. [129]. The second is that the computational domain of the problem is bounded by periodic boundaries on the sides and absorbing boundaries on the top and bottom. The periodic



(a) Leaf length (cm) allometric relationship versus DAP and normalized vertical position.



(b) Nominal simulation set up with 3D CAD models of corn plants and a rough soil surface, with periodic boundaries (PRB) on the sides, a perfectly matched layer (PML) boundary on top, and an impedance boundary (ZB) on the bottom.

Figure 5.2: A surface plot showing the allometric relationships for leaf length (left) and a labeled diagram of the computational domain for calculating the backscatter from a corn field (right).

boundaries allow the response from a big corn field to be assessed, including all multiple scattering effects between adjacent plants. A 3D view of a typical plant scattering simulation is shown in Fig. 5.2b.

5.2.2 Multivariate Macromodel

The full-wave model is computationally expensive to evaluate. Thus, it is necessary to have a robust way to interpolate between different scenarios (growth stage, soil moisture level, etc.) and also provide an avenue for rapidly evaluating the forward model, which will help streamline the inversion process. Thus, a forward macromodel was made to help achieve this. One guiding

Table 5.1: Varied parameters in the simulation database.

DAP	0, 34, 44, 54, 64, 74, 84, 94, 104
m_v (m^3m^{-3})	0.05, 0.15, 0.25, 0.35
h_{rms} (cm)	1, 2, 4
Inc. Angle (ϕ_i, θ_i)	(0, 28.3), (0, 39.1), (0, 52.1), (48.2, 28.2), (43.0, 40.3), (43.8, 49.9), (90, 31.9), (90, 38.1), (90, 52.5)

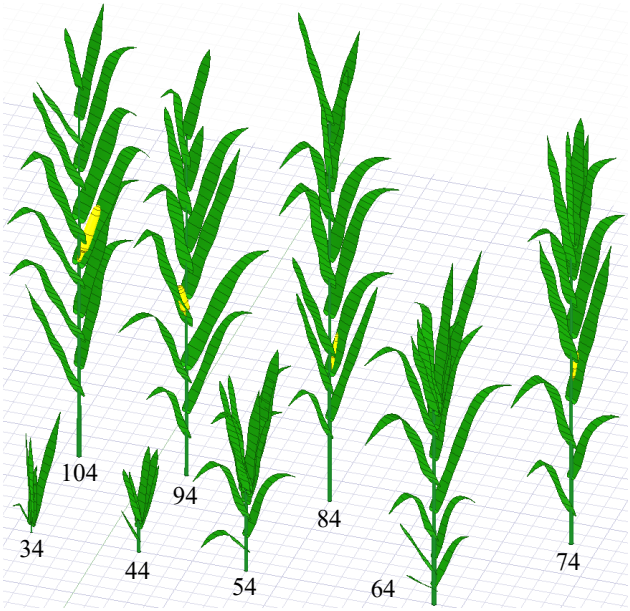


Figure 5.3: Representative plant models used for each growth stage in the macromodel with labels for the DAP of each 3D model.

principle that may justify interpolation is that the average polarimetric backscattering coefficients for vegetated, natural terrains are often smooth functions of the constitutive parameters like soil moisture or growth stage. Thus, we expect that several Monte Carlo realizations of the full-wave simulation methodology should also give average backscatter values that vary smoothly with different underlying plant or soil conditions, and this can justify interpolating the backscatter across different conditions.

Building a macromodel requires some data points on which the interpolation can be based. This initializing data requires many simulations to be run for representative scenarios. The scenarios considered by this work are shown in Table 5.1, where m_v is the volumetric moisture content of the

soil, and h_{rms} is the RMS roughness of the soil. The observation angle in elevation and azimuth (θ_i, ϕ_i) are also included, where an azimuth incident angle of $\phi_i = 0°$ corresponds to the radar looking at the corn field perpendicular to the row direction. The somewhat unusual angles are a result of using periodic boundaries, which only allow backscatter at specific angles. Scenarios with a DAP of 0 only included a rough soil surface. The allometric data was then used to programmatically generate 3D models of corn plants for different growth stages as given by the DAP. Representative models of the corn plants from each growth stage are shown in Fig. 5.3.

Each scenario in Table 5.1 was simulated at 1.25 GHz with at least 10 different random realizations. All simulations were performed on the Great Lakes high-performance computing (HPC) services at the University of Michigan. The simulations were completed over the course of two months. The simulation results make up a full-wave simulation database that contains the backscatter from every combination of the variables in Table 5.1.

This database was then used to interpolate the backscatter using penalized cubic splines with the Splinter library [48] to create a multivariate macromodel that expresses the backscatter as 4D functions of the elevation incidence angle θ_i, DAP or growth stage t, SMC m_v, and soil roughness h_{rms}, or $\sigma^0_{pq} = f_{pq}(\theta_i, t, m_v, h_{rms})$. The database does include backscatter information at three azimuth incidence angles (0°, ∼45°, 90°). However, because radar data from the validation dataset (see Section 5.4) was essentially acquired at $\phi_i = 45°$, the macromodel is only based on the results from that incidence angle. The functions' smoothness was controlled by using 2$^{\text{nd}}$ order splines for t and m_v, and 3$^{\text{rd}}$ order splines for θ_i and h_{rms}, with the spline regularization parameter $\alpha = 0.001$. Figure 5.4 shows the backscattering coefficients for σ^0_{vv} and σ^0_{hh} in decibels from the macromodel for vertical and horizontal polarizations as functions of the DAP and SMC for a given incidence angle of $\theta_i = 40°$ and an RMS roughness of 1.5 cm. Red points indicate the backscatter from the simulation database, while the colored surface shows the smoothed macromodel.

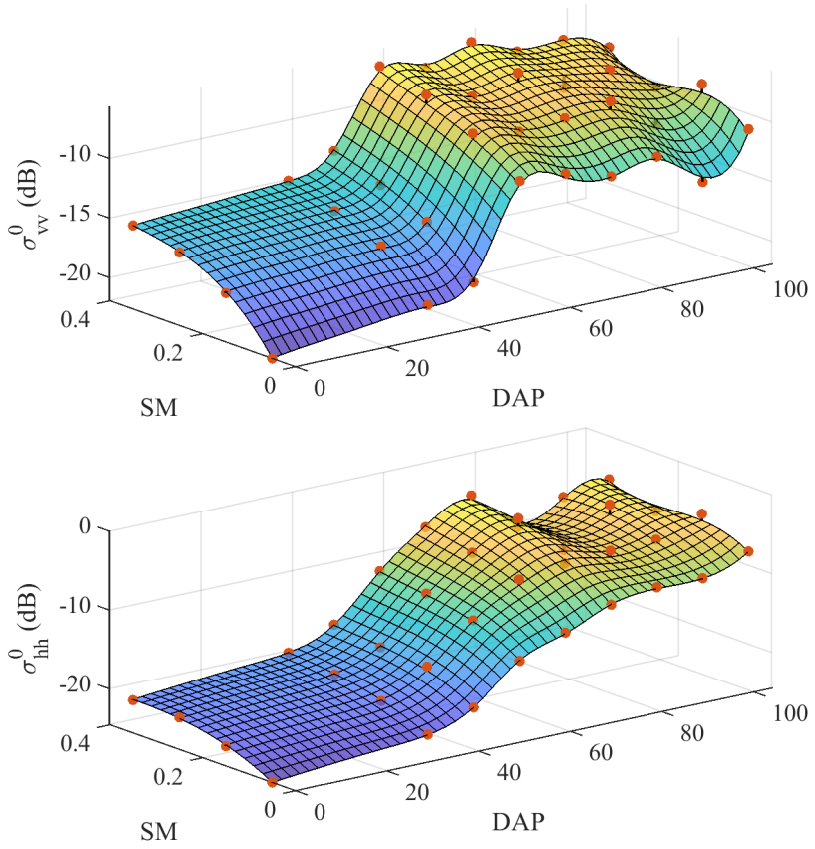


Figure 5.4: Surface plots of the spline macromodel fit to the full-wave simulation data (red dots) for σ^0_{vv} (top) and σ^0_{hh} (bottom) as a function of the DAP and SMC for a fixed $\theta_i = 40°$ and $h_{rms} = 1.5$ cm.

5.3 Inversion Algorithm

The macromodel provides a map from the constitutive parameters (SMC, growth stage, etc.) to polarimetric backscattering coefficients. A reverse map is required, though, to make estimates of SMC or growth stage from the backscatter; that is, based on the measured σ^0, we would like to find a set of macromodel parameters that at least comes close to reproducing σ^0. This is a challenging task since there are many combinations of parameters that may produce the desired σ^0. We approached it with a regressive residual artificial neural network (ResNet) combined with an iterative, nonlinear, regularized inversion (RI) method. This approach is illustrated in Fig. 5.5, where the measured backscatter σ^0_{vv}, σ^0_{hh}, σ^0_{hv}, and the incidence angle θ_i are first fed to the regularized inversion algorithm to produce coarse estimates of the growth stage $\hat{t}_c$, SMC $\hat{m}_{v,c}$, and

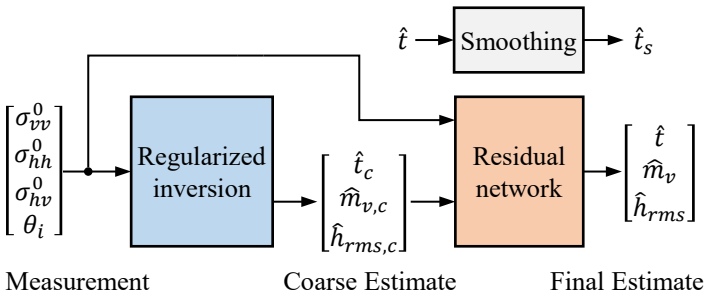


Figure 5.5: Diagram of inversion algorithm.

RMS roughness $\hat{h}_{rms,c}$. The backscatter, incidence angle, and coarse estimates are then fed to the ResNet, which makes the final SMC estimate. The ResNet's estimates for growth stage are then smoothed to give the final result for growth stage.

5.3.1 Iterative, Nonlinear, Regularized Inversion

Regularized inversion is a conventional approach for inverse problems that are ill-posed in some way. A typical formula that expresses the idea of regularization is given by

$$\min_{\mathbf{p}} g(\mathbf{p}) = \|\mathbf{F}(\mathbf{p}) - \mathbf{m}\|^2 + \frac{\mu}{2} \|L\mathbf{p}\|^2 , \tag{5.1}$$

where g is the objective function, $\mathbf{p} \in \mathbb{R}^n$ is a vector of model parameters, $\mathbf{m} \in \mathbb{R}^k$ is a vector of measurements, $\mathbf{F}$ is the model function that maps $\mathbb{R}^n$ to $\mathbb{R}^k$, μ is the regularization weight, and L is the regularization operator. A high-level interpretation of this formula is that a set of parameters $\mathbf{p}$ should be sought that minimizes the error between the measurement and the model's prediction at $\mathbf{p}$, while at the same time penalizing solutions that stray from prior knowledge of acceptable parameters. If $\mathbf{F}$ is linear, then there are many tools that allow questions of uniqueness or continuous dependence on data to be analyzed, as well as methods for minimizing g. Answering these questions becomes much more complicated if $\mathbf{F}$ is nonlinear. As indicated by Fig. 5.4, the macromodel for corn plant backscatter is nonlinear. In this case, solving (5.1) can be accomplished with an iterative optimization method [91].

We tailored (5.1) to our specific problem by considering the noisiness of the measured data and

prior knowledge of the soil roughness as follows

$$\min_{\mathbf{p}} g(\mathbf{p}) = \frac{1}{2} \left\| C_p^{-1/2} \left(\mathbf{F}(\mathbf{p}) - \tilde{\mathbf{m}} \right) \right\|^2 + \frac{\mu_r}{2} \left\| h_{rms} - h_{rms,0} \right\|^2 \tag{5.2}$$

$$\mathbf{p} = \left[\theta_i, t, m_v, h_{rms} \right]^T \tag{5.3}$$

$$\mathbf{m} = \left[\sigma_{vv}^0, \sigma_{hh}^0, \sigma_{hv}^0 \right]^T, \tag{5.4}$$

where $\tilde{\mathbf{m}}$ is a noisy measurement from a normal distribution with mean $\mathbf{m}$ and covariance matrix C_p, $h_{rms,0}$ is a prior known soil roughness, and μ_r is the regularization weight. From there, (5.2) is minimized with a global optimization routine, specifically `dual_annealing` from SciPy's optimization library [162, 140, 141, 161]. The incidence angle θ_i is used to restrict the search space since it can usually be derived from the measurement geometry. If roughness information is available, a regularization parameter value of $\mu_r = 5$ is used.

The RI serves as the first stage in the inversion algorithm. It provides rough estimates of the parameters of interest. These rough estimates are then given to the second stage: the residual network or ResNet.

5.3.2 Regressive, Residual Neural Network

Artificial neural networks have achieved significant performance breakthroughs in the past decade by effectively using the parallel computing capabilities of graphics processing units (GPUs). They have the ability to fit highly nonlinear data patterns and make predictions, and this has been applied in many diverse applications. Their capability comes at the cost of intensive training and difficulty in understanding what a trained model specifically learns. Nonetheless, the performance metrics are difficult to match. Thus, we wanted to apply the power of this machine learning technique to making SMC and ABG estimates with the simulated macromodel.

To this end, a ResNet was designed using the PyTorch framework, and its structure is illustrated in Fig. 5.6. The input features to the network are the polarimetric backscattering coefficients,

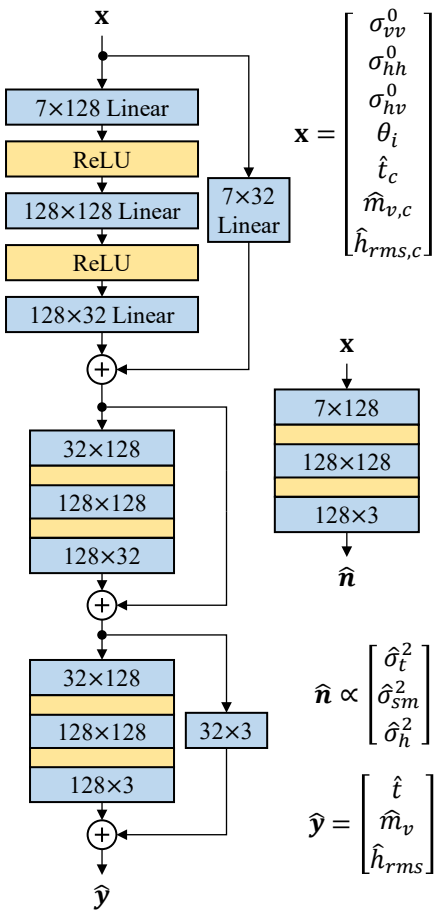


Figure 5.6: Diagram of ResNet structure for soil moisture and growth stage estimation.

incidence angle, and the coarse estimates from the regularized inversion. Information about the RMS roughness can also be included in the list of features if it is available. Other polarimetric features could also be used as inputs for the network, such as the coherent phase difference [148]. The network is made up of three residual blocks. Each block is a dense network with two hidden layers of 128 nodes each, as well as a skip connection from the input to the output. Linear blocks in the network are indicated with blue in the diagram along with the input and output dimensions (in $\times$ out). Rectified linear activations (ReLUs) are used for the activation functions between each layer, and these are shown in yellow. An additional linear layer is included in the skip connection if the dimensions of the input and output do not match. Thus, the output of a block is given by

$$\mathbf{y}_{\text{block}} = \mathbf{F}(\mathbf{x}) + \mathbf{W}_{\text{skip}}(\mathbf{x}), \tag{5.5}$$

where $\mathbf{F}$ represents the output of the dense network, and $\mathbf{W}_{\text{skip}}$ is the output of the skip connection, which is the identity operator when the input and output dimensions match. There are 7 inputs to the first block with 32 outputs. The number of outputs were increased to provide the opportunity for learned patterns from the first block to flow to subsequent ones; these additional outputs (and inputs for downstream blocks) do not have a physical basis and would represent fictitious measures determined by the network itself. The second block has input and output layers of 32 nodes. The last block has 32 input nodes and 3 output nodes, corresponding to the parameters of interest. Figure 5.6 also shows another dense, two-layer network that is trained alongside the main ResNet. It is used for predicting the variance or $\hat{\mathbf{n}}$, which is used in the loss function during training.

The loss function used for training the network relied on calculating the negative log-likelihood function, which is given by

$$L = \frac{1}{MN} \sum_{i=0}^{M-1} \sum_{j=0}^{N-1} e^{-\hat{\mathbf{n}}_j} (\hat{\mathbf{y}}_j - \mathbf{y}_j)^2 + \hat{\mathbf{n}}_j, \tag{5.6}$$

where L is the loss, $\hat{\mathbf{y}}_j$ is a set of estimated parameters, $\mathbf{y}_j$ is the corresponding set of true parameters, and $\hat{\mathbf{n}}_j$ is a set of variances that are proportional to the variance of the estimated parameters, or $\hat{\mathbf{n}} \propto [\sigma_t^2, \sigma_{sm}^2, \sigma_h^2]^T$. The summation over j in (5.6) indicates an average over all sets in the batch, and the summation over i is an average over individual parameters. Note that all parameters in (5.6) are assumed to be normalized. Using this loss function requires that the variance must also be estimated, and this is the purpose of the additional dense network in Fig. 5.6.

Two iterations of the network were trained: one that uses σ_{vv}^0, σ_{hh}^0, σ_{hv}^0, θ_i, and the coarse estimates to make predictions, and a second that has those same inputs, plus measured roughness h_{rms} information, which is also provided to the regularized inversion. The networks were trained on data created by randomly sampling the domain of the macromodel's parameters with uniform distribution. This amounted to 19 points for θ_i between 30° and 50°, 25 points for t from 0-85 days, 19 points for m_v from 0.05-0.35% or $m^3 m^{-3}$, and 13 points for h_{rms} from 1-3 cm, for a total of 117,325 training points. The parameters were normalized by their sample mean and standard

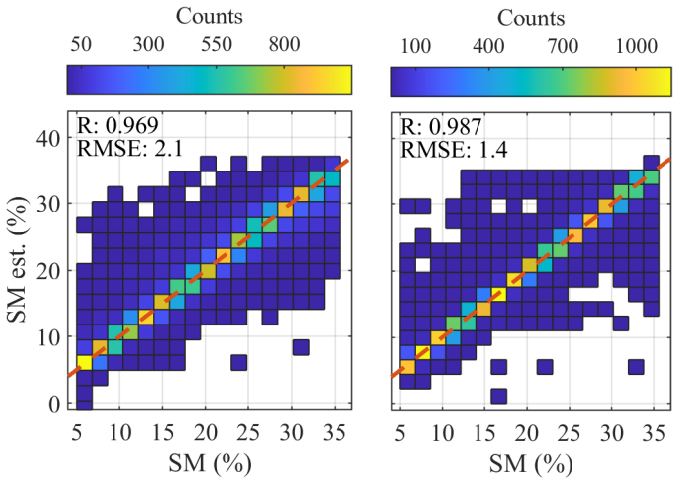


Figure 5.7: Retrieval performance for SMC from simulated data without (left) and with (right) knowledge of the roughness.

deviation so that the normalized dataset had a mean of zero and a standard deviation of one. The dataset was also randomly partitioned into training and validation datasets. The networks were then each trained for 200 epochs in batches of 512 using the Adam optimizer [64].

5.3.3 Growth Stage Smoothing

The last stage of the algorithm is to smooth the growth stage estimates. This is done to bring prior knowledge of realistic results into the algorithm, and this knowledge is the fact that, normally, the growth stage of a plant will be a monotonically increasing function of time. This is only valid in nominal growing conditions. The smoothing is carried out by again using 2^{nd} order penalized splines as implemented by the Splinter library. Here, the time variable, either DAP or DOY, is provided as the independent dataset parameter, and the estimated height $\hat{t}$ is given as the dependent dataset parameter, and a regularization parameter of 20 is used to provide the desired degree of smoothing.

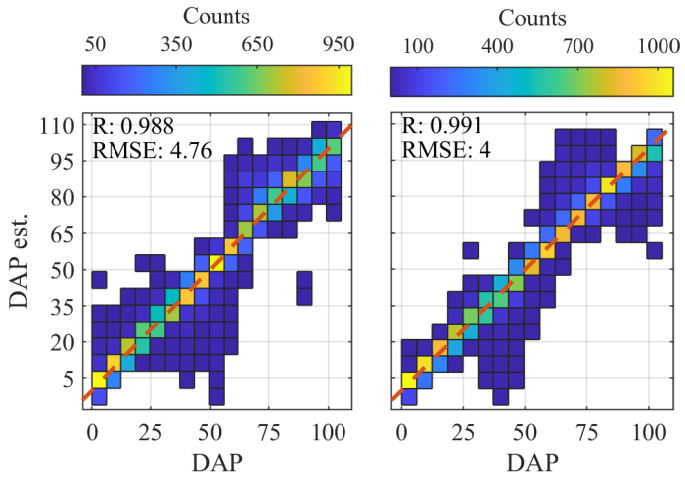


Figure 5.8: Retrieval performance for DAP from simulated data without (left) and with (right) knowledge of the roughness.

5.3.4 Simulated Algorithm Performance

After training, the performance of the inversion algorithm was evaluated with the validation dataset, which consisted of 20,000 random sets of the input parameters (θ_i, DAP, m_v, h_{rms}). These parameter sets were passed through the macromodel to give the associated backscatter. The inversion method was then given those backscatter quantities as data points with which to make predictions of SMC and growth stage (smoothing was excluded). The results of this process can be seen in Figs. 5.7 and 5.8, where bivariate histogram heatmaps are used in place of scatter plots to show the correlation between the nominal and estimated SMC and DAP values.

It can be seen that most of the SMC and DAP estimates track the nominal SMC and DAP. There are outliers, but the root mean square errors (RMSE) from the nominal estimations are 2.1% and 4.76 days, with correlation coefficients of 0.969 and 0.988 for the SMC and DAP, respectively. The second iteration that includes roughness information also performs slightly better, with perhaps a bigger boost for the SMC than DAP.

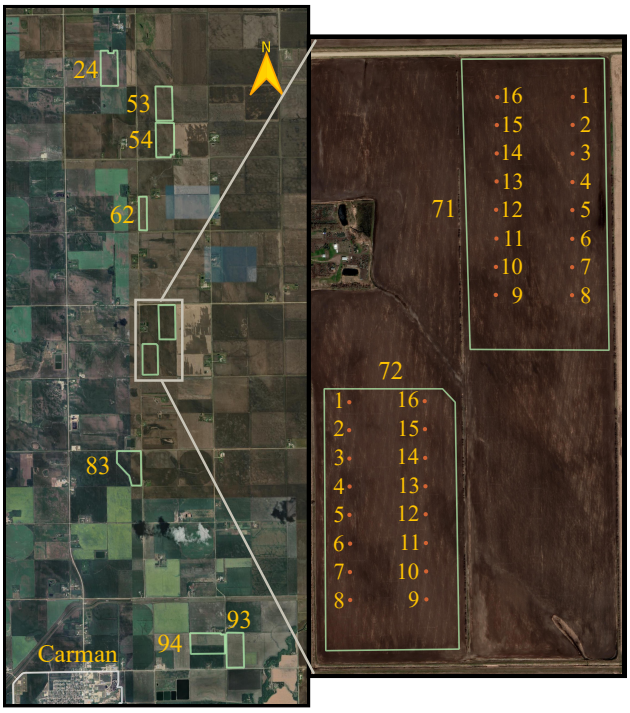


Figure 5.9: Map of corn fields considered in this study (left) and typical soil moisture sampling locations (right).

5.4 Description of Validation Data

We used data from the Soil Moisture Active Passive Validation Experiment of 2012 (SMAPVEX12) that took place in Manitoba, Canada to evaluate the performance of the inversion methods [84]. The campaign sought to collect simultaneous vegetation and radiometric measurements to aid in validating algorithms for the then upcoming SMAP mission. Brightness temperature measurements were made with the airborne PALS system, and radar backscatter measurements were made with both PALS and NASA's UAVSAR. All radiometric observations were made in L-band: 1.2 GHz for the radiometer, and 1.26 GHz for the SAR. The area of study included both forest and agricultural terrain, and the measurement of vegetation characteristics were tailored to each type of terrain. There were 9 corn fields that were monitored during the experiment campaign. Their geographic relationship can be seen in Fig. 5.9. Our study only used the measured results from fields 53, 54, 71, 83, and 94.

Table 5.2: Average soil parameters and incidence angle for each field.

Field ID	Sand	Silt	Clay	h_{rms}	l_{corr}	θ_i
53	57.8%	13.1%	29.1%	0.8 cm	7.5 cm	42.0°
54	81.25%	5.55%	13.2%	0.83 cm	5.75 cm	43.6°
71	93.5%	0.2%	6.3%	1.57 cm	15.5 cm	42.6°
83	72.75%	11.55%	15.5%	1.13 cm	8.75 cm	49.2°
94	70.80%	11.0%	18.3%	1.28 cm	8 cm	45.6°

5.4.1 Soil and Vegetation Data

The soil texture and roughness were measured for all the corn fields (and all other agricultural fields) near the beginning of the campaign. Table 5.2 shows a breakdown of this information for the fields considered. The soil moisture was typically measured in 16 locations across each field as seen on the right side of Fig. 5.9 with a portable, handheld meter to capture the spatial variation of SMC. Additionally, three measurements were taken at each location, and if furrows were present, then the three measurements were taken at the top, middle, and bottom of the furrow. The soil moisture measurements from the handheld meter were also calibrated against core soil samples whose moisture content was assessed by oven drying. Finally, the soil moisture measurements were only made on mornings when the UAVSAR flew to try and achieve simultaneous measurements.

The agricultural vegetation measurements focused on many selected fields. These fields were regularly surveyed for measurements like leaf area index and plant dimensions. The observed fields represented a diverse range of crop types from wheat to soybeans, canola, and several others. Measurement of plant characteristics like plant height were tailored to each type of crop. For corn, this meant that the plant's height and diameter were measured, as well as the total biomass and the separate biomass of the stalk and leaves. The location of these measurements took place at three of the 16 SMC measurement sites for each field that was monitored.

5.4.2 SAR Data

The UAVSAR typically made observations around 8-10 am local time. Each observation included four parallel passes that were offset so that the same location could be observed at several different observation angles. We used passes that allowed each corn field to be observed in the range of 40° -50°. These passes can be identified on the UAVSAR website as 31603, 31604, 31605, and 31606 [57]. We used pass 31603 for field 93, 31604 for fields 71 and 83, and pass 31605 for fields 53 and 54. We used the gridded, georeferenced data product from the UAVSAR website to build the backscattering coefficient covariance matrix for each pixel in every field. This allowed the backscatter to be calculated for any polarization. We primarily made use of the nominal polarimetric backscattering coefficients σ^0_{vv}, σ^0_{hh}, and σ^0_{hv}. They were then averaged over each field. The average incidence angle at each field is also given in Table 5.2.

5.5 Results

The macromodel from Section 5.2.2 provides the basis on which the inversion algorithm in Section 5.3 relies on to produce estimates of SMC and growth stage from σ^0_{pq}. This section will demonstrate the performance of the inversion algorithm against measured data from SMAPVEX12. Before doing so, however, some context for the inversion results will be added by first providing a demonstration of how well the macromodel can predict σ^0 for corn fields.

5.5.1 Forward Model Predictions

First, the SMAPVEX12 data was used to specify proper inputs for the multivariable macromodel, which consisted of the incidence angle, the growth stage, SMC, and the soil roughness. Growth stage and SMC evolved over time, and the SMAPVEX12 data on these variables is shown later in Section 5.5.2. The incidence angle did not change appreciably over time, and it was assumed that the soil roughness did not change either. Again, the values of those variables for each field are given in Table 5.2. The growth stage for the macromodel was determined by matching the

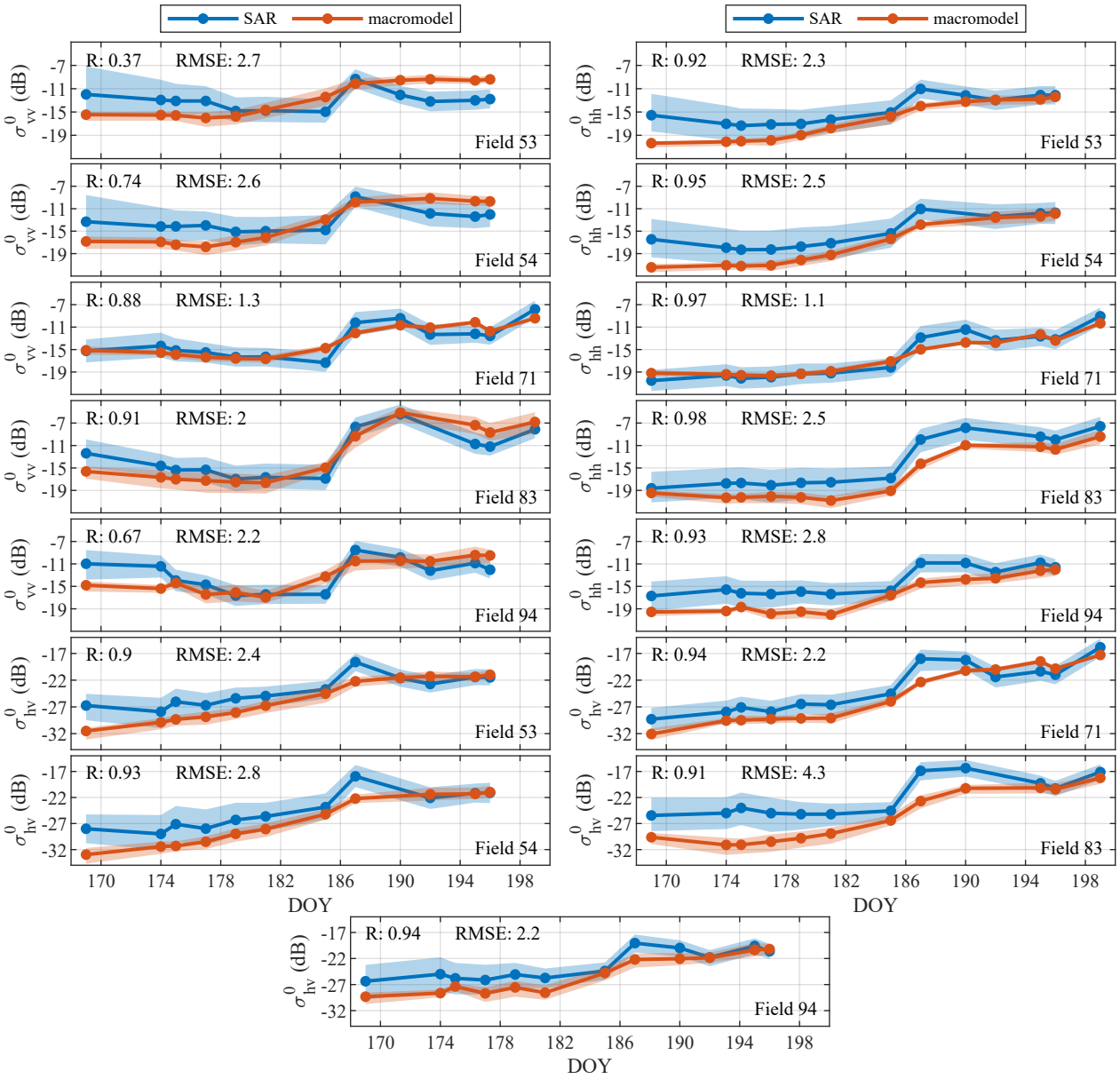


Figure 5.10: Comparison of σ^0_{pq} from UAVSAR data and the macromodel.

SMAPVEX12 average plant height with the corresponding plant height in the macromodel. For example, if the SMAPVEX12 plant height was 150 cm on day of year (DOY) 192, then that might correspond to DAP 70 in the macromodel. Finally, the nominal input for the soil moisture was determined from the average soil moisture for the entire field.

The macromodel's predictions for σ^0_{pq} are compared with the SMAPVEX12 SAR data in Fig. 5.10. The shaded area around the SAR values indicate the middle 70$^{\text{th}}$ percent, while the solid line

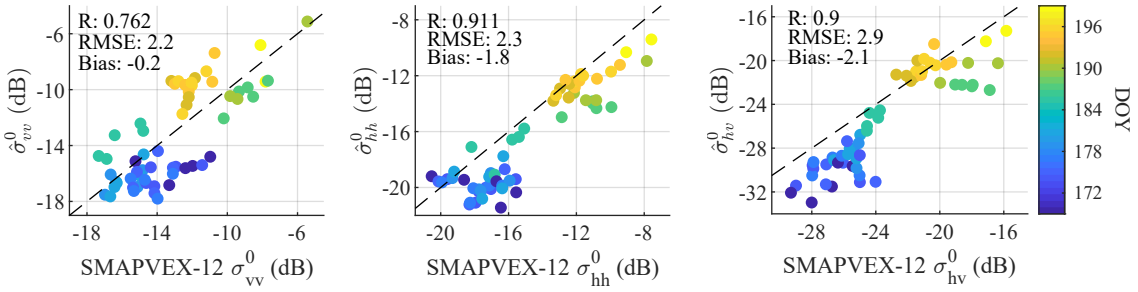


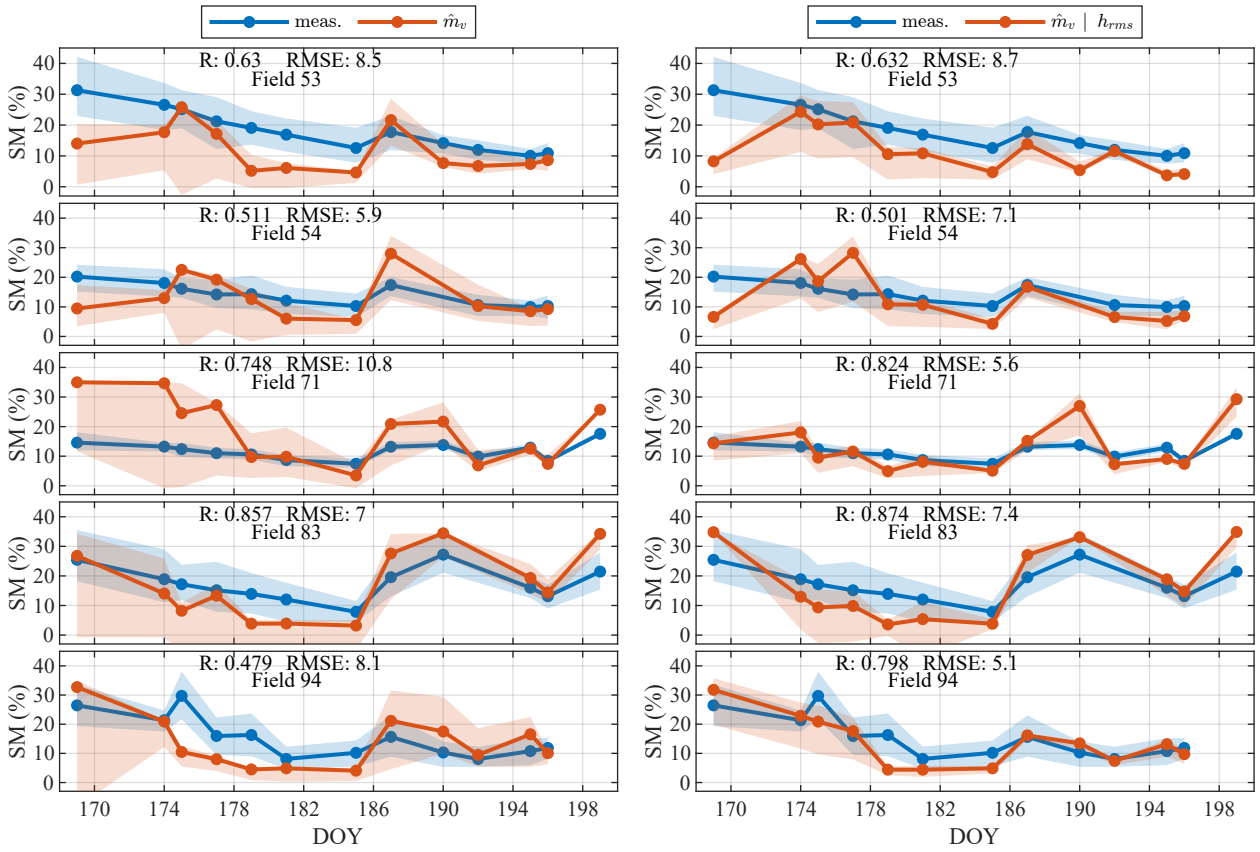
Figure 5.11: Correlations for the predicted and measured backscattering coefficients. The DOY color scale is identical among all plots.

is the median value. For the predicted (red) σ^0 values, an error tolerance was estimated based on the statistics of the SMC measurements. This was done by generating many random sets of input parameters from a normal distribution of the SMC based on the sample mean and deviation. These random sets were then fed into the macromodel to produce many σ^0 realizations that could be used to derive statistics. Again, the shaded red area indicates the middle 70^{th} percent, while the solid red line is the median. Figure 5.11 also shows the overall correlation between the measured and predicted backscatter, with points colored by DOY.

It can be seen that the macromodel's predictions generally agree well with the measured SAR data. However, both σ^0_{hh} and σ^0_{hv} are frequently underestimated, especially early in the campaign and around DOY 187 and 189. And although there is not much bias for σ^0_{vv}, the dynamics of the predicted values are subdued compared to the data. This feature is present to some degree for each polarization and field. These results are shown because the inversion's performance will be limited by how well the forward model can predict the backscatter from the constitutive parameters. Thus, it can be expected that the retrieval performance with real data will be degraded compared to the retrieval performance using simulated data.

5.5.2 Inversion Results

The inversion algorithm used the polarimetric backscattering coefficients measured by UAVSAR to estimate SMC and growth stage, where the plant height was used as a surrogate for the growth stage. One iteration of the algorithm used the measured σ^0_{vv}, σ^0_{hh}, σ^0_{hv}, and θ_i to make its estimates.



(a) Inversion algorithm estimates of SMC without soil roughness information.

(b) Inversion algorithm estimates of SMC with soil roughness information.

Figure 5.12: Inversion results for SMC.

The second iteration used those same inputs as well as h_{rms} to make its predictions. As previously mentioned, all the SAR pixels for a particular field were averaged together for each DOY, and that average value was run though the algorithm to make the estimates.

The SMC inversion results for fields 53, 54, 71, 83, and 94 are shown in Figs. 5.12a and 5.12b. Again, the shaded areas are the middle 70^{th} percent of the data, while the solid lines are the median values. The statistics are based on 48 nominal samples for each field and DOY. The statistics for the predicted values (red) were determined based on running many sets of random inputs into the inversion algorithm that are based on the statistics of the SAR data. The statistics of the SAR data, in decibels, were characterized as a multivariate, normal random variable, with a mean and covariance matrix determined by the sample mean and covariance. The statistics of the inversion

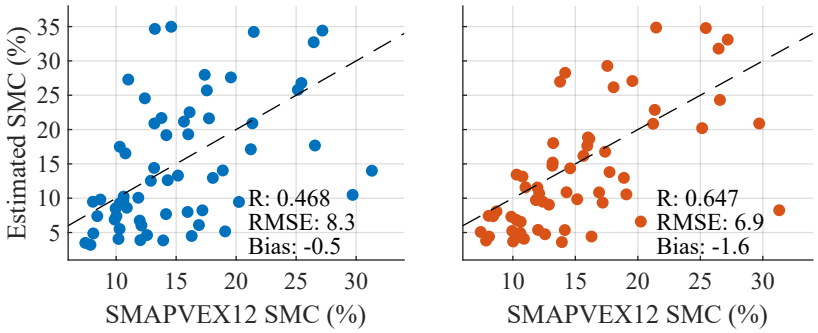


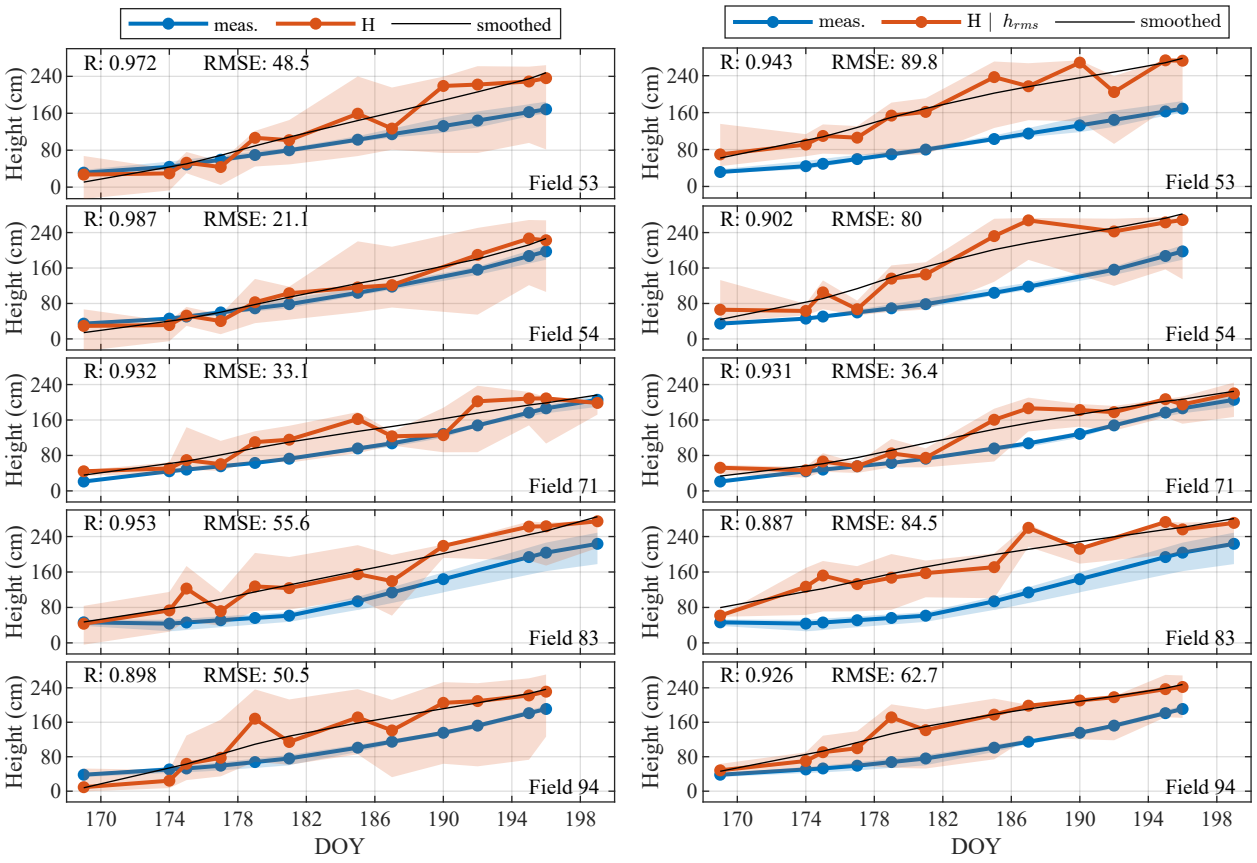
Figure 5.13: Scatter plots of measured SMC and estimated SMC values without (left) and with (right) soil roughness information.

estimates were then determined with respect to those inputs. The figures also show the correlation coefficient (R), the RMSE, and the field number.

From the results in Fig. 5.12a, it appears that the retrievals of the first iteration follows the trends of the measured data, however there are significant mismatches early in the growing season for fields 53 and 71. It is also apparent that the inversion's performance is not uniform across all the fields. For instance, the estimates for field 71 are the most inaccurate, while the estimates for field 83 agree well with the data.

The second iteration of the inversion algorithm's results can be seen in Fig. 5.12b. By taking roughness information into account, the SMC estimation accuracy improves for fields 71 and 94. There also appears to be a decrease increase in the variability of the predicted SMC overall. The performance of the algorithm's first and second iterations are summarized in the scatterplots of Fig. 5.13, where the overall correlation coefficient and RMSE improve from 0.46 and 8.3% to 0.647 and 6.9%.

The growth stage inversion results are shown in Figs. 5.14a and 5.14b. Again, the solid lines indicate the median values, while the shaded areas are the middle 70^{th} percent of the data. However, the blue solid line is the average measured plant height, while the blue-shaded area is the minimum and maximum measured height, since only 3 height measurements were made for each field. The smoothed plant height measurement is shown in black. The correlation and RMSE given in these figures are with respect to the non-smoothed estimates.



(a) Estimates of plant height using only the backscatter and incidence angle.

(b) Estimates of plant height using backscatter, incident angle, and roughness data.

Figure 5.14: Inversion results for plant height.

Both algorithm iterations generally overestimate the plant height, with the retrievals from the first performing best with field 54 and worst with field 94. The second iteration does best with field 71 and worst with 83. It appears that having roughness information reduces the variability of the retrieval, however accuracy is in general degraded. The overall retrieval performance for growth stage is summarized in Fig. 5.15, which shows the smoothed height estimates. Figure 5.15 makes it clear that the plant height is overestimated with a bias of 30.9 and 62.4 for each iteration, respectively, but otherwise there is a tight correlation of 0.951 and 0.909 between the estimated and measured values. It is also apparent that soil roughness information can degrade the plant height estimate.

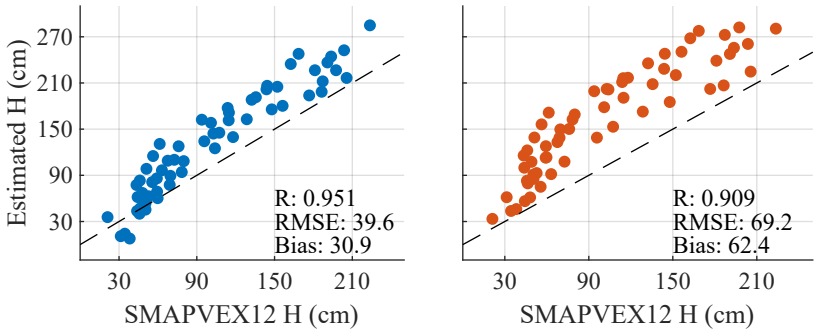


Figure 5.15: Scatterplots for smoothed plant height, with nominal results on the left, and results that include roughness information on the right.

5.6 Discussion

There are a few observations that can be made about the retrieval algorithm. First, it predicts SMC best when roughness information is provided. Second, it can predict the growth stage with better accuracy than the soil moisture, and this accuracy is enhanced when roughness information is not included in the inversion. These observations are borne out in a summary of the results shown in Tables 5.3a and 5.3b, where the height results are with respect to the smoothed estimates. There are also a few germane questions to consider in addition to these observations. One is what might be the source of errors in the predictions? A second is why is the retrieval better for some fields than others? And finally, why does roughness information generally not help with height estimation?

Considering the first question, there are several error sources. There are of course potential measurement errors with the SMC, plant height, and SAR data, and quantifying these is not possible. They may likely be small or at least typical compared to other experimental campaigns. There is also error from the inversion method, which relies on a measurement vector whose dimensionality is smaller than the parameter space it is used to estimate. The error in doing this is apparent from the simulated retrieval results in Figs. 5.7 and 5.8. Another source of error would be any mismatch between the forward scattering model and the actual scattering process that took place to produce the SAR data, which would include the soil structure, permittivity, and the plant structure and its permittivity. This source is likely in effect, and a sense of its magnitude is given by the forward model predictions in Fig. 5.10. And finally, in connection with the error from the forward

Table 5.3: Summary of inversion performance

(a) Summary of SMC results.

Patch ID	53	54	71	83	94
R	0.63	0.511	0.748	0.857	0.479
RMSE	8.5	5.9	10.8	7	8.1
Bias	-6.3	-0.8	6.6	-0.4	-2
R | h_{rms}	0.632	0.501	0.824	0.874	0.798
RMSE | h_{rms}	8.7	7.1	5.6	7.4	5.1
Bias | h_{rms}	-6.6	-1.1	1	0	-1.5

(b) Summary of smoothed plant height results.

Patch ID	53	54	71	83	94
R	0.998	0.994	0.985	0.973	0.959
RMSE	44.8	18.5	27	53.1	43.5
Bias	33	10.4	25.1	49.9	34.8
R | h_{rms}	0.989	0.968	0.982	0.94	0.961
RMSE | h_{rms}	87.2	74.2	29.9	81.7	60.5
Bias | h_{rms}	83.7	68.7	27.4	78.6	57.2

scattering process, there may be errors in the allometric model of corn plants that was used, where the generated models deviate in some way from the general structure of the corn plants that were present during SMAPVEX12.

The last two error sources may be part of the reason why the retrieval performance is not consistent across each field. For instance, the soil composition of each field is different, and the clay percentage is a key parameter for estimating the soil's dielectric constant. Again, the macromodel simulations were executed assuming a 15% clay content, so it might be expected that the retrieval performance would be best for fields 54, 83, and 94. The retrieval performance for field 83 is generally good, but comparatively not for field 54 or 94. As another example, the forward model predictions for field 71 match up better than the predictions for field 83. But the SMC retrieval performance is better for field 83 than field 71. So, while it is very likely that there is mismatch between the forward model and the real scattering scenario, it's clear that this is not the only factor that affects the variability in the retrieval performance between fields.

There is a plausible explanation for the last question. Soil roughness usually increases the soil's cross-polarized backscatter and reduces its co-polarized interaction with any plants. That first effect would strongly influence σ^0_{hv}. The second effect would influence σ^0_{vv} or σ^0_{hh}, but it may not be as strong because the fields' soil is relatively smooth for L-band; their roughness is on the edge of validity for the small perturbation model ($ks < 0.3, kl < 3, s/l < 0.3$) [109]. Additionally, vertically polarized waves will strongly couple with a corn canopy because of the

vertical orientation of the stalks, and thus σ^0_{vv} is strongly influenced by the plant height, as can be seen in the top of Fig. 5.4. Thus, because soil roughness may affect σ^0_{hv} more strongly than σ^0_{vv}, and σ^0_{vv} is strongly influenced by plant height, adding roughness information to the inversion may not strongly enhance the plant height estimates.

5.7 Conclusion

It is possible to measure soil moisture and biomass with radar because of the backscatter's sensitivity to the plant and soil structure and material properties. Deploying a SAR on a satellite makes it possible to measure these quantities at regular time intervals across the globe. Modern SAR techniques also allow large swaths of terrain to be imaged at high resolution so that SMC and biomass estimates can be used for smart agriculture applications, improving local weather forecasts, and environmental monitoring. The challenge in this endeavor is to correctly interpret backscatter with regard to SMC and biomass.

This work has sought to aid in that goal by investigating whether estimates can be improved by using σ^0_{pq} predictions from a scattering model specifically designed for corn fields that is based on a full-wave electromagnetic solver methodology. That scattering model is encapsulated in a macromodel and serves as the basis for an inversion algorithm that generates SMC and biomass estimates from radar data. The algorithm is based on a residual, artificial neural networks combined nonlinear, regularized inversion. The inversion algorithm's performance was first evaluated using simulated data from the macromodel. Then, both the macromodel and inversion algorithms were tested using vegetation, soil, and radar data that were collected during SMAPVEX12. The inversion algorithm estimated growth stage more accurately than SMC. It was also found that the SMC estimates improved if known prior information about the soil roughness was included in the inversion process. The results indicate room for improvement, since an RMSE of 4% would be more desirable. This is still an important step towards radar-based SMC and AGB estimation and represents the first time that a full-wave scattering model has been used in this application.

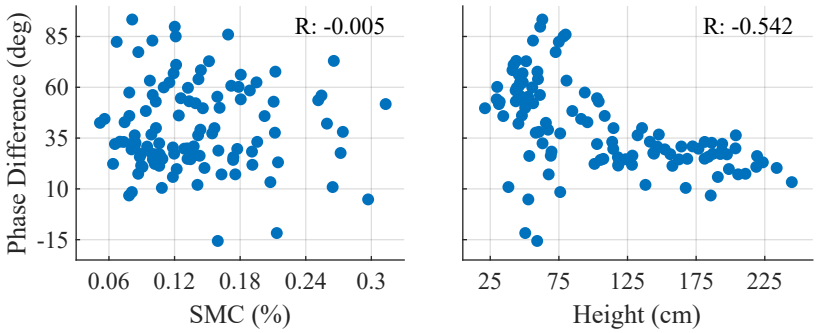


Figure 5.16: Scatterplots of the average measured co-pol phase difference versus measured SMC (left) and plant height (right).

Further improvements may come from broadband scattering models for corn fields in order to provide additional measurement points to enable more robust inversion results. Other features such as the co-pol phase difference could also be modeled and included in the inversion process. From the SMAPVEX12 data, the phase difference can provide information on plant growth stage as seen in Fig. 5.16, but not necessarily information about SMC. Modeling the phase difference would require fast full-wave simulations, since many realizations must be run in order to derive phase difference statistics (10 is not enough). The incorporation of other ancillary information would also be a large benefit, such as planting dates from farmers, a limited number of scattered in situ soil moisture sensors or estimates of canopy height from other sensing modalities like LIDAR.

CHAPTER 6

Conclusion

6.1 Research Summary and Contributions

This work has undertaken a detailed investigation of using 3D CAD models of corn plants to help push the envelope forward on using SAR data to sense biophysical parameters like SMC and Above Ground Biomass (AGB). Two important keys in this effort were (1) creating a model that could predict the radar backscatter from a set of biophysical parameters or forward model, and (2) developing an inverse model which could do the reverse: derive estimates of biophysical parameters from radar backscatter data. An important aspect of that investigation is the ability to measure the permittivity of different materials. Thus, this work also presented a novel system for the in-line measurement of a liquid's dielectric constant, which also used forward and inverse models to make estimates. A summary of the major contributions of this dissertation include:

- An in-line system for measuring a liquid's permittivity with a (1) novel sample holder design for easily introducing liquids while confining microwave energy; (2) a forward model to account for variations in the design due to manufacturing tolerances; (3) an extensive quantitative error analysis of the device; and (4) two fabricated designs to validate the measurements with previous work and real-time capability.

- A simulation methodology for corn fields that (1) faithfully represents the plant's geometry, (2) accurately accounts for interactions among plant constituents and other adjacent plants,

(3) accounts for interactions between the plants and the soil surface, (4) reflects the row structure of the canopy, and (5) is computationally feasible for a full-wave commercial solver to execute.

- A computer program for creating realistic 3D models of corn plants based on measured data from the University of Florida, and a database of simulated radar backscatter from corn for a whole growing season, which may be interpolated with splines to create a forward macromodel. The forward model is also compared with SAR data from SMAPVEX12 and is shown to have good agreement.

- A novel inverse model based on classical iterative, regularized inversion and a neural network, which uses the macromodel for making estimates and training data for the network. It's ability to estimate plant height and soil moisture is again evaluated against SMAPVEX12 data.

6.2 Insights

The main contributions of this work stepped through the process of modeling radar scattering and then using that model to sense biophysical parameters from radar data. Several insights were gained in going through that process.

The first is that accurately retrieving parameters from radar data is difficult. Part of that difficulty comes from several sources of uncertainty. One of these is modeling uncertainty, where the scattering model may not faithfully represent the scattering processes that occur in reality. Another source is associated with experimental data. Examples of this are the uncertainties associated with the calibration of Synthetic Aperture Radar (SAR) data, and at what depth in situ soil moisture measurements are made. Finally, there is some error that arises when attempting to invert a multi-parameter scattering model. These uncertainties and error sources can build up, making it difficult to retrieve biophysical parameters with high accuracy. The difficulty of properly characterizing ground-truth data (SAR, in situ SMC measurements) has been identified by Long and Ulaby in

[76, p. 364], who referred to it as a "curse of remote sensing."

The second set of insights comes from some modeling aspects that could make an important difference but were difficult to characterize. The first of these was the structure of the soil. This work assumes a surface profile based on a random Gaussian process. However, the presence of furrow-like structures would affect scattering from the soil surface. The effect of such structures was not considered, though, because there was not enough information that could be found about the shape of such structures. Thus, in the future they could be better characterized by using pin profilometers or 3D scans of the soil profile to measure any furrow structures in a field. The second modeling aspect is the spacing between plants. Spacing makes a difference as illustrated in Section 3.5.1. However, once again there was a lack of information about the variability of plant spacing. Given another attempt at this study, it would be helpful to measure both the row and inter-plant spacing statistics by measuring many samples in different corn fields.

The third insight deals with the experimental dataset. SMAPVEX12 is an excellent dataset, and it would have been more useful for the purposes of this work if there was more information about the previously mentioned modeling aspects (soil profile, plant spacing). There are also a couple aspects of the radar data that would be more conducive for validating a vegetation scattering model. The UAVSAR is an excellent, complicated system that makes use of electronic beam steering to correct for the attitude of the UAVSAR with respect to the area of interest that it is attempting to image. The beam's characteristics likely change with respect to the steering angle, and this could introduce some variability in the observed backscatter. Additionally, the resolution of the multi-look UAVSAR dataset used in this work is about 5×7.2 m (range $\times$ azimuth) per pixel. The raw single-look data has a higher resolution of about 1.67×0.6 m. This higher resolution would help in resolving spatial variations within fields, but the UAVSAR single-look data was more difficult to access during the course of this work.

For these reasons, it may be possible to more thoroughly validate a scattering model for corn fields by using a relatively simpler, small SAR system operating from a drone that could operate with a fixed antenna beam, high resolution, while incorporating a consistent calibration routine.

The fixed beam would reduce variation from beam steering, and a higher pixel resolution would help with discerning spatial variations. A consistent calibration routine is a necessary feature to track changes in scattering from a corn field. Using such a SAR system in combination with other ground-truth measurements like the plant structure or soil moisture could then provide an experimental database with a tighter relationship between the radiometric and biophysical measurements, which may then help to enhance the fidelity of any developed scattering model.

6.3 Future Work

6.3.1 Standardized Test Datasets

It is still an open question as to how well this corn field forward model performs in comparison to other types of well-known models like ones based on RT or the DBA. It would be valuable to see one of these methods applied in the same way as the present work to the SMAPVEX12 data to provide a thorough, fair comparison. A lack of such comparisons between different methods is one challenge that may face the field right now. Perhaps one reason for this may be the scarcity of easily accessible high-quality datasets with simultaneous measurements. There are many studies that publish good work on their own methods, but sometimes with datasets that are unique to their work in some way, thus making it difficult to fairly compare two different methods. The availability of Sentinel-I data has certainly helped to provide some commonality between approaches, however. It may be a valuable asset for the microwave remote sensing community to have a standard group of datasets that new SMC or AGB retrieval algorithms or forward scattering can be tested against. This would help to clarify what methods work well and crystallize meaningful progress.

6.3.2 Modeling Tilted Ground Planes

On the forward modeling side, one direction for future investigation is studying the effect of a tilted ground plane on the backscatter from corn plants. It certainly has a significant effect, and

it may be possible to fully characterize it with the methodology of this work. However, it could require significant computation, since taking ground tilt and tilt direction into account will add two variables to the five which already make up the simulation database, thus requiring *many* additional simulations.

6.3.3 Additional Directions for Future Investigation

- Applying this same simulation methodology to other types of plants. An important focus here would be developing accurate allometric models of the plants.
- Extending the plant full-wave analysis to calculate the backscatter as a function of frequency. The current setup does not easily allow this (essentially, simulations have to be re-run for each frequency).
- Accelerating the process of calculating the average backscatter coefficient. The current method relies on averaging the results of several random realizations in order to arrive at that. Perhaps the solution to this may be a custom numerical solver that can execute much more quickly.
- On the inverse sensing side, additional features could be investigated for improving predictions, such as the average co-pol phase difference or multi-frequency data.

APPENDIX A

SST-based Corn Scattering Model

The SST-based model follows the same formulation as that given by Sharma *et al.* [131] in their appendix, with several modifications. First, scattering coefficients are calculated for the entire plant as one entity, rather than breaking it up into stalks and leaves. Second, the plant's scattering coefficients are calculated using HFSS, which has the benefit of accounting for intra-plant scattering mechanisms. The equations for the direct and bistatic components were modified to reflect the fact that the simulation's phase center was located at the bottom of the stalk of each plant. The average direct component is given by

$$\bar{\sigma}^0_{q,direct} = \frac{\langle \sigma_{q,direct} \rangle}{A_{plant}} e^{-4|\kappa''_q|d}, \tag{A.1}$$

where the angle brackets $\langle \cdot \rangle$ are an average of the orientation statistics and plant models, $\sigma_{q,direct}$ is the direct RCS calculated by HFSS, q is the vertical (v) or horizontal (h) polarization, A_{plant} is the nominal area of ground that each plant occupies, κ''_q is the imaginary part of the mean wave propagation constant, and d is the canopy depth. The bistatic component is given by

$$\bar{\sigma}^0_{q,bistatic} = 4|\Gamma_{q,surface}|^2 \frac{\langle \sigma_{q,bistatic} \rangle}{A_{plant}} e^{-4|\kappa''_q|d}, \tag{A.2}$$

where $\Gamma_{q,surface}$ is the reflection coefficient of a rough soil surface, and $\sigma_{q,bistatic}$ is the bistatic RCS calculated by HFSS. Finally, the rough surface scattering $\sigma^0_{q,surface}$ is calculated with AIEM [43, 158] rather than IEM [42].

BIBLIOGRAPHY

[1] Yadgar I. Abdulkarim, Lianwen Deng, Olcay Altıntaş, Emin Ünal, and Muharrem Karaaslan. Metamaterial absorber sensor design by incorporating swastika shaped resonator to determination of the liquid chemicals depending on electrical characteristics. *Physica E: Low-dimensional Systems and Nanostructures*, 114:113593, 2019.

[2] Yadgar I. Abdulkarim, Lianwen Deng, Muharrem Karaaslan, and Emin Unal. Determination of the liquid chemicals depending on the electrical characteristics by using metamaterial absorber based sensor. *Chemical Physics Letters*, 732:136655, 2019.

[3] Zurina Zainal Abidin, Fatin Nordalila Omar, Pavithiran Yogarajah, Dayang Radiah Awang Biak, and Yaakob Bin Che Man. Dielectric characterization of liquid containing low alcoholic content for potential halal authentication in the 0.5-50 ghz range. *American Journal of Applied Sciences*, 11(7):1104, 2014.

[4] Fatemeh Akbar, Behzad Yektakhah, Haokui Xu, and Kamal Sarabandi. A low-complexity time-domain method for a fast and accurate measurement of q-factor and resonant frequency of rf and microwave resonators. *IEEE Access*, 9:96478–96486, 2021.

[5] Andrea Alu and Nader Engheta. Dielectric sensing in ε-near-zero narrow waveguide channels. *Physical Review B*, 78(4):045102, 2008.

[6] EPW Attema and Fawwaz T Ulaby. Vegetation modeled as a water cloud. *Radio science*, 13(2):357–364, 1978.

[7] R. Augustine, S. Raman, and A. Rydberg. Relative permittivity measurements of et–oh and mt–oh mixtures for calibration standards in 1–15 ghz range. *Electronics Letters*, 50(5):358–359, 2014.

[8] Nicolas Baghdadi, R Cresson, Mohammad El Hajj, R Ludwig, and Isabelle La Jeunesse. Estimation of soil parameters over bare agriculture areas from c-band polarimetric sar data using neural networks. *Hydrology and Earth System Sciences*, 16(6):1607–1621, 2012.

[9] Nicolas Baghdadi, S Gaultier, and C King. Retrieving surface roughness and soil moisture from synthetic aperture radar (sar) data using neural networks. *Canadian Journal of Remote Sensing*, 28(5):701–711, 2002.

[10] Mehmet Bakır, Şekip Dalgaç, Muharrem Karaaslan, Faruk Karadağ, Oğuzhan Akgol, Emin Unal, Tolga Depçi, and Cumali Sabah. A comprehensive study on fuel adulteration sensing

by using triple ring resonator type metamaterial. *Journal of The Electrochemical Society*, 166(12):B1044, aug 2019.

[11] Jian-Zhong Bao, Mays L Swicord, and Christopher C Davis. Microwave dielectric characterization of binary mixtures of water, methanol, and ethanol. *The Journal of chemical physics*, 104(12):4441–4450, 1996.

[12] Matías Ernesto Barber, David Sebastián Rava, and Carlos López-Martínez. L-band sar copolarized phase difference modeling for corn fields. *Remote Sensing*, 13(22):4593, 2021.

[13] P Beckman and AM Spizzichino. Electromagnetic scattering from rough surfaces, 1963.

[14] David O Benson and Paul A Dirmeyer. Characterizing the relationship between temperature and soil moisture extremes and their role in the exacerbation of heat waves over the contiguous united states. *Journal of Climate*, 34(6):2175–2187, 2021.

[15] Rajat Bindlish and Ana P Barros. Parameterization of vegetation backscatter in radar-based, soil moisture estimation. *Remote sensing of environment*, 76(1):130–137, 2001.

[16] Erik Blomberg, Laurent Ferro-Famil, Maciej J Soja, Lars MH Ulander, and Stefano Tebaldini. Forest biomass retrieval from l-band sar using tomographic ground backscatter removal. *IEEE Geoscience and Remote Sensing Letters*, 15(7):1030–1034, 2018.

[17] Jean Bouchat, Emma Tronquo, Anne Orban, Niko EC Verhoest, and Pierre Defourny. Assessing the potential of fully polarimetric mono-and bistatic sar acquisitions in l-band for crop and soil monitoring. *IEEE Journal of Selected Topics in Applied Earth Observations and Remote Sensing*, 15:3168–3178, 2022.

[18] M Bracaglia, P Ferrazzoli, and L Guerriero. A fully polarimetric multiple scattering model for crops. *Remote Sensing of Environment*, 54(3):170–179, 1995.

[19] Mariko Burgin, Daniel Clewley, Richard M Lucas, and Mahta Moghaddam. A generalized radar backscattering model based on wave theory for multilayer multispecies vegetation. *IEEE Transactions on geoscience and remote sensing*, 49(12):4832–4845, 2011.

[20] Matteo Camporese, Silvio J Gumiere, Mario Putti, and Gianluca Botter. Efficient irrigation of maize through soil moisture monitoring and modeling. *Frontiers in Water*, 3:627551, 2021.

[21] Yunhao Cao, Cunjun Ruan, Kanglong Chen, and Xingyun Zhang. Research on a high-sensitivity asymmetric metamaterial structure and its application as microwave sensor. *Scientific Reports*, 12(1), 2022. Cited by: 6; All Open Access, Gold Open Access, Green Open Access.

[22] Narinder S Chauhan, David M Le Vine, and Roger H Lang. Discrete scatter model for microwave radar and radiometer response to corn: comparison of theory and data. *IEEE Transactions on Geoscience and Remote Sensing*, 32(2):416–426, 1994.

[23] Kun-Shan Chen, Tzong-Dar Wu, Leung Tsang, Qin Li, Jiancheng Shi, and Adrian K Fung. Emission of rough surfaces calculated by the integral equation method with comparison to three-dimensional moment method simulations. *IEEE Transactions on Geoscience and Remote Sensing*, 41(1):90–101, 2003.

[24] Tao Chen, Suyan Li, and Hui Sun. Metamaterials application in sensing. *Sensors*, 12(3):2742–2765, 2012.

[25] Clara Chew and Eric Small. Description of the ucar/cu soil moisture product. *Remote Sensing*, 12(10):1558, 2020.

[26] Tsenchieh Chiu and Kamal Sarabandi. Electromagnetic scattering from short branching vegetation. *IEEE Transactions on Geoscience and Remote Sensing*, 38(2):911–925, 2000.

[27] Christopher Aragón. Svg version of the usda soil texture triangle chart. https://commons.wikimedia.org/wiki/File:USDA_Soil_Texture.svg, 2018. [Online; accessed 14-January-2025].

[28] Euclides Lourenço Chuma, Yuzo Iano, Glauco Fontgalland, and Leonardo Lorenzo Bravo Roger. Microwave sensor for liquid dielectric characterization based on metamaterial complementary split ring resonator. *IEEE Sensors Journal*, 18(24):9978–9983, 2018.

[29] JO Curtis, CA Weiss Jr, and JB Everett. Effect of soil composition on dielectric properties. *US Army Corps Eng. Waterways Exp. Station, Vicksburg, MS, Tech. Rep. EL-95-34*, 1995.

[30] C Ditzler, K Scheffe, HC Monger, et al. Soil science division staff. *Soil survey manual*, pages 120, 603, 2017.

[31] Pascale C Dubois, T Engman, et al. Corrections to" measuring soil moisture with imaging radars". *IEEE Transactions on Geoscience and Remote Sensing*, 33(6):1340, 1995.

[32] Pascale C Dubois, Jakob Van Zyl, and Ted Engman. Measuring soil moisture with imaging radars. *IEEE transactions on geoscience and remote sensing*, 33(4):915–926, 1995.

[33] Google Earth, Maxar Technologies 2023, CNES, Airbus 2023, Landsat, and Copernicus. Satellite imagery of Manitoba, Canada. Google Earth, August 25, 2022. Accessed June 11, 2025.

[34] B. Edwards, A. Alù, M. G. Silveirinha, and N. Engheta. Reflectionless sharp bends and corners in waveguides using epsilon-near-zero effects. *Journal of Applied Physics*, 105(4):044905, 2009.

[35] Brian Edwards, Andrea Alù, Michael E. Young, Mário Silveirinha, and Nader Engheta. Experimental verification of epsilon-near-zero metamaterial coupling and energy squeezing using a microwave waveguide. *Phys. Rev. Lett.*, 100:033903, Jan 2008.

[36] M El Hajj, N Baghdadi, H Bazzi, and M Zribi. Penetration analysis of sar signals in the c and l bands for wheat, maize, and grasslands, remote sens., 11, 22–24, 2019.

[37] Mohamed A El-Rayes and Fawwaz T Ulaby. Microwave dielectric spectrum of vegetation-part i: Experimental observations. *IEEE Transactions on Geoscience and Remote Sensing*, (5):541–549, 1987.

[38] Dara Entekhabi, Eni G Njoku, Peggy E O'Neill, Kent H Kellogg, Wade T Crow, Wendy N Edelstein, Jared K Entin, Shawn D Goodman, Thomas J Jackson, Joel Johnson, et al. The soil moisture active passive (smap) mission. *Proceedings of the IEEE*, 98(5):704–716, 2010.

[39] H.-J. Eul and B. Schiek. A generalized theory and new calibration procedures for network analyzer self-calibration. *IEEE Transactions on Microwave Theory and Techniques*, 39(4):724–731, 1991.

[40] Fabio Fascetti, Nazzareno Pierdicca, and Luca Pulvirenti. Empirical fitting of forward backscattering models for multitemporal retrieval of soil moisture from radar data at l-band. *Journal of Applied Remote Sensing*, 11(1):016002–016002, 2017.

[41] Rémy Fieuzal, C Marais Sicre, and Frédéric Baup. Estimation of corn yield using multi-temporal optical and radar satellite data and artificial neural networks. *International journal of applied earth observation and geoinformation*, 57:14–23, 2017.

[42] Adrian K Fung and Kun-Shan Chen. *Microwave scattering and emission models for users*. Artech house, 2010.

[43] Adrian K Fung, Zongqian Li, and Kun-Shan Chen. Backscattering from a randomly rough dielectric surface. *IEEE Transactions on Geoscience and remote sensing*, 30(2):356–369, 1992.

[44] A.K. Fung, W.Y. Liu, K.S. Chen, and M.K. Tsay. An improved iem model for bistatic scattering from rough surfaces. *Journal of Electromagnetic Waves and Applications*, 16(5):689–702, 2002.

[45] Ruoxing Gao, Jongwoo Jeong, Weihui Gu, Leung Tsang, Andreas Colliander, and Simon Yueh. Full-wave simulations of scattering by corn fields at l-band. In *IGARSS 2022-2022 IEEE International Geoscience and Remote Sensing Symposium*, pages 847–850. IEEE, 2022.

[46] Gianluca Gennarelli, Stefania Romeo, Maria Rosaria Scarfì, and Francesco Soldovieri. A microwave resonant sensor for concentration measurements of liquid solutions. *IEEE Sensors Journal*, 13(5):1857–1864, 2013.

[47] A. Gregory and R. Clarke. A review of rf and microwave techniques for dielectric measurements on polar liquids. *IEEE Transactions on Dielectrics and Electrical Insulation*, 13:727–743, 2006.

[48] Bjarne Grimstad. Splinter, 2018.

[49] Weihui Gu, Leung Tsang, Andreas Colliander, and Simon H Yueh. Wave propagation in vegetation field using a hybrid method. *IEEE Transactions on Antennas and Propagation*, 69(10):6752–6761, 2021.

[50] Jacques Hadamard. Sur les problèmes aux dérivées partielles et leur signification physique. *Princeton university bulletin*, pages 49–52, 1902.

[51] Martti T Hallikainen, Fawwaz T Ulaby, Myron C Dobson, Mohamed A El-Rayes, and Lil-Kun Wu. Microwave dielectric behavior of wet soil-part 1: Empirical models and experimental observations. *IEEE Transactions on geoscience and remote sensing*, (1):25–34, 1985.

[52] Roger F. Harrington. *Time-Harmonic Electromagnetic Fields*. IEEE-Press, 2001.

[53] Lian He, Rocco Panciera, Mihai A Tanase, Jeffrey P Walker, and Qiming Qin. Soil moisture retrieval in agricultural fields using adaptive model-based polarimetric decomposition of sar data. *IEEE Transactions on Geoscience and Remote Sensing*, 54(8):4445–4460, 2016.

[54] Mehdi Hosseini, Heather McNairn, Amine Merzouki, and Anna Pacheco. Estimation of leaf area index (lai) in corn and soybeans using multi-polarization c-and l-band radar data. *Remote Sensing of Environment*, 170:77–89, 2015.

[55] Shaowu Huang and Leung Tsang. Electromagnetic scattering of randomly rough soil surfaces based on numerical solutions of maxwell equations in three-dimensional simulations using a hybrid uv/pbtg/smcg method. *IEEE Transactions on Geoscience and Remote Sensing*, 50(10):4025–4035, 2012.

[56] Shaowu Huang, Leung Tsang, Eni G Njoku, and Kuan Shan Chan. Backscattering coefficients, coherent reflectivities, and emissivities of randomly rough soil surfaces at l-band for smap applications based on numerical solutions of maxwell equations in three-dimensional simulations. *IEEE Transactions on Geoscience and Remote Sensing*, 48(6):2557–2568, 2010.

[57] Jet Propulsion Laboratory. Uavsar data search.

[58] Abhishek Kumar Jha and M. Jaleel Akhtar. Design of multilayered epsilon-near-zero microwave planar sensor for testing of dispersive materials. *IEEE Transactions on Microwave Theory and Techniques*, 63(8):2418–2426, 2015.

[59] Mingquan Jia, Ling Tong, Yan Chen, Yong Wang, and Yuanzhi Zhang. Rice biomass retrieval from multitemporal ground-based scatterometer data and radarsat-2 images using neural networks. *Journal of Applied Remote Sensing*, 7(1):073509–073509, 2013.

[60] Xianfeng Jiao, Heather McNairn, Jiali Shang, Elizabeth Pattey, Jiangui Liu, and Catherine Champagne. The sensitivity of radarsat-2 polarimetric sar data to corn and soybean leaf area index. *Canadian Journal of Remote Sensing*, 37(1):69–81, 2011.

[61] Alicia T Joseph, Rogier van der Velde, Peggy E O'Neill, Roger H Lang, and Tim Gish. Soil moisture retrieval during a corn growth cycle using l-band (1.6 ghz) radar observations. *IEEE Transactions on Geoscience and Remote Sensing*, 46(8):2365–2374, 2008.

[62] Jasmeet Judge, Pang-Wei Liu, Alejandro Monsiváis-Huertero, Tara Bongiovanni, Subit Chakrabarti, Susan C Steele-Dunne, Daniel Preston, Samantha Allen, Jaime Polo Bermejo, Patrick Rush, et al. Impact of vegetation water content information on soil moisture retrievals in agricultural regions: An analysis based on the smapvex16-microwex dataset. *Remote Sensing of Environment*, 265:112623, 2021.

[63] Seung-Bum Kim, Mahta Moghaddam, Leung Tsang, Mariko Burgin, Xiaolan Xu, and Eni G Njoku. Models of l-band radar backscattering coefficients over global terrain for soil moisture retrieval. *IEEE Transactions on Geoscience and Remote Sensing*, 52(2):1381–1396, 2013.

[64] Diederik P Kingma. Adam: A method for stochastic optimization. *arXiv preprint arXiv:1412.6980*, 2014.

[65] Il-Suek Koh, Feinian Wang, and Kamal Sarabandi. Estimation of coherent field attenuation through dense foliage including multiple scattering. *IEEE transactions on geoscience and remote sensing*, 41(5):1132–1135, 2003.

[66] Angela Kross, Heather McNairn, David Lapen, Mark Sunohara, and Catherine Champagne. Assessment of rapideye vegetation indices for estimation of leaf area index and biomass in corn and soybean crops. *International Journal of Applied Earth Observation and Geoinformation*, 34:235–248, 2015.

[67] P Kumar, R Prasad, A Choudhary, DK Gupta, VN Mishra, AK Vishwakarma, AK Singh, and PK Srivastava. Comprehensive evaluation of soil moisture retrieval models under different crop cover types using c-band synthetic aperture radar data. *Geocarto International*, 34(9):1022–1041, 2019.

[68] R Kumar and L Silva. Light ray tracing through a leaf cross section. *Applied Optics*, 12(12):2950–2954, 1973.

[69] Jeffrey C. Lagarias, James A. Reeds, Margaret H. Wright, and Paul E. Wright. Convergence properties of the nelder–mead simplex method in low dimensions. *SIAM Journal on Optimization*, 9(1):112–147, 1998.

[70] Roger H Lang. Electromagnetic backscattering from a sparse distribution of lossy dielectric scatterers. *Radio Science*, 16(01):15–30, 1981.

[71] Rae Duk Lee, Han Jun Kim, and Yu.P. Semenov. Precise measurement of the dielectric constants of liquids using the principle of cross capacitance. *IEEE Transactions on Instrumentation and Measurement*, 50(2):298–301, 2001.

[72] Yi-Cheng Lin and Kamal Sarabandi. Electromagnetic scattering model for a tree trunk above a tilted ground plane. *IEEE Transactions on Geoscience and Remote Sensing*, 33(4):1063–1070, 1995.

[73] Yi-Cheng Lin and Kamal Sarabandi. A monte carlo coherent scattering model for forest canopies using fractal-generated trees. *IEEE Transactions on Geoscience and Remote Sensing*, 37(1):440–451, 1999.

[74] Jian Liu, Youshuan Xu, Henghui Li, and Jiao Guo. Soil moisture retrieval in farmland areas with sentinel multi-source data based on regression convolutional neural networks. *Sensors*, 21(3):877, 2021.

[75] Humberto Lobato-Morales, DVB Murthy, Alonso Corona-Chávez, José Luis Olvera-Cervantes, Juan Martínez-Brito, and Luis Gerardo Guerrero-Ojeda. Permittivity measurements at microwave frequencies using epsilon-near-zero (enz) tunnel structure. *IEEE transactions on microwave theory and techniques*, 59(7):1863–1868, 2011.

[76] David Long and Fawwaz Ulaby. *Microwave radar and radiometric remote sensing*. Artech, 2015.

[77] Changchang Lv, Qinghua Xie, Xing Peng, Qi Dou, Jinfei Wang, Juan M Lopez-Sanchez, Jiali Shang, Lei Chen, Haiqiang Fu, Jianjun Zhu, et al. Soil moisture retrieval over agricultural fields with machine learning: A comparison of quad-, compact-, and dual-polarimetric time-series sar data. *Journal of Hydrology*, 644:132093, 2024.

[78] Jianwei Ma, Shifeng Huang, Jiren Li, Xiaotao Li, Xiaoning Song, Pei Leng, and Yayong Sun. Estimating vegetation water content of corn and soybean using different polarization ratios based on l-and s-band radar data. *IEEE Geoscience and Remote Sensing Letters*, 14(3):364–368, 2017.

[79] Yuchi Ma, Zhou Zhang, Yanghui Kang, and Mutlu Özdoğan. Corn yield prediction and uncertainty analysis based on remotely sensed variables using a bayesian neural network approach. *Remote Sensing of Environment*, 259:112408, 2021.

[80] Daniel W Mackowski. Exact solution for the scattering and absorption properties of sphere clusters on a plane surface. *Journal of Quantitative Spectroscopy and Radiative Transfer*, 109(5):770–788, 2008.

[81] Nathan Marcuvitz. *Waveguide Handbook*. Institution of Electrical Engineers, GBR, 1986.

[82] PJ Mason, JW Zillman, A Simmons, EJ Lindstrom, DE Harrison, H Dolman, S Bojinski, A Fischer, J Latham, J Rasmussen, et al. Implementation plan for the global observing system for climate in support of the unfccc (2010 update). 2010.

[83] Kyle C McDonald, Myron C Dobson, and Fawwaz T Ulaby. Using mimics to model l-band multiangle and multitemporal backscatter from a walnut orchard. 1990.

[84] Heather McNairn, Thomas J Jackson, Grant Wiseman, Stephane Belair, Aaron Berg, Paul Bullock, Andreas Colliander, Michael H Cosh, Seung-Bum Kim, Ramata Magagi, et al. The soil moisture active passive validation experiment 2012 (smapvex12): Prelaunch calibration and validation of the smap soil moisture algorithms. *IEEE Transactions on Geoscience and Remote Sensing*, 53(5):2784–2801, 2014.

[85] Thomas Meissner and Frank J Wentz. The complex dielectric constant of pure and sea water from microwave satellite observations. *IEEE Transactions on Geoscience and remote Sensing*, 42(9):1836–1849, 2004.

[86] Valery L Mironov, Lyudmila G Kosolapova, and Sergej V Fomin. Physically and mineralogically based spectroscopic dielectric model for moist soils. *IEEE Transactions on Geoscience and Remote Sensing*, 47(7):2059–2070, 2009.

[87] Iliana E Mladenova, Thomas J Jackson, Rajat Bindlish, and Scott Hensley. Incidence angle normalization of radar backscatter data. *IEEE Transactions on Geoscience and Remote Sensing*, 51(3):1791–1804, 2012.

[88] Alejandro Monsivais-Huertero and Jasmeet Judge. Comparison of backscattering models at l-band for growing corn. *IEEE Geoscience and Remote Sensing Letters*, 8(1):24–28, 2010.

[89] Alejandro Monsivais-Huertero, Pang-Wei Liu, and Jasmeet Judge. Phenology-based backscattering model for corn at l-band. *IEEE Transactions on Geoscience and Remote Sensing*, 56(9):4989–5005, 2018.

[90] Said Mosbah, Chemseddine Zebiri, Djamel Sayad, Issa Elfergani, Mohamed Lamine Bouknia, Samira Mekki, Rami Zegadi, Merih Palandoken, Jonathan Rodriguez, and Raed A. Abd-Alhameed. Compact and highly sensitive bended microwave liquid sensor based on a metamaterial complementary split-ring resonator. *Applied Sciences*, 12(4):2144, Feb 2022.

[91] Jennifer L Mueller and Samuli Siltanen. *Linear and nonlinear inverse problems with practical applications*. SIAM, 2012.

[92] Aditya Varma Muppala, A. Kaleo Roberts, Adib Nashashibi, and Kamal Sarabandi. Real-time dielectric sensing of liquids using waveguide supercoupling. In *2021 IEEE International Symposium on Antennas and Propagation and USNC-URSI Radio Science Meeting (APS/URSI)*, pages 607–608, 2021.

[93] MM Nabi, Volkan Senyurek, Ali C Gurbuz, and Mehmet Kurum. Deep learning-based soil moisture retrieval in conus using cygnss delay–doppler maps. *IEEE Journal of Selected Topics in Applied Earth Observations and Remote Sensing*, 15:6867–6881, 2022.

[94] Parag S Narvekar, Dara Entekhabi, Seung-Bum Kim, and Eni G Njoku. Soil moisture retrieval using l-band radar observations. *IEEE Transactions on Geoscience and Remote Sensing*, 53(6):3492–3506, 2015.

[95] Hamid Nejati and Kamal Sarabandi. Theoretical analysis of tree trunk rough surface interaction using reaction theorem. In *2012 IEEE International Geoscience and Remote Sensing Symposium*, pages 5169–5172. IEEE, 2012.

[96] R.L. Nielson. Stand establishment variability in corn, 1997.

[97] Ebbe Nyfors. Industrial microwave sensors—a review. *Subsurface Sensing Technologies and Applications*, 1:23–43, 01 2000.

[98] United States Department of Agriculture. 2017 census of agriculture.

[99] Yisok Oh. Quantitative retrieval of soil moisture content and surface roughness from multipolarized radar observations of bare soil surfaces. *IEEE Transactions on Geoscience and Remote Sensing*, 42(3):596–601, 2004.

[100] Yisok Oh, Young-Mi Jang, and Kamal Sarabandi. Full-wave analysis of microwave scattering from short vegetation: An investigation on the effect of multiple scattering. *IEEE transactions on geoscience and remote sensing*, 40(11):2522–2526, 2002.

[101] Yisok Oh, Kamal Sarabandi, and Fawwaz T Ulaby. Semi-empirical model of the ensemble-averaged differential mueller matrix for microwave backscattering from bare soil surfaces. *IEEE Transactions on Geoscience and Remote Sensing*, 40(6):1348–1355, 2002.

[102] Roberto Olmi, Viacheslav V. Meriakri, Amleto Ignesti, Saverio Priori, and Cristiano Riminesi. Monitoring alcoholic fermentation by microwave dielectric spectroscopy. *Journal of Microwave Power and Electromagnetic Energy*, 41(3):38–50, 2006.

[103] Jeffrey D Ouellette, Mohammad M Al-Khaldi, and Joel T Johnson. Soil moisture retrieval using cygnss data in a time-series ratio method: Progress update and error analysis, part ii. *IEEE Journal of Selected Topics in Applied Earth Observations and Remote Sensing*, 2024.

[104] Jeffrey D Ouellette, Joel T Johnson, Anna Balenzano, Francesco Mattia, Giuseppe Satalino, Seung-Bum Kim, R Scott Dunbar, Andreas Colliander, Michael H Cosh, Todd G Caldwell, et al. A time-series approach to estimating soil moisture from vegetated surfaces using l-band radar backscatter. *IEEE transactions on geoscience and remote sensing*, 55(6):3186–3193, 2017.

[105] Mehmet Siraç Özerdem, Emrullah Acar, and Remzi Ekinci. Soil moisture estimation over vegetated agricultural areas: Tigris basin, turkey from radarsat-2 data by polarimetric decomposition models and a generalized regression neural network. *Remote Sensing*, 9(4):395, 2017.

[106] Jeil Park, Praveen Gurrala, Brian K Hornbuckle, and Jiming Song. Modeling the microwave transmissivity of row crops. *The Applied Computational Electromagnetics Society Journal (ACES)*, pages 816–823, 2021.

[107] LE Pierce, MC Dobson, EP Wilcox, and FT Ulaby. Artificial neural network inversion of tree canopy parameters in the presence of diversity. In *Proceedings of IGARSS'93-IEEE International Geoscience and Remote Sensing Symposium*, pages 394–397. IEEE, 1993.

[108] Divya Prakash and Nisha Gupta. High-sensitivity grooved csrr-based sensor for liquid chemical characterization. *IEEE Sensors Journal*, 22(19):18463–18470, 2022.

[109] Stephen O Rice. Reflection of electromagnetic waves from slightly rough surfaces. *Communications on pure and applied mathematics*, 4(2-3):351–378, 1951.

[110] Hannah Ritchie, Pablo Rosado, and Max Roser. Environmental impacts of food production. *Our World in Data*, 2022. https://ourworldindata.org/environmental-impacts-of-food.

[111] Hannah Ritchie and Max Roser. Land use. *Our World in Data*, 2019. https://ourworldindata.org/land-use.

[112] A Kaleo Roberts, Jiayi Wu, Alejandro Monsivais-Huertero, Jasmeet Judge, Robert C Moore, and Kamal Sarabandi. Microwave backscatter phenomenology of corn fields at l-band using a full-wave electromagnetic solver. *IEEE Transactions on Geoscience and Remote Sensing*, 2023.

[113] Thomas Maximillian Roberts, Ian Colwell, Clara Chew, Stephen Lowe, and Rashmi Shah. A deep-learning approach to soil moisture estimation with gnss-r. *Remote Sensing*, 14(14):3299, 2022.

[114] Emanuele Santi, Davide Comite, Laura Dente, Leila Guerriero, Nazzareno Pierdicca, Maria Paola Clarizia, and Nicolas Floury. Global soil moisture mapping at 5 km by combining gnss reflectometry and machine learning in view of hydrognss. *Science of Remote Sensing*, 10:100177, 2024.

[115] K. Sarabandi. A technique for dielectric measurement of cylindrical objects in a rectangular waveguide. *IEEE Transactions on Instrumentation and Measurement*, 43(6):793–798, 1994.

[116] K Sarabandi. Foundations of applied electromagnetics. *Ann Arbor, MI, University of Michigan Press*, 2022.

[117] K. Sarabandi and E.S. Li. Microstrip ring resonator for soil moisture measurements. *IEEE Transactions on Geoscience and Remote Sensing*, 35(5):1223–1231, 1997.

[118] K Sarabandi, Thomas BA Senior, and FT Ulaby. Effect of curvature on the backscattering from a leaf. *Journal of Electromagnetic Waves and Applications*, 2(7):653–670, 1988.

[119] Kamal Sarabandi. A technique for dielectric measurement of cylindrical objects in a rectangular waveguide. *IEEE transactions on instrumentation and measurement*, 43(6):793–798, 2002.

[120] Kamal Sarabandi and Tsenchieh Chiu. Electromagnetic scattering from slightly rough surfaces with inhomogeneous dielectric profiles. *IEEE Transactions on Antennas and Propagation*, 45(9):1419–1430, 1997.

[121] Kamal Sarabandi and Eric S Li. Microstrip ring resonator for soil moisture measurements. *IEEE transactions on geoscience and remote sensing*, 35(5):1223–1231, 1997.

[122] Kamal Sarabandi, Paul F Polatin, and Fawwaz T Ulaby. Monte carlo simulation of scattering from a layer of vertical cylinders. *IEEE transactions on antennas and propagation*, 41(4):465–475, 1993.

[123] Kamal Sarabandi, Paul F Polatin, and Fawwaz T Ulaby. Monte carlo simulation of scattering from a layer of vertical cylinders. *IEEE transactions on antennas and propagation*, 41(4):465–475, 2002.

[124] Kamal Sarabandi, Ahad Tavakoli, and Fawwaz T Ulaby. Propagation in a two-dimensional periodic random medium with inhomogeneous particle distribution. *IEEE transactions on antennas and propagation*, 40(10):1175–1186, 1992.

[125] Kamal Sarabandi and Fawwaz T Ulaby. High frequency scattering from corrugated stratified cylinders. *IEEE transactions on antennas and propagation*, 39(4):512–520, 1991.

[126] Kamal Sarabandi and Fawwaz Tayssir Ulaby. Technique for measuring the dielectric constant of thin materials. *IEEE Transactions on Instrumentation and Measurement*, 37(4):631–636, 1988.

[127] Kamal Sarabandi, Fawwaz Tayssir Ulaby, and TBA Senior. Millimeter wave scattering model for a leaf. *Radio science*, 25(1):9–18, 1990.

[128] Vikram Sekar, William J. Torke, Samuel Palermo, and Kamran Entesari. A self-sustained microwave system for dielectric-constant measurement of lossy organic liquids. *IEEE Transactions on Microwave Theory and Techniques*, 60(5):1444–1455, 2012.

[129] TBA Senior, K Sarabandi, and FT Ulaby. Measuring and modeling the backscattering cross section of a leaf. *Radio Science*, 22(06):1109–1116, 1987.

[130] Volkan Senyurek, Fangni Lei, Dylan Boyd, Ali Cafer Gurbuz, Mehmet Kurum, and Robert Moorhead. Evaluations of machine learning-based cygnss soil moisture estimates against smap observations. *Remote Sensing*, 12(21):3503, 2020.

[131] Avinash Sharma, Roger H Lang, Mehmet Kurum, Peggy E O'neill, and Michael H Cosh. L-band radar experiment and modeling of a corn canopy over a full growing season. *IEEE Transactions on Geoscience and Remote Sensing*, 58(8):5821–5835, 2020.

[132] Omar Siddiqui, Mani Kashanianfard, and Omar Ramahi. Dielectric sensors based on electromagnetic energy tunneling. *Sensors*, 15(4):7844–7856, 2015.

[133] Mário Silveirinha and Nader Engheta. Tunneling of electromagnetic energy through subwavelength channels and bends using ε-near-zero materials. *Physical review letters*, 97(15):157403, 2006.

[134] Hewlett-Packard Staff. Automating the hp 8410b microwave network analyzer. *Hewlett-Packard Application Note A*, 221:1979.

[135] James M Stiles and Kamal Sarabandi. Electromagnetic scattering from grassland. i. a fully phase-coherent scattering model. *IEEE Transactions on Geoscience and Remote Sensing*, 38(1):339–348, 2000.

[136] James M Stiles and Kamal Sarabandi. Electromagnetic scattering from grassland. i. a fully phase-coherent scattering model. *IEEE Transactions on Geoscience and Remote Sensing*, 38(1):339–348, 2000.

[137] James M Stiles, Kamal Sarabandi, and Fawwaz T Ulaby. Electromagnetic scattering from grassland. ii. measurement and modeling results. *IEEE Transactions on Geoscience and Remote Sensing*, 38(1):349–356, 2000.

[138] James M Stiles, Kamal Sarabandi, and Fawwaz T Ulaby. Microwave scattering model for grass blade structures. *IEEE transactions on geoscience and remote sensing*, 31(5):1051–1059, 2002.

[139] Alex Stogryn. Electromagnetic scattering from rough, finitely conducting surfaces. *Radio Science*, 2(4):415–428, 1967.

[140] Constantino Tsallis. Possible generalization of boltzmann-gibbs statistics. *Journal of statistical physics*, 52:479–487, 1988.

[141] Constantino Tsallis and Daniel A Stariolo. Generalized simulated annealing. *Physica A: Statistical Mechanics and its Applications*, 233(1-2):395–406, 1996.

[142] L Tsang, MC Kubacsi, and JA Kong. Radiative transfer theory for active remote sensing of a layer of small ellipsoidal scatterers. *Radio Science*, 16(03):321–329, 1981.

[143] Leung Tsang and JA Kong. Radiative transfer theory for active remote sensing of half-space random media. *Radio Science*, 13(5):763–773, 1978.

[144] Fawwaz Ulaby and T Bush. Corn growth as monitored by radar. *IEEE Transactions on Antennas and Propagation*, 24(6):819–828, 1976.

[145] Fawwaz T Ulaby and MOHAMED A El-Rayes. Microwave dielectric spectrum of vegetation-part ii: Dual-dispersion model. *IEEE Transactions on Geoscience and Remote Sensing*, (5):550–557, 1987.

[146] Fawwaz T Ulaby, Daniel Held, Myron C Donson, Kyle C McDonald, and Thomas BA Senior. Relating polaization phase difference of sar signals to scene properties. *IEEE Transactions on Geoscience and Remote Sensing*, (1):83–92, 1987.

[147] Fawwaz T Ulaby, Kamal Sarabandi, Kyle Mcdonald, Michael Whitt, and M Craig Dobson. Michigan microwave canopy scattering model. *International Journal of Remote Sensing*, 11(7):1223–1253, 1990.

[148] FT Ulaby, K Sarabandi, and A Nashashibi. Statistical properties of the mueller matrix of distributed targets. In *IEE Proceedings F (Radar and Signal Processing)*, volume 139, pages 136–146. IET, 1992.

[149] Leonard S Unganai and Felix N Kogan. Drought monitoring and corn yield estimation in southern africa from avhrr data. *Remote sensing of environment*, 63(3):219–232, 1998.

[150] Paul C Vermunt, Saeed Khabbazan, Susan C Steele-Dunne, Jasmeet Judge, Alejandro Monsivais-Huertero, Leila Guerriero, and Pang-Wei Liu. Response of subdaily l-band backscatter to internal and surface canopy water dynamics. *IEEE Transactions on Geoscience and Remote Sensing*, 59(9):7322–7337, 2020.

[151] Gorden Videen, Mary G Turner, Vincent J Iafelice, William S Bickel, and William L Wolfe. Scattering from a small sphere near a surface. *JOSA A*, 10(1):118–126, 1993.

[152] Wolfgang Wagner, Sebastian Hahn, Richard Kidd, Thomas Melzer, Zoltan Bartalis, Stefan Hasenauer, Julia Figa, Patricia De Rosnay, Alexander Jann, Stefan Schneider, et al. The ascat soil moisture product: A review of its. *Meteorologische Zeitschrift*, 22(1):1–29, 2013.

[153] Feinian Wang and Kamal Sarabandi. An enhanced millimeter-wave foliage propagation model. *IEEE Transactions on Antennas and Propagation*, 53(7):2138–2145, 2005.

[154] Y.-Z. Wei and S. Sridhar. Radiation-corrected open-ended coax line technique for dielectric measurements of liquids up to 20 ghz. *IEEE Transactions on Microwave Theory and Techniques*, 39(3):526–531, 1991.

[155] Wikipedia contributors. Maize — Wikipedia, the free encyclopedia. https://en.wikipedia.org/w/index.php?title=Maize&oldid=1251720389, 2024. [Online; accessed 21-October-2024].

[156] Jo-Yu Wu and Robert Lee. The advantages of triangular and tetrahedral edge elements for electromagnetic modeling with the finite-element method. *IEEE Transactions on Antennas and Propagation*, 45(9):1431–1437, 1997.

[157] Tzong-Dar Wu, Kun-Shan Chen, Jiancheng Shi, and Adrian K Fung. A transition model for the reflection coefficient in surface scattering. *IEEE Transactions on Geoscience and Remote Sensing*, 39(9):2040–2050, 2001.

[158] Tzong-Dar Wu, Kun-Shan Chen, Jiancheng Shi, Hung-Wei Lee, and Adrian K Fung. A study of an aiem model for bistatic scattering from randomly rough surfaces. *IEEE Transactions on Geoscience and Remote Sensing*, 46(9):2584–2598, 2008.

[159] Xuerui Wu, Wenxiao Ma, Junming Xia, Weihua Bai, Shuanggen Jin, and Andrés Calabia. Spaceborne gnss-r soil moisture retrieval: Status, development opportunities, and challenges. *Remote Sensing*, 13(1):45, 2020.

[160] Peter Xaypraseuth, R Satish, and Alok Chatterjee. Nisar spacecraft concept overview: Design challenges for a proposed flagship dual-frequency sar mission. In *2015 IEEE Aerospace Conference*, pages 1–11. IEEE, 2015.

[161] Yang Xiang and XG Gong. Efficiency of generalized simulated annealing. *Physical Review E*, 62(3):4473, 2000.

[162] Yang Xiang, DY Sun, W Fan, and XG Gong. Generalized simulated annealing algorithm and its application to the thomson model. *Physics Letters A*, 233(3):216–220, 1997.

[163] Boxiang Xiao, Xinyu Guo, Xiaohong Du, Weiliang Wen, Xue Wang, and Shenglian Lu. An interactive digital design system for corn modeling. *Mathematical and computer modelling*, 51(11-12):1383–1389, 2010.

[164] Simon H Yueh, Rashmi Shah, M Julian Chaubell, Akiko Hayashi, Xiaolan Xu, and Andreas Colliander. A semiempirical modeling of soil moisture, vegetation, and surface roughness impact on cygnss reflectometry data. *IEEE Transactions on Geoscience and Remote Sensing*, 60:1–17, 2020.

[165] John XJ Zhang and Kazunori Hoshino. *Molecular sensors and nanodevices: principles, designs and applications in biomedical engineering*. Academic Press, 2018.